Development and Application of Planar Laser Thermometry in Sooting Flames

Doctoral Dissertation

Dahe Gu

July 2016

School of Mechanical Engineering
Faculty of Engineering, Mathematical and Computer Sciences
The University of Adelaide, Australia

Declarations

This work contains no material that has been accepted for the award of any other degree or diploma in any university or other tertiary institution and, to the best of my knowledge and belief, contains no material previously published or written by another person, except where due reference has been made in the text.

I give consent to this copy of my thesis when deposited in the University Library, being made available for loan and photocopying, subject to the provisions of the Copyright Act 1968.

The author acknowledges that copyright of published works arising from this thesis resides with the copyright holder(s) of those works.

I also give permission for the digital version of my thesis to be made available on the web, via the University's digital research repository, the Library catalogue, the Australasian Digital Theses Program (ADTP) and also through web search engines, unless permission has been granted by the University to restrict access for a period of time.

Dahe Gu

Acknowledgments

This work would not have been possible without the invaluable contributions and support from numerous people. First and foremost, I must acknowledge the reliable supervision and outstanding assistance provided by my academic supervisors, Prof. Graham 'Gus' Nathan, A/Prof. Zeyad Alwahabi, Dr Paul Medwell and Prof. Bassam Dally, whose tutelage has guided me through the highs and lows of a research student. In addition, I owe my deepest gratitude to Dr Zhiwei Sun, who has made available his support in countless ways.

I am also indebted to many of the staff members from both the Mechanical and Chemical Engineering Departments. In particular, I would like to thank Prof. Anthony Zander, Tracy Miller, Fei Gao, Stephen Slape, Wendy Brown, Sophie Chen and Yvette Knapp; Billy Constantine, from the IT support group; Garry Clarke, Richard Pateman, Anthony Herzich, Pascal Symons, Philip Schmidt, Norio Itsumi, Derek Franklin, Lydia Zhang and Jason Peak from the workshops, for their constant support throughout the course of this work.

I am also grateful towards my friends, particularly Lloyd Fletcher, Yang Sun, Zifeng Wu, Gema Nadal, Shuye Tian, Ashley Chadwick, Michael Bolzon, John Redmond, Xiao Chen, Gary Cai, Chia Xiong Thong, Manabendra Saha, Saleh Mahmoud, Rahim Kurji, Michael Evans, Kae Ken Foo and Jingjing Ye, for their support and companionship. Above all, I must express my gratitude towards my family for their endless support. Without them, none of this would have been possible.

Abstract

Temperature may be considered the most important combustion parameter owing to its exponential influence on chemical reaction rates and on the formation of combustion products. However, reliable and detailed experimental temperature measurements are limited. Therefore, there is a strong need to develop a reliable temperature measurement technique for combustion environments that is relevant to practical devices such as turbulent sooting flames. This dissertation reports further development and application of a laser-based instantaneous temperature imaging technique called Non-linear excitation regime Two-Line Atomic Fluorescence (NTLAF) of indium in four journal papers. This dissertation, first, provides a new understanding of the mechanisms behind a novel seeding method employed in the NTLAF technique. Second, new knowledge of interferences to the indium fluorescence in highly sooting flames was reported and an effective means to improve the precision and accuracy of the NTLAF technique was demonstrated. Third, the accuracy of the improved NTLAF technique in turbulent sooting flames was assessed by comparing results with those obtained by the German Aerospace Centre (DLR) group using an independent technique. Finally, a line-wise NTLAF technique, which enables flame temperature measurement in highly sooting flames under high-flux irradiation, has been demonstrated.

The mechanisms of a novel seeding arrangement for the NTLAF technique, indium nanoparticles seeding, have been investigated. It was found that the NTLAF signal generation is associated with the vapourisation of indium nanoparticles into the gas phase by thermal decomposition. In addition, laser-induced *in-situ* ablation of the indium nanoparticles within the flame can be a further source of indium fluorescence. This is only significant in the low temperature regions of the flame that are also near to the base of the flame and is expected to generally have only a small influence on the NTLAF's accuracy since these regions are mostly at a temperature that is below the threshold of the NTLAF technique of $\sim$ 800 K.

Spatially- and temporally-resolved spectral measurements were employed to characterise the spectral interferences to indium fluorescence. A set of narrow-band filters with a bandwidth of ~ 1.2 nm (full-width at half-maximum, FWHM) and a high peak transmission of $\sim 95\%$ was then used to suppress interferences based on the spectral characteristics of the interferences. In comparison to a previous NTLAF configuration with broad-band band-pass filters employed (FWHM = 10 nm and transmission of $\sim 50\%$), it was found that the measurement accuracy was improved from 198 K to 10 K at a location where the soot volume fraction is 1.2 ppm. An average reduction of 40% in the standard deviation of measured temperature in single-shot measurements has also been achieved with the use of high transmission filters.

The accuracy of the improved NTLAF technique was assessed by performing planar measurements of temperature in a well characterised, lifted ethylene jet flame with a peak mean soot volume fraction of ~ 0.52 ppm and comparing these results with previous measurements obtained by the DLR group with Coherent Anti-Stokes Raman Scattering (CARS). Good agreement was found between the temperature results obtained with these two techniques, especially within a large central region of the flame in which a high probability of strong NTLAF signal occurs. In addition, measurements of planar soot volume fraction were simultaneously performed with the temperature measurements. It has been found that the joint probability of temperature and soot volume fraction depends more strongly on axial than on radial distance, consistent with previous trends found in other flames.

A line-wise NTLAF technique has also been developed to enable flame temperature measurement in highly sooting flames under high-flux irradiation, which is relevant to conditions in high temperature, solar receiver-combustors. Flame temperature was measured at various heights, with and without high-flux irradiation. The strong scattering interference to the NTLAF signal from the irradiated soot particles was accounted for by subtracting the scattering background. At a flame height of 40 mm and $r = 0$ mm, the temperature measurement probability distribution had a standard deviation of 40 K, or 2.2%, while the measurement accuracy due to the presence of unaccounted spectral interferences was about $\pm$ 45 K. The high-flux solar irradiation was also found to increase the temperature of the flame by up to ~ 100 K at heights above burner (HAB) between 26 mm and 41 mm and by ~ 50 K elsewhere on the centreline. The radial profiles of temperature show similar trends.

The first contribution of this dissertation is that the mechanisms of a

novel seeding method for the NTLAF technique, indium nanoparticles seeding, have been found to be associated with vapourisation and *in-situ* laser ablation of indium nanoparticles. The influence of this seeding method on the accuracy of the NTLAF technique was found to be negligible in the regions where the indium nanoparticles decompose completely. The second major contribution is characterisation of the interferences to the indium fluorescence for the NTLAF technique, which leads to the improvement of accuracy and precision of the NTLAF technique in highly sooting flames with the use of a set of narrow-band filters. The accuracy and precision of the improved NTLAF technique for turbulent sooting flames was then assessed by performing temperature measurements in a well characterised, lifted ethylene jet flame and comparing temperature results with previous CARS data. This comparison confirms good agreement between the two methods within a large central region of the flame. Soot volume fraction measurements were simultaneously performed in this flame to advance understanding of soot evolution in turbulent sooting flames. It has been found that the joint probability of temperature and soot volume fraction depends more strongly on axial than on radial distance. Lastly, a line-wise NTLAF technique has also been developed to enable temperature measurement in highly sooting flames under high-flux irradiation, which is relevant to conditions in high temperature, solar receiver-combustors.

List of papers

[1] D. Gu, Z. Sun, P. R. Medwell, Z. T. Alwahabi, B. B. Dally, G. J. Nathan, Mechanism for laser-induced fluorescence signal generation in a nanoparticle-seeded flow for planar flame thermometry, Applied Physics B 118 (2) (2015) 209–218.

[2] D. Gu, Z. Sun, G. J. Nathan, P. R. Medwell, Z. T. Alwahabi, B. B. Dally, Improvement of precision and accuracy of temperature imaging in sooting flames using two-line atomic fluorescence (TLAF), Combustion and Flame 167 (2016) 481 – 493.

[3] D. Gu, Z. Sun, B. B. Dally, P. R. Medwell, Z. T. Alwahabi, G. J. Nathan, Simultaneous imaging of flame temperature and soot volume fraction in a sooting lifted turbulent jet diffusion flame, Proceedings of the Combustion Institute 36, submitted 4 December 2015.

[4] D. Gu, Z. Sun, G. J. Nathan, X. Dong, B. B. Dally, P. R. Medwell, Z. T. Alwahabi, Optical thermometry for sooting flames under high-flux irradiation, Solar Energy, submitted 25 May 2016.

Other publications

[1] X. Dong, Z. Sun, D. Gu, P. J. Ashman, Z. T. Alwahabi, B. B. Dally, G. J. Nathan, The influence of high flux broadband irradiation on soot concentration and temperature of a sooty flame, Combustion and Flame 171 (2016) 103–111.

[2] Z. Sun, D. Gu, G. J. Nathan, Z. T. Alwahabi, B. B. Dally, Single-shot, time-resolved planar laser-induced incandescence (TiRe-LII) for soot primary particle sizing in flames, Proceedings of the Combustion Institute 35 (3) (2015) 3673–3680.

[3] Z. Sun, Z. T. Alwahabi, D. Gu, S. M. Mahmoud, G. J. Nathan, B. B. Dally, Planar laser-induced incandescence of turbulent sooting flames: the influence of beam steering and signal trapping, Applied Physics B 119 (4) (2015) 731–743.

[4] X. Dong, Z. Sun, G. J. Nathan, P. J. Ashman, D. Gu, Time-resolved spectra of solar simulators employing metal halide and xenon arc lamps, Solar Energy 115 (2015) 613–620.

[5] X. Dong, G. J. Nathan, Z. Sun, P. J. Ashman, D. Gu, Secondary concentrators to achieve high flux radiation with metal halide solar simulators, Journal of Solar Energy Engineering 138 (4) (2016) 041001.

[6] X. Dong, G. J. Nathan, Z. Sun, D. Gu, P. J. Ashman, Concentric multilayer model of the arc in high intensity discharge lamps for solar simulators with experimental validation, Solar Energy 122 (2015) 293–306.

[7] X. Dong, G. J. Nathan, S. M. Mahmoud, P. J. Ashman, D. Gu, B. B. Dally, Global characteristics of non-premixed jet flames of hydrogen–hydrocarbon blended fuels, Combustion and Flame 162 (4) (2015) 1326–1335.

Contents

List of Figures

Chapter 1

Introduction

1.1 Background

According to World Energy Outlook 2014 [1], the combustion of fossil fuels such as coal, oil, natural gas, bitumen and carbon-containing wastes accounts for 82% of the thermal energy used world-wide to generate electricity or support heat-dependent industrial processes. The World Energy Outlook 2014 also predicts that fossil fuels will continue to remain the dominant sources of energy in 2040, only falling from 82% to 80% in the Current Policies Scenario and to 74% in the New Policies Scenario, with slight changes to shares of the energy mix. Furthermore, combustion also plays an important role in the production and utilisation of renewable fuels such as biomass and hydrogen. Despite the ever-increasing importance of other renewable energy sources such as solar and wind, combustion will remain important for the foreseeable future. Therefore, in the face of the human health effects and environmental impacts of fossil fuel combustion [2–4], it is important to develop and refine current combustion technologies, including gas turbines, furnaces, and large-scale combustion systems, to ensure that they are efficient, effective and substantially cleaner than those currently in use.

Turbulent non-premixed flames that contain soot are employed in a large number of practical combustion processes. Soot that forms during the combustion processes results from the incomplete combustion of fossil fuels and other organic sources. The formation, growth, transportation and destruction processes of soot involves complex and concurrent three-phase physical and chemical processes [5–8]. Although soot formation is desirable in certain applications, such as industrial furnaces, since the presence of soot

greatly enhances radiative heat [9], it is often an undesirable combustion product, one that impedes overall combustion efficiency, for examples, in engines and gas turbines [10, 11]. The exhaust emissions of soot along with various gaseous products that are strongly coupled with the processes of soot formation, growth and oxidation, pose significant environmental challenges and health risks [2–4, 12]. Therefore, the study of the fundamental processes of turbulent non-premixed flames that contain soot remains important from practical, economic, environmental and safety standpoints.

Over the past two decades, numerous investigations of soot formation, growth and oxidation employing experimentation and computational modelling have advanced the understanding of sooting flames [13–20]. Among these experiments and ongoing research studies, laser diagnostic techniques have been playing an important role in providing a detailed understanding of combustion processes. Laser diagnostic techniques can deliver *in-situ*, non-intrusive, planar, and instantaneous measurements of many important parameters of interest with desired spatial and temporal resolution; they also provide high measurement selectivity and sensitivity [21–25]. Recent advances in laser diagnostics techniques enable the measurement of primary soot particle diameter (d_p) [26–30], soot volume fraction (f_v) [20, 29, 31–35], velocity (v) [18, 19, 36], and temperature (T) [12, 18, 19, 33–35] in flames. However, detailed investigations of turbulent flames that contain soot and other particulates still remain limited. This is because strong optical absorption, scattering, and other interferences associated with the presence of soot particles and their precursors, or of other particles, present difficulties for laser diagnostic techniques, resulting in slow advances in understanding flames that are not free of soot [25]. In spite of significant advances in the computational power and sophistication of computational methods, the present ability to predict the behavior of complex turbulent combustion remains limited [24]. Moreover, the development of such models has been limited by the availability of sufficiently reliable and detailed experimental data. Therefore, to advance our understanding of soot evolution in flames, there is an urgent need to develop reliable laser-based diagnostic techniques that can be applied in sooting flames.

To understand soot evolution in turbulent flames, **instantaneous and planar** measurements are highly desirable, as these provide better insight than point-wise measurements on the scalar gradients in the field of view. It is also highly desirable that such measurements not only be well resolved spatially and temporally but that they record **multiple parameters simultaneously**. This is necessary due to the complex coupling between

soot, turbulence, radiation and chemistry. Of these, two of the parameters of greatest interest are **soot volume fraction (f_v)**, which characterizes the amount of soot in the flame, and **flame temperature (T)**, on which all reaction rates depend. However, only a few simultaneous measurements of these two parameters in well-characterised turbulent flames [12, 33, 37] and in JP8 pool fires [34, 38] have been reported and none of these are spatially well-resolved or of known absolute accuracy. Therefore, there is a need, first, to assess measurement accuracy through independent measurements of **soot volume fraction** and **flame temperature** using non-intrusive, laser-based diagnostic techniques and, second, for the provision of new insight and data, through the simultaneous and planar measurement of these parameters.

While soot volume fraction can be measured using the relatively mature laser-induced incandescence (LII) technique, laser-based thermometry techniques require substantial further development owing to the strong interference encountered in the measurements from soot particles and their precursors. Among available laser-based thermometry techniques, two-line atomic fluorescence (TLAF) using seeded atomic indium as a tracer has been demonstrated to potentially provide planar temperature information in sooting flames, taking advantage of its strong atomic LIF signal and its sensitivity to flame temperatures between 800 K and 2800 K [39, 40]. However, in large-scale turbulent flames, single-shot TLAF measurements are difficult to implement when a relatively low laser fluence is used. This is because it is difficult to sufficiently seed indium in these flames. Therefore, the non-linear excitation regime TLAF (NTLAF) and saturated TLAF regime (sTLAF) have been developed to improve the signal and, with it, the signal-to-noise ratio (SNR) [41–44]. Despite the advantages of NTLAF and sTLAF, using relatively high laser fluence can enhance the SNR and thereby enable single-shot measurements; high laser fluence also generates large interferences in flames with high soot loading. However, these approaches have had limited applicability in previous investigations of flames with soot volume fractions of less than $\sim$ 1 ppm [35, 43, 45]. Hence, to improve the accuracy and precision of the measurements, these interferences must be suppressed. The objective for the present work is, therefore, to broaden the range of applicability of the NTLAF technique in turbulent sooting flames with a peak soot volume fraction of several parts per million (ppm).

A key challenge identified in previous experiments with large-scale turbulent flames using the NTLAF technique is that of seeding indium atoms into the flames to achieve a satisfactory SNR for single-shot imaging while also minimising other influences on the flame. A novel seeding

arrangement in which a laser ablation seeder can be used to produce indium nanoparticles for seeding has been developed to meet these desirable seeding characteristics [46, 47]. It has been found that the influence of the nanoparticle seeding on the flames was negligible and sufficient SNR for single-shot imaging can be achieved [48]. However, the evolution of the indium nanoparticles through the flame, the mechanisms by which neutral indium atoms are generated in and transported through the flame as well as its possible influences on the NTLAF technique, are unknown. Therefore, there is a need for new knowledge of nanoparticle seeding for NTLAF thermometry.

The development of techniques that integrate concentrating solar thermal (CST) and combustion technologies has driven growing interest in the impact of concentrated solar irradiation on flames. One of such technologies is the hybrid solar-thermal receiver-combustor (HRC) [49], which integrates combustion into a solar cavity receiver to allow the two energy sources to be harvested in a single device, which results in some periods of operation in which the flame is irradiated with high-flux, broad-band irradiation. To optimize the design of the HRC, especially for the mixed mode of operation with both CST and combustion, a detailed understanding of the interactions between the flame and the concentrated solar thermal energy is required. These complex interactions involve the non-linearly coupled processes of heat transfer, turbulence and chemistry, which are all dependent on flame temperature. It is therefore important to measure temperature distribution in this challenging environment with high temperatures and high-flux irradiation.

Laser diagnostic tools are preferred over intrusive probes in such high temperature environments owing to their non-intrusive nature and good temporal and spatial resolution [22, 24, 25, 50]. However, the additional scattering interference from particles and burner components is too strong for many of these laser-based optical methods to be applied reliably. For example, filtered Rayleigh scattering thermometry suffers from a low signal-to-interference ratio (SNR) even in sooting flames without additional irradiation. Coherent Anti-Stokes Raman Spectroscopy (CARS) has been demonstrated to measure the gas temperature of a reacting flow in a solar receiver/reactor to study gas phase chemical reactions in a high temperature environment, but this has only been demonstrated in an environment without any soot particles and was limited to single-point measurements [51]. Thermometry with laser-induced fluorescence (LIF), such as TLAF, has shown potential for such measurements because its signal is collected at a wavelength shifted away from that of excitation [39, 40, 43, 44, 48, 52]. However, the potential of

TLAF to perform temperature measurements in sooting flames under strong external irradiation has yet to be assessed. The final aim of this dissertation is to investigate this feasibility, measurement precision and accuracy of the TLAF technique applied to such environment.

1.2 Aims

The aim of this dissertation is to develop and apply an effective single-shot temperature imaging technique for turbulent sooting flames, with a peak soot volume fraction (f_v) of several parts per million. The specific aims of this dissertation are as follows:

- to advance the understanding the mechanisms of the nanoparticle seeding technique and to identify possible influences of nanoparticle seeding method on the NTLAF technique;

- to assess the sources and characteristics of interferences to both the Stokes and anti-Stokes LIF signals in highly sooting flames with peak soot volume fractions of several parts per million;

- to identify a means to improve the signal-to-interference ratio (SIR) in highly sooting flames and to assess the efficacy of the adopted means for reducing error in the resulting temperature measurement;

- to assess the accuracy of the improved NTLAF technique in a well-characterised turbulent sooting flame through a comparison with previous measurements of temperature using CARS and to increase the understanding of soot evolution in well-characterised flames from simultaneous and planar measurements of the joint probability density function (PDF) statistics of temperature and soot volume fraction;

- to perform temperature measurements in highly sooting laminar flames under strong interference from high-flux irradiation using a line-wise NTLAF configuration and to assess the precision and accuracy of the NTLAF technique.

1.3 Dissertation Layout

This dissertation consists of seven chapters and constitutes a compilation of journal papers (published and under review). Following this chapter, Chapter 2 provides a summary of the relevant background literature and a critical review of laser-based thermometry techniques for combustion research about sooting flames. The literature review reveals that there is an urgent need for improvement of the precision and accuracy of the thermometry technique in turbulent flames with soot loadings of several parts per million.

Reporting on the novel seeding method employed in the NTLAF technique described in the subsequent chapters, Chapter 3 addresses the first aim of the present work. This novel seeding method involves seeding indium nanoparticles into flames, which are produced using an in-house seeder via laser ablation. The chapter, more specifically, reports the mechanisms of atomic indium generation for indium LIF from indium nanoparticles. The influences of this seeding method on the NTLAF technique are also reported.

Chapter 4 addresses the second and third aims of the present work, assessing the characteristics of interferences to both the Stokes and anti-Stokes LIF signals in highly sooting flames with peak soot volume fractions of several parts per million, as assessed through spatially- and temporally-resolved spectral measurements. The utilisation of a set of narrow-band filters (FWHM $\sim$ 1.2 nm) with high peak transmission ($\sim$ 95%) for signal collection and interference suppression is also assessed. Temperature measurements obtained with narrow-band filters (FWHM $\sim$ 1.2 nm) and conventional band-pass filters (FWHM $\sim$ 10 nm), in both a soot-free flame and a sooting flame, are reported and compared.

Chapter 5 addresses the fourth aim of the present work. Simultaneous measurements of temperature and soot volume fraction in a well-characterised, lifted ethylene jet flame with a peak soot volume fraction of several parts per million were performed using the improved NTLAF technique.

Chapter 6 reports the development of a line-wise NTLAF technique to measure flame temperature in a laminar non-premixed ethylene sooting flame under strong interference from high-flux, broad-band irradiation, which is relevant to conditions in high temperature, solar receiver-combustors. For this experiment, flame temperature was measured at various heights, with

and without the high-flux irradiation.

Finally, Chapter 7 presents conclusions and recommendations for future work based on this research.

Chapter 2

Literature Review

2.1 Thermometry in sooting flames

Temperature is one of the key controlling parameters of the combustion process. It determines the overall efficiency of combustion process and exponentially influences all the chemical reactions responsible for radiation heat transfer and the formation of combustion products, including pollutants and soot particles [53]. In the context of this project, a fundamental understanding of soot formation, growth, and oxidation processes in turbulent sooting flames is needed. This requires an accurate and reliable measurement of flame temperature.

Due to their ability to provide non-intrusive measurements, **laser diagnostic techniques** have been under continuous development for the past few decades. They are particularly suitable for this study because they can deliver *in-situ*, planar and instantaneous measurements of many important parameters of interest with desired spatial and temporal resolution; they can also provide high measurement selectivity and sensitivity [21–25]. However, it is difficult to apply these techniques for temperature measurements in strongly sooting flames owing to the strong absorption, spectral interference from particulate scattering, and fluorescence from large molecule that occurs in such flames [25].

2.2 Laser-based thermometry techniques

To meet the requirements for both instantaneous and planar measurements of temperature in combustion, several laser-based techniques have been

developed. These include Rayleigh scattering (RS) [54–58], Coherent Anti-Stokes Raman Spectroscopy (CARS) [59], two-line laser induced fluorescence (LIF) using OH [60], two-line fluorescence from atomic indium [35, 39–44, 48, 52] and multi-line LIF NO [61, 62]. All of these techniques generally work well in soot-free flames or flames with a low soot loading. However, in the more challenging environments of highly sooting turbulent flames, due to the presence of soot particles and their precursors, the application of these laser-based optical methods is limited by strong interferences, including elastic and inelastic laser scattering.

Rayleigh scattering-based thermometry detects the elastic scattering signal of a cross-section of a gas mixture by molecules to give a measurement of the total number density. Assuming a constant pressure and applying the ideal gas law, a temperature can be deduced in this way because it is inversely proportional to the Rayleigh signal [54, 57, 58]. However, Rayleigh scattering does not convey any information on the nature or the temperature of the probed molecules. Especially in complex environments such as a turbulent gas mixture, instantaneous and complete characterisation of the mixture and the cross-section of all its constituents must be known to determine the temperature. In addition, Rayleigh scattering measurements can only be employed under very clean, particle free conditions because Mie scattering from particles is ten to twenty orders of magnitude more intense than Rayleigh scattering [21]. Therefore, Rayleigh scattering is only applicable in a restricted monitored combustion environment [21, 23, 25]. Filtered Rayleigh scattering (FRS), which allows accurate planar temperature measurements in weakly sooting flames, has been developed to circumvent problems associated with elastic scattering [55, 56]. However, FRS suffers from reduced SNR in flames with high soot loadings [21, 54].

Coherent Anti-Stokes Raman Spectroscopy (CARS) has proved its usefulness for accurate point-wise thermometry in various temperature and pressure ranges of practical combustion systems, including gas turbine combustors [63], liquid fuel combustors [64] and sooting turbulent pool fires [65]. CARS offers a stronger signal and is more applicable to luminous and particle laden flows than Rayleigh scattering-based thermometry [66] and can provide a high precision temperature measurement, making it an attractive technique [67]. Nonetheless, the necessity for line-of-sight optical access in this technique, its experimental complexity (including saturation by Raman pumping, the effects of the laser mode and SNR limitations), its lack of spatial fidelity in areas with a high temperature gradient in comparison to planar techniques, its subjection to differential beam steering

and its differential attenuation all restrict the generic application of CARS in turbulent, large-scale applications [23]. Similarly, while two-dimensional CARS is an exciting technique under development, it is yet to be tested with sooting flames [59].

Various laser-induced fluorescence (LIF) approaches for thermometry have also been attempted based either on a naturally occurring species such as NO [61, 62, 68] and OH [69, 70] or on seeded atoms [71]. However, due to the low prevailing temperatures and low levels of oxidising species present, OH exhibits low concentrations in fuel-rich and sooting flames [69]. These problems can be partially overcome by seeding the combustion process with suitable atoms as thermometry markers. Experiments in fuel-rich flames have been performed based on thermally assisted fluorescence of gallium atoms [72]. The disadvantage of thermally assisted fluorescence is that knowledge of the collisional cross-subsections of all involved species is required. Unfortunately, in highly sooting turbulent flames, this parameter is difficult to assess. In contrast, two-line atomic fluorescence (TLAF) using seeded atomic indium as a tracer, taking advantage of its strong LIF signal and its sensitivity to flame temperatures between 800 K and 2800 K, has been used to provide instantaneous planar temperature measurements in sooting flames [39, 40]. However, the precision and accuracy of TLAF when applied to single-shot temperature imaging in highly sooting flames with a peak soot volume fraction of several part per million, is yet to be investigated.

2.3 Two-line Atomic Fluorescence

Over the last two decades, two-line atomic fluorescence (TLAF) has evolved to become one of the most applicable techniques for measuring temperature in particle-laden flows, especially sooting flames [23, 39, 40, 52]. Omenetto *et al.* [72] have developed point TLAF thermometry technique using thallium as the seeding species and a compact arc lamp for excitation. Zizak *et al.* [73] and Joklik *et al.* [71] investigated different excitation sources and compared the accuracy of TLAF with other thermometry methods, finding that a more intense excitation source, such as a pulsed dye laser, could overcome many of the physical limitations of a vapour discharge lamp. Advancements in both laser technology and digital imaging have made TLAF a viable temporally- and spatially-resolved temperature measurement technique for flames. Engström *et al.* [39] and Nygren *et al.* [40], for instance, have demonstrated that linear excitation regime TLAF with indium holds

promise for temperature measurements in highly sooting flames with simple burner configurations. Hult *et al.* [74] have developed a pointwise TLAF system with the use of two extended-cavity diode laser systems (ECDLs). Chrystie *et al.* [75] further developed this TLAF configuration to enable a repetition rate of 3.5 kHz with a precision of 1.5% at 2000 K in laminar methane/air flames. Through the evolution of the TLAF technique, the robustness and the accuracy of planar TLAF measurements have been significantly improved, making TLAF an attractive thermometry technique for temperature diagnostics in turbulent sooting flames.

In comparison with other laser-based thermometry techniques, TLAF offers several distinct advantages that make it a promising technique for temperature measurements in particle-laden environments (e.g., sooting flames). First, TLAF allows for measurements in systems with inhomogeneous distributions of seeded species concentrations, which is typical of turbulent environments. Second, TLAF is insensitive to collisional quenching effects between seeding species and other species in flames, because the temperature is derived from taking the ratio of the two fluorescense signals, i.e. same quenching behavior. Third, the inelastic nature of its excitation and detection scheme allows each LIF signal to be separated from spurious scattered interference, such as the effects of Rayleigh scattering, Mie scattering, and window and wall scattering. However, most TLAF measurements have been performed in laminar flames with time-averaged results are reported [39, 40, 74, 75]. It is, therefore, worthwhile to extend existing TLAF techniques to enable single-shot temperature measurements in turbulent flames with high soot loadings, which are of relevance to industrial combustion systems.

The first limitation of applying earlier TLAF configurations to large-scale turbulent sooting flames for single-shot temperature imaging is to achieve a sufficient signal and, therefore, a sufficient SNR. Despite efforts to develop a variety of seeding methods to provide a sufficient indium concentration [43, 44, 46, 47, 76–78], it remains difficult to achieve sufficient SNR for single-shot imaging in large-scale turbulent flames without adversely impacting these flames [48]. An alternative approach to achieving sufficient SNR for single-shot imaging is to extend the excitation laser fluence from the linear regime into the non-linear excitation regime TLAF (NTLAF) [35, 41–43, 48] and the saturated TLAF regime (sTLAF) [44]. When high excitation laser spectral power density is employed, the non-linear excitation regime is approached so that the populations in the excited states are comparable to those in the ground state and the decay in excited state atoms by stimulated

emission becomes non-negligible compared to spontaneous emission. In a previous study [41], it was shown that the NTLAF technique could be used to provide a significantly improved SNR over the TLAF technique, improving single-shot precision from $\sim$ 250 K for the TLAF technique to $\sim$ 100 K for the NTLAF technique. The accuracy of the NTLAF technique demonstrated in [48] has been assessed by comparing temperature measurements with previous single-point measurements obtained by planar Rayleigh scattering measurements [79], in a well-characterised turbulent non-premixed flame known as TNF DLR-A. It was found that the NTLAF temperature results generally agreed with previous Rayleigh scattering data to within approximately $\sim$ 100 K, indicating that NTLAF is a suitable means for providing instantaneous imaging in non-premixed turbulent flames.

Despite the advantages that NTLAF could achieve sufficient SNR to enable single-shot planar measurements in large-scale turbulent flames [43, 48], this NTLAF configuration was found to be susceptible to interference from soot particles and their precursors in highly sooting flames [45]. In previous investigations [35, 43, 45], it was found that the applicability of this NTLAF configuration in sooting flames was limited to a soot volume fraction of less than $\sim$ 1 ppm. This is because the high laser fluence employed in these techniques may also generate large interferences in flames with high soot loading. Chan *et al.* assessed the magnitude of interference on the NTLAF measurements in a set of laminar non-premixed ethylene/air flames [45], recording the radial profiles of emissions with on-resonant and off-resonant laser excitation (for indium) and comparing these with laser-induced incandescence (LII) signals. Measurements were performed for both the Stokes and anti-Stokes processes, with laser line widths of 0.4 cm^{-1} (Stokes) and 0.3 cm^{-1} (anti-Stokes). Prompt laser-induced emissions were collected using optical filters with a bandwidth of $\sim$ 10 nm and a camera gate-width of 50 ns. The interferences were found to account for more than 50% of the collected signal in regions where the soot volume fraction (f_v) was 3.4 part per million. These significant interferences can lead to an unacceptable error of 200% in the derived temperature, making it impossible to perform reliable NTLAF measurements in highly sooting flames with this optical arrangement. Therefore, new methods are needed to suppress, or correct for, these significant interferences. However, no details on the temporal or the spectral characteristics of these interferences in sooting flames are available from which to develop improved optical methods. For this reason, one aim of the present work is to determine the spectral interferences and to implement a suppression/correction scheme that allows the extension of the usable range of the NTLAF technique to flames of higher soot loadings.

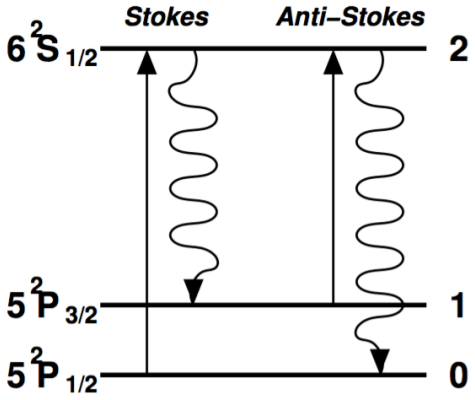

Figure 2.1: Three-level model of indium showing direct-line fluorescence (non-resonance fluorescence) involved in TLAF energy transitions. The laser excitation transitions are denoted by arrows pointing upwards. The fluorescence transitions are indicated by arrows pointing downwards.

2.3.1 Measurement scheme for TLAF

In previous studies [23, 39, 40], indium has been identified among the available atomic species as a prime thermometry candidate since it has a suitable excitation and detection scheme and good sensitivity over a temperature range 800 to 2800 K at pressures up to 14 bar, which is nearly the entire range of temperatures encountered in practical combustion [52]. In a TLAF measurement using indium as a tracer species, the two laser wavelengths typically chosen to excite atomic indium to the same upper state are 410.18 nm and 451.13 nm, as shown in Figure 2.1. The corresponding fluorescence at 451.13 nm (Stokes signal) and at 410.18 nm (anti-Stokes signal) have been collected through band-pass filters to suppress both the spontaneous emissions from the flame and the laser scattering from particles. A temporal separation between the two excitation pulses was introduced to suppress the spurious scattering that results from excitation and collection at the same wavelength. The time separation also allows for thermal equilibrium to be restored before the second laser pulse arrives. It is assumed that the seeding species atoms are in local thermal equilibrium with their surrounding environment and, hence, that a gas temperature can be obtained.

Temperature expression in the non-linear excitation regime is given by:

$$T = \frac{\triangle E_{10}/k}{ln(F_{21}(I_{20}) \times (1 + \frac{C_S}{I_{20}})) - ln(F_{20}(I_{21}) \times (1 + \frac{C_A}{I_{21}})) + ln(C_t)}. \quad (2.1)$$

Here T is the flame temperature, $\triangle E_{10}$ is the energy difference between levels 0 ($5^2P_{1/2}$) and 1 ($5^2P_{3/2}$), k is Boltzmann's constant, *F(I)* is used to correct for laser power variations during NTLAF measurements, where F is the function of LIF signals dependent on the laser power I, while C_S, C_A are calibration constants to describe the relationship between laser power and fluorescence signal and C_t is a system-dependent calibration constant that includes factors such as spectral overlap between laser and atomic line-widths, and detector and light collection efficiencies. These constants all need to be experimentally determined in the calibration.

2.3.2 Temperature calibration

To obtain the calibration function F and the calibration constants C_S and C_A for the Stokes and anti-Stokes processes, calibration curves between the LIF signal and laser energy were obtained by recording the LIF signal at different laser energies.

To obtain the system-dependent calibration constant, C_t, a soot-free, premixed C_2H_4/air flame was employed. The flow rates were 0.53 L/min for the C_2H_4 fuel, and 3.91 L/min and 127.7 L/min for the premixed air and co-flow air stream, respectively. The calibration flame temperature measurements were performed in the product zone of the calibration flame with a uniform temperature of 1840 K by using an *R*-type Pt/Pt-Rh 13% thermocouple with a wire diameter of 75 μm (Omega, P13R-003). The measurement was performed in the central region of the flame where the temperature is uniform. A temperature correction of 61 K was added to the raw measurement to correct for radiation heat loss from the thermocouple, following previous work [80].

2.3.3 Seeding arrangement for TLAF

In order to generate the TLAF signal, the seeding of neutral indium atoms into flames is required. It is important that this seeding achieves

a satisfactory signal-to-noise ratio (SNR) for single-shot imaging, and its influence on the combustion process to be negligible. This is particularly challenging in large-scale turbulent flames where the concentration of seeded indium decreases from the burner exit to the downstream locations and along the radial distance away from the centreline [48, 76].

Nebuliser seeding is a widely adopted seeding method for TLAF [39–43, 48, 52, 75, 76, 81]. Nebuliser seeding involves using a nebuliser to generate fine droplets of indium chloride ($InCl_3$) dissolved in a solvent with a typical concentration varying of 100 and 6000 mg/L [39, 40, 52, 75, 81]. The droplets are then filtered using a droplet selector [52] to avoid seeding large droplets into the flame and are transported by a carrier gas stream into the flame. As the droplets enter the flame and are heated, the solvent is evaporated and the remaining Indium complexes interact with the flame releasing Indium atoms. The concentration of indium salt dissolved in the solution and the amount of solvent being seeded into the flame is selected to generate enough laser-induced fluorescence (LIF) signal in the flame for a good SNR while keeping the quantity of seeded indium and solvent to a minimum.

The disadvantage of the nebuliser seeding approach is that the solvent inevitably changes the flame temperature, the stoichiometry and/or the soot concentration over that of the parent fuel. The flame temperature is changed because thermal energy is required to evaporate the droplets to produce atomic indium, which can also generate local thermal gradients. The addition of solvents such as methanol or distilled water typically reduces sooting propensity [82, 83]. For example, Engström *et al.* [39] reported a flame temperature reduction of 100-150 K in an acetylene/air flame resulting from the addition of the $InCl_3$ aqueous solution into the flame. For measurements in liquid-fuelled systems, this bias can be mitigated by dissolving the indium salt into the fuel [52, 84]. In addition, the detection region is limited to the high temperature fuel rich zone because indium is highly reactive under oxidising conditions. Due to the high thermal energy required to decompose the metal salt, the temperature detection threshold is $\sim$ 1000 K [81]. The major approaches to developing alternative techniques are that of ablation seeding of nanoparticles [46–48] and of seeding tri-methyl-indium [78].

Among alternative seeding techniques, the **direct seeding of indium nanoparticles** offers potential to seed pure indium while avoiding the disadvantages of other approaches, which introduce it as a compound.

Nanoparticles offers many desirable characteristics compared to macro-particles for direct seeding, including a lowered melting point [85], an increased absorption cross-section [86], increased reactivity as a result of a high specific surface area [87, 88] and high purity. Nanoparticles can be synthesised in a number of ways [89], among which laser ablation appears as an attractive option because it can deliver freshly produced nanoparticles of indium into the flame by passing the fuel stream through an ablation chamber. Laser ablation involves a series of complex physical and chemical processes including thermal vapourisation, plasma ignition, expansion and cooling, particle ejection, condensation, coagulation and aggregation [90–92]. Nanoparticles are formed through the interaction between the plasma and the ambient gas and the micron-sized particles formed from other mechanisms, including solid exfoliation, hydrodynamic sputtering and liquid droplet ejection [93]. However, none of the previous investigations of laser ablation have been performed under conditions of relevance to seeding flames for NTLAF measurements [90–93]. For these reasons, there is a need for new knowledge of nanoparticle seeding for NTLAF thermometry.

The use of laser ablation to generate nanoparticles from an indium rod has been demonstrated to provide a useful seeding technique for NTLAF [46–48]. In these studies, a 10 Hz (8 ns pulse duration) 532 nm beam from an Nd:YAG laser was focused onto an indium rod, which was rotated and translated in a sealed ablation chamber. Carrier gas was then used to transport the nanoparticles to the measurement volume. The technique was shown to generate an indium LIF signal at all measurement heights in the flame, including detection within the low-temperature regions of the jet flow or flame, which is not possible with nebuliser seeding. As no solvent is required, the influence of seeding on flame temperature and chemistry is significantly mitigated. Strong Mie scattering from the ablation products confirmed the presence of fine particles in the ablation products, which suggests that they may play an important role in the thermometry measurement. However, the form and the evolution of the nanoparticles through the flame, the mechanism(s) by which neutral indium atoms are generated in and transported through the flame, and the possible influences of nanoparticle seeding on the NTLAF technique has previously been unknown. Hence, the present work aims to provide this understanding.

2.3.4 Temperature measurement in sooting flames

Severe interference to the fluorescence signal from seeded indium has previously limited the application of current NTLAF to single-shot temperature imaging in low sooting flames. Chan *et al.* [45] assessed the magnitude of interference on the NTLAF measurements in a set of laminar non-premixed ethylene/air flames. They recorded radial profiles of emissions with on-resonant and off-resonant laser excitation (for indium) and compared these with laser-induced incandescence (LII) signals. Measurements were performed for both the Stokes and anti-Stokes processes, with laser line widths of 0.4 cm^{-1} (Stokes) and 0.3 cm^{-1} (anti-Stokes). Prompt laser-induced emissions were collected using optical filters with a bandwidth of $\sim$ 10 nm and a camera gate-width of 50 ns. The interferences were found to account for more than 50% of the collected signal in regions where the soot volume fraction was 3.4 ppm. These significant interferences can lead to an unacceptable error in the derived temperature of 200%. Hence, it is impossible to perform reliable NTLAF measurements in highly sooting flames with this optical arrangement and new methods are needed to suppress, or correct for, these significant interferences. However, no details of the temporal or spectral characteristics of these interferences in sooting flames are available from which to develop improved optical methods. For this reason, the first aim of the present investigation is to provide this new understanding.

Aside from laser elastic light scattering (ELS), interference on the NTLAF signals can be expected to arise from LIF from polycyclic aromatic hydrocarbons (PAH) and LII signals from soot particles in sooting flames. These interferences are generated simultaneously with the TLAF signals and exhibit broad-band spectra, which make them difficult to separate from the signal. The additional options with which it may be possible to enhance the suppression of these temporally- and spectrally- overlapped interferences, or to correct for them, are: (1) to correct the raw image with a separate image of the interference, acquired by exciting the flame with the same wavelengths as in the TLAF measurement and simultaneously detected at a different wavelength to the indium LIF line, e.g. using an interference filter centered at 430 nm; (2) to temporally suppress the interference by using a shorter camera gate width (for example, 10−30 ns); (3) to employ excitation lasers with narrow line widths; and (4) to employ narrower band-pass filters.

An image correction scheme based on interference subtraction was proposed by Chan *et al.* [45], in which an additional intensified CCD camera is introduced to record simultaneously the laser-induced interference at

a nearby detection wavelength, here at $\sim$ 430 nm. These off-resonance interferences can then be subtracted from the on-resonance signals, which contain both the pure indium LIF signals and the interferences. However, this correction method was found to be of little value for single-shot NTLAF applications in turbulent sooting flames, because the scatter in the spatial distribution and intensity between the on- and off-resonance images was too great to yield acceptable SNR in a turbulent non-premixed flame. This, in part, is because the interference subtraction method needs to be performed for both Stokes and anti-Stokes signals, thereby introducing another error associated with additional image acquisition and increasing the error of the derived temperature. Additionally, this correction scheme is complex because additional lasers and cameras are required. Temporal separation by means of a shorter gate width (for example, when comparing 15 ns to 30 ns) for the detector also offers some potential but is estimated to offer less than a factor of two improvement in signal-to-interference ratio (SIR). A laser with a line width narrower than $\sim$ 0.35 cm^{-1} (which is used in the NTLAF), e.g. a commercial dye laser with a typical line width of $\sim$ 0.1 cm^{-1}, can also be used to enhance SIR. This is because the same level of LIF signals of indium can be achieved at a lower total laser fluence compared to using a laser with a broader line width, hence with weaker interferences. However, the application of lasers with such a narrow line width also suffers from reduced spectral overlap between the laser line width and the indium absorption lines, which has a FWHM of $\sim$ 0.95 cm^{-1} for the Stokes process and 0.6 cm^{-1} for anti-Stokes at atmospheric pressure. Therefore, the LIF signal of indium also drops under these circumstances. This issue becomes worse in pressurized flames [74]. Alternatively, the utilization of filters with a bandwidth narrower than the conventional 10 nm, potentially offers a simple and suitable method for interference sup- pression. This is because the LIF from atomic indium has a narrow line width of $\sim$ 0.02 nm [74], while the interferences are spectrally broadband. For this reason, a set of customized filters with FWHM of $\sim$ 1.2 nm was chosen and manufactured to improve the precision and accuracy of the NTLAF technique in sooting flames via interference suppression. This study aims to assess the efficacy of the narrow-band filters for interference suppression and for reducing the measurement error to the resulting temperature measurement.

2.4 Measurements of flame temperature and soot volume fraction

A key statistical measurement in turbulent sooting flames that has very limited data is the joint probability density function (PDF) of temperature and soot volume fraction [12, 35]. Not only does the development of validated models require such data in a wide range of flames, but there is also a need to establish greater confidence in the available data with independent measurements. In particular, the simultaneous laser extinction (for soot volume fraction) and two-color pyrometry (for temperature of the soot) that have been measured in piloted ethylene jet flames [12, 33, 37] and also in JP8 pool fires [34, 38] were measured with an entirely different method, one that involved a semi-intrusive, two-ended optical-fiber probe with a laser beam having a path length of between 5 mm and 20 mm. The temperature measurements provided by Mahmoud *et al.* [35] have a relatively high uncertainty (180 K) because they were obtained with an earlier configuration of the NTLAF method in which the two temperature images were subjected to differential beam steering, being collected along different optical paths, and were also subjected to spectral interference. That method has recently been refined to suppress interference through the utilisation of narrow-band filters (FWHM $\sim$ 1 nm) with a high transmission ($\sim$ 95%) at the signal collection wavelength and a high optical density (OD) of 6.0 at the excitation wavelength [94]. Hence, meeting the need for reliable joint PDFs of temperature and soot volume fraction in well-characterised flames requires both by the need for complete data in well-characterised flames and a comparison of these with previous measurements of the joint PDF in other flames.

2.5 Temperature measurements in sooting flames under high-flux irradiation

There is growing interest in the impact of concentrated solar irradiation on flames that is driven by the development of techniques that integrate concentrating solar thermal (CST) and combustion technologies, such as the hybrid solar-thermal receiver-combustor (HRC) [49]. The HRC integrates combustion into a solar cavity receiver to allow the two energy sources to be harvested in a single device, which results in some periods of operation in which the flame is irradiated with high-flux, broad-band irradiation. Nathan *et al.* [95] evaluated the economic viability of the HRC concept and found that it offers significant potential advantages compared to an

equivalent solar-gas hybrid (SGH) between a stand-alone cavity receiver and a gas-fired boiler. These advantages include reduced capital costs and levelised costs of electricity resulting from the combination of lowered infrastructure cost and reduced net thermal losses [49, 95]. To optimize the design of the HRC, especially for the mixed mode of operation with both CST and combustion, a detailed understanding of the interactions between the flame and the concentrated solar thermal energy is required. These complex interactions involve the non-linearly coupled processes of heat transfer, turbulence and chemistry, which are all dependent on flame temperature. It is therefore important to measure temperature distribution in this challenging environment with high temperatures and high-flux irradiation.

Laser diagnostic tools are preferred over intrusive probes in high temperature environments such as combustion owing to their non-intrusive nature and good temporal and spatial resolution [22, 24, 25, 50]. However, the total radiative power in a direct hybrid system is an order of magnitude greater than the natural radiation from a sooting flame [95], given that the total thermal inputs from the two sources is comparable while the radiant fraction from a flame is typically 10-20% [96, 97]. Hence, the additional scattering interference from particles and burner components is too strong for many of these laser-based optical methods to be applied reliably. For example, filtered Rayleigh scattering thermometry suffers from a low signal-to-interference ratio (SNR) even in sooting flames without additional irradiation. Coherent Anti-Stokes Raman Spectroscopy (CARS) has been demonstrated to measure the gas temperature of a reacting flow in a solar receiver/reactor to study gas phase chemical reactions in a high temperature environment, but this has only been demonstrated in an environment without any soot particles and was limited to single-point measurements [51]. Thermometry with laser-induced fluorescence (LIF), such as two-line atomic fluorescence (TLAF), has shown potential for such measurements because its signal is collected at a wavelength shifted away from that of excitation [39, 40, 43, 44, 48, 52]. Moreover, the signal from seeded metallic species (usually indium) is much stronger than that from naturally occurring species such as OH and NO and is present in broader regions of a flame [25]. However, the potential of TLAF to perform temperature measurements in sooting flames under strong external irradiation has yet to be assessed. It is for this reason that the present work aims to develop a line-wise configuration of NTLAF under strong interference from high-flux irradiation in a highly sooting laminar flame and to assess the precision and accuracy of the resulting temperature measurements.

Chapter 3

Mechanism for laser-induced fluorescence signal generation in a nanoparticle-seeded flow for planar flame thermometry

Minor amendments to published paper:

The following sentence has been revised from: 'Nanoparticles possess many desirable characteristics over macro-particles for direct seeding, including: lowered melting point [17], increased absorption cross-section [18], increased reactivity as a result of high specific surface area [19, 20] and high purity.' to 'Nanoparticles possess many desirable characteristics over macro-particles for direct seeding, including: lowered melting point [17], increased reactivity as a result of high specific surface area [19, 20] and high purity.'

Statement of Authorship

Title of Paper	Mechanism for laser-induced fluorescence signal generation in a nanoparticle-seeded flow for planar flame thermometry
Publication Status	☑ Published ☐ Accepted for Publication ☐ Submitted for Publication ☐ Unpublished and Unsubmitted work written in manuscript style
Publication Details	Applied Physics B: Lasers and Optics

Principal Author

Name of Principal Author (Candidate)	Dahe Gu
Contribution to the Paper	Under supervision of G. J. Nathan, Z. W. Sun, P. R. Medwell, Z. T. Alwahabi and B. B. Dally, I developed experimental methods, performed experiments, analysed data and wrote the manuscript.
Overall percentage (%)	55%
Certification:	This paper reports on original research I conducted during the period of my Higher Degree by Research candidature and is not subject to any obligations or contractual agreements with a third party that would constrain its inclusion in this thesis. I am the primary author of this paper.
Signature	Date 27/01/2016

Co-Author Contributions

By signing the Statement of Authorship, each author certifies that:

i. the candidate's stated contribution to the publication is accurate (as detailed above);

ii. permission is granted for the candidate in include the publication in the thesis; and

iii. the sum of all co-author contributions is equal to 100% less the candidate's stated contribution.

Name of Co-Author	Graham J. Nathan
Contribution to the Paper	I acted as principal supervisor for the Ph.D. candidate, Dahe Gu, aided in development of the experimental methods, revision of the manuscript and evaluation of the final manuscript. I give consent to Dahe Gu to present this paper for examination towards the Doctorate of Philosophy.
Signature	Date 11/2/16.

Name of Co-Author	Paul R. Medwell
Contribution to the Paper	I acted as co-supervisor for the Ph.D. candidate, Dahe Gu, aided in revision of the manuscript and evaluation of the final manuscript. I give consent to Dahe Gu to present this paper for examination towards the Doctorate of Philosophy.
Signature	Date 11-FEB-2016

Name of Co-Author	Zeyad T. Alwahabi
Contribution to the Paper	I acted as co-supervisor for the Ph.D. candidate, Dahe Gu, aided in revision of the manuscript and evaluation of the final manuscript. I give consent to Dahe Gu to present this paper for examination towards the Doctorate of Philosophy.
Signature	Date: Feb 11, 2016

Name of Co-Author	Bassam B. Dally
Contribution to the Paper	I acted as co-supervisor for the Ph.D. candidate, Dahe Gu, aided in revision of the manuscript and evaluation of the final manuscript. I give consent to Dahe Gu to present this paper for examination towards the Doctorate of Philosophy.
Signature	Date: 4-2-16

Name of Co-Author	Zhi Wei Sun
Contribution to the Paper	I am a postdoc, co-supervised the experiments, aided in development of the experimental methods, performing experiments, data analysis and results discussion, revision of the manuscript and evaluation of the final manuscript. I give consent to Dahe Gu to present this paper for examination towards the Doctorate of Philosophy.
Signature	Date: 11/02/2016

Please cut and paste additional co-author panels here as required.

Gu, D.H., Sun, Z.W., Medwell, P.R., Alwahabi, Z.T., Dally, B.B. & Nathan, G.J. (2015). Mechanism for laser-induced fluorescence signal generation in a nanoparticle-seeded flow for planar flame thermometry.
Applied Physics B, 118(2), 209–218.

Chapter 4

Improvement of precision and accuracy of temperature imaging in sooting flames using two-line atomic fluorescence (TLAF)

Statement of Authorship

Title of Paper	Improvement of precision and accuracy of temperature imaging in sooting flames using two-line atomic fluorescence (TLAF)
Publication Status	☑ Published ☐ Accepted for Publication ☐ Submitted for Publication ☐ Unpublished and Unsubmitted work written in manuscript style
Publication Details	Combustion and Flame

Principal Author

Name of Principal Author (Candidate)	Dahe Gu
Contribution to the Paper	Under supervision of G. J. Nathan, Z. W. Sun, P. R. Medwell, Z. T. Alwahabi and B. B. Dally, I developed experimental methods, performed experiments, analysed data and wrote the manuscript.
Overall percentage (%)	55%
Certification:	This paper reports on original research I conducted during the period of my Higher Degree by Research candidature and is not subject to any obligations or contractual agreements with a third party that would constrain its inclusion in this thesis. I am the primary author of this paper.
Signature	Date: 27/01/2016

Co-Author Contributions

By signing the Statement of Authorship, each author certifies that:

i. the candidate's stated contribution to the publication is accurate (as detailed above);

ii. permission is granted for the candidate in include the publication in the thesis; and

iii. the sum of all co-author contributions is equal to 100% less the candidate's stated contribution.

Name of Co-Author	Graham J. Nathan
Contribution to the Paper	I acted as principal supervisor for the Ph.D. candidate, Dahe Gu, aided in development of the experimental methods, revision of the manuscript and evaluation of the final manuscript. I give consent to Dahe Gu to present this paper for examination towards the Doctorate of Philosophy
Signature	Date: 1/2/16

Name of Co-Author	Paul R. Medwell
Contribution to the Paper	I acted as co-supervisor for the Ph.D. candidate, Dahe Gu, aided in revision of the manuscript and evaluation of the final manuscript. I give consent to Dahe Gu to present this paper for examination towards the Doctorate of Philosophy.
Signature	Date: 11-FEB-2016

Name of Co-Author	Zeyad T. Alwahabi
Contribution to the Paper	I acted as co-supervisor for the Ph.D. candidate, Dahe Gu, aided in revision of the manuscript and evaluation of the final manuscript. I give consent to Dahe Gu to present this paper for examination towards the Doctorate of Philosophy.
Signature	Date: Feb 11, 2016

Name of Co-Author	Bassam B. Dally
Contribution to the Paper	I acted as co-supervisor for the Ph.D. candidate, Dahe Gu, aided in revision of the manuscript and evaluation of the final manuscript. I give consent to Dahe Gu to present this paper for examination towards the Doctorate of Philosophy.
Signature	Date: 4-2-16

Name of Co-Author	Zhi Wei Sun
Contribution to the Paper	I am a postdoc, co-supervised the experiments, aided in development of the experimental methods, performing experiments, data analysis and results discussion, revision of the manuscript and evaluation of the final manuscript. I give consent to Dahe Gu to present this paper for examination towards the Doctorate of
Signature	Date: 11/02/2016

Please cut and paste additional co-author panels here as required.

Combustion and Flame 167 (2016) 481–493

Contents lists available at ScienceDirect

Combustion and Flame

journal homepage: www.elsevier.com/locate/combustflame

Improvement of precision and accuracy of temperature imaging in sooting flames using two-line atomic fluorescence (TLAF)

Dahe Gu [a,b], Zhiwei Sun [a,b,*], Graham J. Nathan [a,b], Paul R. Medwell [a,b], Zeyad T. Alwahabi [a,c], Bassam B. Dally [a,b]

[a] Centre for Energy Technology, The University of Adelaide, S.A. 5005, Australia
[b] School of Mechanical Engineering, The University of Adelaide, S.A. 5005, Australia
[c] School of Chemical Engineering, The University of Adelaide, S.A. 5005, Australia

ARTICLE INFO

Article history:
Received 15 May 2015
Revised 15 September 2015
Accepted 23 September 2015
Available online 22 October 2015

Keywords:
Temperature
Laser diagnostics
Two-line atomic fluorescence
Soot

ABSTRACT

Severe interference to the fluorescence signal from seeded indium has previously limited the application of current non-linear excitation regime two-line atomic fluorescence (NTLAF) to low sooting flames. The present paper reports new details of these interferences, from spatially- and temporally-resolved spectral measurements in a laminar, non-premixed sooting C_2H_4 flame burning in air. Three types of interference to the indium LIF signal have been identified: laser-induced fluorescence (LIF) from polycyclic aromatic hydrocarbons (PAH), elastic laser scattering (ELS) and laser-induced incandescence (LII) from soot particles. This knowledge was used to propose new methods to suppress interferences and select customized narrow-band filters for the signal collection, with a narrow bandwidth of ~1.2 nm (full-width at half-maximum, FWHM) and a high peak transmission of ~95%. The efficacy of the narrow-band filters for interference suppression in planar NTLAF measurements was assessed by comparing these measurements with those obtained with a set of conventional band-pass filters (FWHM = 10 nm), in both a soot-free flame and a sooting flame. The application of the narrow-band filters was found to increase both the accuracy and the precision of the temperature measurement, so that measurement accuracy that is due to the presence of interferences has been improved from 198 K to 10 K at a location where the soot volume fraction (f_v) is 1.2 ppm. An average reduction of 40% in the standard deviation of measured temperature in single-shot measurements has also been achieved with the use of high transmission filters. With the use of narrow-band filters, NTLAF can be reliably applied in laboratory target sooting flames with peak soot volume fraction of several ppm.

1. Introduction

Planar measurements of temperature are highly desired in combustion research to advance the detailed understanding of combustion processes through the development and validation of computational models. This is because reaction rates typically scale non-linearly on temperature and in flames with thin reaction zones which have strong spatial gradients. Instantaneous, planar measurements are also desirable for the investigation of turbulent flames, which are prevalent in most practical combustion systems as they provide better insight than point-wise measurements on the scalar gradients in the field of view. To meet the requirement for both instantaneous and planar measurements of temperature in combustion, several laser-based techniques have been developed. These include Rayleigh scattering (RS) [1–5], two-dimensional coherent anti-Stokes Raman spectroscopy (2D-CARS) [6], two-line laser induced fluorescence (LIF) using OH [7], two-line fluorescence from atomic indium [8–15] and multi-line NO [16,17]. All of these techniques generally work well in soot-free flames or flames with a sufficiently low soot loading. However, in the more challenging environments of highly sooting turbulent flames, the application of these laser-based optical methods is limited by strong interferences including elastic laser scattering (ELS) due to the presence of soot particles and their precursors. For example, while filtered Rayleigh scattering (FRS) allows accurate planar temperature measurements in weakly sooting flames [1,2], it suffers from reduced signal-to-noise ratio (SNR) in flames with high soot loadings [5,18]. Similarly, while 2D-CARS is an exciting technique under development, it is yet to be demonstrated in sooting flames [6]. In contrast, two-line atomic fluorescence (TLAF) using seeded atomic indium as a tracer has been demonstrated to provide instantaneous planar temperature measurements in sooting flames, taking advantage of its strong atomic LIF signal and its sensitivity to flame temperatures between 800 K and 2800 K [9,14]. Meanwhile, a variety of seeding methods have been developed to provide sufficient

* Corresponding author. fax: +61 (0) 8 8313 4367.
E-mail address: zhiwei.sun@adelaide.edu.au (Z. Sun).

http://dx.doi.org/10.1016/j.combustflame.2015.09.028

indium concentration, to achieve good signal to noise ratio without impacting on the flames [8,19–23]. However, in large-scale turbulent flames, single-shot TLAF measurement is difficult to implement when relatively low laser power is used. This is because sufficient seeding of indium is difficult to achieve in these flames. Therefore, the non-linear excitation regime TLAF (NTLAF) and saturated TLAF regime (sTLAF) have been developed to overcome the low signal and hence low signal-to-noise ratio (SNR) [12,13,21]. In addition, the application of NTLAF and sTLAF techniques are expected to mitigate the effects of beam steering on florescence signal compared with the linear TLAF technique, especially in turbulent reacting flows [24]. This is because the fluorescence signal acquired in the non-linear/saturation regime is less sensitive to the change of excitation laser fluence caused by the beam steering effects compared with the fluorescence signal acquired in the linear excitation regime. Despite the advantage that the NTLAF and sTLAF using relatively high laser fluence can enhance the SNR to enable single-shot measurements and reduce the measurement uncertainty caused by beam steering effects, high laser fluence also generates large interferences in flames of high soot loading, which has limited the applicability of these techniques in previous investigations [25]. Hence, to improve the accuracy and precision of the measurements these interferences must be suppressed, which in turn requires more detailed understanding of their characteristics.

In a TLAF measurement, the two laser wavelengths typically chosen to excite atomic indium to the same upper state are 410.18 nm and 451.13 nm. The corresponding fluorescence at 451.13 nm (Stokes signal) and at 410.18 nm (anti-Stokes signal) have been previously collected through 10 nm (full width at half maximum, FWHM) band-pass filters to suppress both the spontaneous emissions from the flame and the laser scattering from particles. The ratio of these two signals is then used to determine the flame temperature. The alternate excitation and detection scheme, combined with a time separation (for example, ~100 ns) between the two fluorescence transitions, mitigates strong ELS of excitation beams by the particles in the measurement volume. In addition to ELS, other species in flames can also be simultaneously excited by the laser beams, which also causes interference on the TLAF signals [26–33]. In the linear excitation regime of TLAF measurements, it was found that such spectral interference to TLAF measurement is negligible [9,14,15]. This is because the electronic transitions of atomic indium are much stronger than that of other large species in the flame. However, this strong transition also leads to deviation from the linear excitation regime of atomic indium at relatively low laser fluence, which reduces the strength of the signal relative to the interferences in the NTLAF regime, especially in rich hydrocarbon flames such as ethylene flames with a peak soot volume fraction of a few ppm [25]. As a result, laser-induced emissions from other species become comparable in intensity with LIF from atomic indium in NTLAF measurements [25].

Chan et al. assessed the magnitude of interference on the NTLAF measurements in a set of laminar non-premixed ethylene/air flames [25]. They recorded radial profiles of emissions with on-resonant and off-resonant laser excitation (for indium) and compared these with laser-induced incandescence (LII) signals. Measurements were performed for both the Stokes and anti-Stokes processes, with laser line widths of 0.4 cm^{-1} (Stokes) and 0.3 cm^{-1} (anti-Stokes). Prompt laser-induced emissions were collected using optical filters with a bandwidth of ~10 nm and a camera gate-width of 50 ns. The interferences were found to account for more than 50% of the collected signal in regions where the soot volume fraction f_v was 3.4 ppm. These significant interferences can lead to an unacceptable error in the derived temperature of 200%. Hence, it is impossible to perform reliable NTLAF measurements in highly sooting flames with this optical arrangement and new methods are needed to suppress, or correct for, these significant interferences. However, no details of the temporal or spectral characteristics of these interferences in sooting flames are available from which to develop improved optical methods. For this reason, the first aim of the present investigation is to provide this new understanding.

Aside from ELS, interference on the NTLAF signals can be expected to arise from LIF from polycyclic aromatic hydrocarbons (PAH) and LII signals from soot particles in sooting flames. These interferences are generated simultaneously with the TLAF signals and exhibit broadband spectra, which make them difficult to separate from the signal. The additional options with which it may be possible to enhance the suppression of these temporally- and spectrally- overlapped interferences, or to correct for them, are: (1) to correct the raw image with a separate image of the interference, acquired by exciting the flame with the same wavelengths as in the TLAF measurement and simultaneously detected at a different wavelength to the indium LIF line, e.g. using an interference filter centered at 430 nm; (2) to temporally suppress the interference by using a shorter camera gate width (for example, 10–30 ns); (3) to employ excitation lasers with narrow line widths; and (4) to employ narrower band-pass filters.

An image correction scheme based on interference subtraction was proposed by Chan et al. [25], in which an additional intensified CCD camera is introduced to record simultaneously the laser-induced interference at a nearby detection wavelength, here at ~430 nm. These off-resonance interferences are then subtracted from the on-resonance signals, which contain both the pure indium LIF signals and the interferences. However, this correction method was found to be of little value for single-shot NTLAF applications in turbulent sooting flames [34], because the scatter in the spatial distribution and intensity between the on- and off-resonance images was too great to yield acceptable SNR in a turbulent non-premixed flame. This, in part, is because the interference subtraction method needs to be performed for both Stokes and anti-Stokes signals, thereby introducing another error associated with additional image acquisition and increasing the error of the derived temperature. Additionally, this correction scheme is complex because additional lasers and cameras are required. The potential of temporal separation by means of a shorter gate width (for example, when comparing 15 ns to 30 ns) for the detector also offers some potential but is estimated to offer less than a factor of two improvement in signal-to-interference ratio (SIR). A laser with a line width narrower than ~0.35 cm^{-1} (which is used in the NTLAF), e.g. a commercial dye laser with a typical line width of ~0.1 cm^{-1}, can also be used to enhance SIR. This is because the same level of LIF signals of indium can be achieved at a lower total laser fluence compared to using a laser with a broader line width, hence with weaker interferences. However, the application of lasers with such a narrow line width also suffers from reduced spectral overlap between the laser line width and the indium absorption lines, which has a FWHM of ~0.95 cm^{-1} for the Stokes process and 0.6 cm^{-1} for anti-Stokes at atmospheric pressure. Therefore, the LIF signal of indium also drops under these circumstances. This issue becomes worse in pressurized flames [35]. Alternatively, the utilization of filters with a bandwidth narrower than the conventional 10 nm, potentially offers a simple and suitable method for interference suppression. This is because the LIF from atomic indium has a narrow line width of ~0.02 nm [35], while the interferences are spectrally broadband. For this reason, a set of customized filters with FWHM of ~1.2 nm was chosen and manufactured to improve the precision and accuracy of the NTLAF technique in sooting flames via interference suppression.

For the reasons described, the aims of the present paper are threefold. The first aim is to assess the aforementioned sources of interferences to both the Stokes and anti-Stokes fluorescence signals through the examination of temporally- and spatially-resolved laser-induced emission spectra in a laminar ethylene non-premixed flame burning in air with a high soot loading. The second aim is to assess the efficacy of two alternative types of band-pass filters (broad- and

narrow-band) with bandwidths of 10 nm and 1.2 nm for interference suppression and for reducing the measurement error to the resulting temperature measurement. The third aim, which is the main aim of this paper, is to verify the efficacy of the narrow-band filters by comparing the resulting uncertainty in planar measurements of temperature with that obtained with conventional filters, both in an interference-free flame and a sooting flame with a peak soot volume fraction of ~1.2 ppm. The objective for the present work is to broaden the range of applicability of the NTLAF technique.

2. Experimental details

2.1. Burner and flames

A Santoro-type burner was used in this study [36,37]. The burner consists of two concentric brass tubes of 11 mm and 98 mm inner diameter. Gaseous fuel was injected through the central tube while air was passed through the annular co-flow passage. The central fuel tube extends 4 mm above the surface of the annular air co-flow tube. Both the central flow and annular co-flow were conditioned through a series of wire meshes and glass beads with a diameter of 4.8 mm at the bottom of the burner. Stainless steel honeycomb was encased as the final stage to straighten the flows. The vertically oriented burner was mounted on a translation device to allow vertical movements. The burner was positioned ~1.5 m beneath an exhaust hood. All measurements were performed at atmospheric pressure.

Both the spectral assessments of the sources of interference and the evaluation of the efficacy of narrow-band filters to suppress them were performed in a laminar non-premixed ethylene flame burning in air. The flow rate of ethylene through the central tube was kept at 0.175 standard liters per minute (L/min) and the flow rate of the co-flow air was 136.1 L/min, resulting in a flame length of 64 mm and a co-flow velocity of 0.3 m/s. This flame was chosen for its stable and well-defined structure, together with its high concentration of soot [38,39].

Verifications of planar NTLAF measurements in sooting flames were performed in a partially premixed ethylene/air sooting flame. The flow in the central tube was a mixture of ethylene (98.0% purity) (0.65 L/min) and air (1.28 L/min), resulting an equivalence ratio (Φ) of 7.2. This less sooting premixed flame was chosen over the non-premixed Santoro-type flame because it reduces out-of-plane fluorescence from atomic indium generated by secondary, scattered, excitation from soot up-beam in the flame that becomes notable at sufficiently high soot volume fractions. This additional issue is beyond the scope of the present paper. Noteworthy, the soot volume fraction under these operating conditions exceed most measured values in turbulent flames which is the main target of the planar NTLAF technique [40].

A soot-free premixed ethylene/air flame was employed to obtain the calibration constants for the NTLAF measurements and also to assess the fidelity of the narrow-band filters in the NTLAF measurements in non-sooting flames. The chosen flame relied on previous studies that showed that the calibration constants are insensitive to fuel composition and flame conditions [12,13]. In this non-sooting flame, the flow rate of the ethylene was 0.53 L/min, the blended air was kept at 3.91 L/min and the co-flow air stream was maintained at 136.1 L/min.

The independent measurements of flame temperature, required for calibration, were performed using an *R*-type Pt/Pt–Rh 13% thermocouple with a bead diameter of 75 μm (Omega, P13R-003). The measurement was performed in the central region of the flame where the temperature is uniform. A correction of 61 K was added to the raw measurement to correct for radiation heat loss from the thermocouple. Furthermore, temperatures measured in the present work were also compared with those calculated using the ChemKin software package, in which the model of OPPDIF and the GRI-Mech 3.0 mechanism were employed [41].

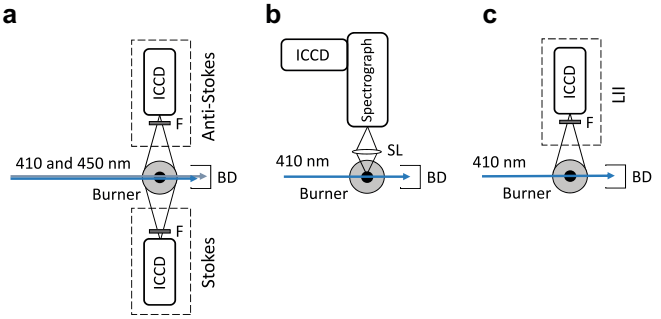

Fig. 1. Schematic diagrams of the experimental setup for (a) NTLAF measurements; (b) spectral assessment measurements and (c) LII measurements. SL, spherical lens; BD, laser beam dump; F, band-pass filter.

2.2. Indium seeding

The flames were seeded with indium nanoparticles produced using a laser ablation technique. The indium nanoparticles were produced using an in-house built device described previously [19,20,22]. A 10 Hz (8 ns pulse width) 532 nm beam from an Nd:YAG laser (Quantel, Brilliant B) was focused onto an indium rod. The ablation laser energy of ~0.1 J/pulse was chosen to yield sufficient LIF signal under the current flame conditions. The indium rod was rotated and translated in a sealed ablation chamber to provide a fresh surface for each ablation pulse. The ablation chamber was kept at approximately atmospheric pressure. The mass flow rate of the ablated particles seeded into the flame was estimated to be 160 μg/min, which corresponds to a gas-phase mole fraction in the fuel stream of approximately one part per million (assuming all indium ablation products convert to the gas phase). The seeded indium nanoparticles undergo thermal decomposition in the flame at positions close to the burner surface to yield neutral indium atoms. The thermal energy required to vaporize the entire mass flow rate of the indium ablation products in the flame was found to be negligible compared with the heat release from the flame.

2.3. Optical setup

Figure 1a presents the schematic diagram of the experimental setup for the NTLAF measurements. Two Nd:YAG pumped dye lasers are used to provide the excitation beams with wavelengths at 410.18 nm (the Stokes beam, $5^2P_{1/2} \rightarrow 6^2S_{1/2}$ transition) and 451.13 nm (the anti-Stokes beam, $5^2P_{3/2} \rightarrow 6^2S_{1/2}$ transition). The corresponding fluorescence signals are collected at approximately 450 nm (for the Stokes fluorescence, $6^2S_{1/2} \rightarrow 5^2S_{3/2}$ transition) and 410 nm (for the anti-Stokes fluorescence, $6^2S_{1/2} \rightarrow 5^2S_{1/2}$ transition), respectively [42]. Laser energy of 2.8 mJ/pulse and 1.6 mJ/pulse, were recorded for the Stokes and anti-Stokes beams, respectively, which are in the non-linear excitation regime. A temporal separation of ~100 ns between the two excitation lasers was adopted to avoid strong ELS from the alternate excitation lasers. The two laser beams are combined using a dichroic mirror (Thorlabs, DMLP425) and then passed through a telescope to expand into a collimated sheet of ~0.5 mm thickness. After the telescope, a small portion of the laser sheets was reflected by a thin glass window into a glass tank. The glass tank was located at the same distance from the telescope as the focusing point of the laser beam. The glass tank was filled with distilled water with suspended titanium oxides particles of diameter ~300 nm. The Mie scattering from titanium oxide nanoparticles was simultaneously recorded with a CCD camera (MegaPlus, ES 4020) and used for the reference laser power to derive temperature.

2.4. Detection systems

In the spectral assessment of interferences, a spectrometer (Andor Shamrock, SR-500i) combined with an intensified CCD (ICCD) camera (AndoriStar, DH734-18H-13) was used to record the laser-induced emissions from the laminar non-premixed ethylene sooting flame burning in air, as shown in Fig. 1b. The interference assessment was performed to the Stokes and the anti-Stokes processes. The radial profile of the flame was imaged onto the entrance slit using an $f = 250$ mm lens. The emissions were recorded without any optical filter. Both the prompt emission (relative to the start of the laser pulse) and that with a delay of 50 ns were recorded, with the aim to isolate the LII signals. The gate width of the camera was kept constant at 30 ns for all measurements, which is typical of previous NTLAF measurements. Spectra were accumulated from 100 instantaneous spectral images. Subtraction of dark charge was performed for each accumulated spectral image.

Two customized narrow band-pass filters (Alluxa) were employed for interference suppression, centered at 451.4 nm (FHMW = 1.32 nm) and 410.4 nm (FHMW = 1.08 nm). Both filters have a peak transmission of 95%, which provides an indium LIF signal collection efficiency nearly two times higher than that of the conventional 10 nm band-pass filters (Andover), whose peak transmissions are ~50%. The narrow-band filters are expected to increase the SIR around 7 – 9 times due to the narrower transmission band (10 nm/1.2 nm = 8.3). The doubled transmission also increases the ratio between LIF signals and the camera noise, which is particularly beneficial in instantaneous measurements. Moreover, the narrow band-pass filters have a specified high optical density (OD) of ~6.0 at the excitation laser wavelengths to further suppress laser ELS signals from the soot particles. This high OD is also necessary in NTLAF measurements because it had been found that a conventional filter with OD ~4.0 at laser wavelengths cannot suppress the ELS signals to an acceptable level in spectral assessments of interference source.

The effectiveness of the narrow band-pass filters in the enhancement of SIR in the laminar non-premixed ethylene sooting flame burning in air was assessed by recording separate sets of images, including total laser-induced emission (indium LIF and interferences), total interference and laser-induced emissions at 430 ± 5 nm. Each type of filter was used in front of one of the four-ICCD-camera bundle system (HFSC Pro, PCO), each with its independent control. The differences in collection efficiencies between the four cameras were corrected for. Spectral assessments with high spectral resolution around the indium LIF line at ~450 nm were also performed for the two sets of filter (broad- and narrow-band). Prompt signal from laser-induced emissions were recorded using the same setup in the aforementioned spectral assessment. These two assessments were only performed for the Stokes process, for which the transmission band of the filter (1.32 nm) is a little larger than that used for the anti-Stokes process (1.08 nm). Images were averaged from 400 instantaneous images.

The effectiveness of the narrow band-pass filters in measuring temperature was assessed both in non-sooting and sooting flames, using two oppositely positioned ICCD cameras to collect the Stokes and anti-Stokes signals (one camera in the HSFC Pro system and a PI-MAX II camera), which were each mounted with Nikon lenses (f/1.4). The narrow band-pass filters and the conventional band-pass filters (Andover, FWHM ~ 10 nm) were each mounted in front of the cameras, separately; then the measured temperatures were compared. The camera gate width was kept constant at 30 ns.

A potential drawback of using narrow-band filters in NTLAF measurements are they are limited to images with small angle of views (AOV) without applying any corrections. In this study, since a relatively large AOV has been used, a correction scheme has therefore been applied to the raw LIF images to correct for the variation in transmission efficiency at different angle of view of the filter. This is necessary because the blue-shift of the transmission for the band-pass filters that occurs at relatively large AOV for the narrow-band filters, while the 10 nm band-pass filter it is not affected by this issue because the blue-shift is significantly smaller than the bandwidth of the filter. In this study, the employed correction scheme firstly calculates the light transmission efficiency of the light source through the narrow-band filters and then applies the calculated planar correction image to the raw LIF images. It should be noted that based on the measured transmission curves of the narrow-band filters provided by the manufacturer and assuming an effective refractive index of the filter of 1.8, the maximum angle of incidence has been estimated to be 5.8° for the Stokes filter and 5.1° for the anti-Stokes filter, respectively. With a collection angle smaller than the maximum angle of incidence of the filters, uniform collection efficiency can be achieved in the field of view.

2.5. LII measurements

Soot volume fraction in the laminar sooting flames was measured with the LII technique. Figure 1c presents the schematic diagram of the experimental arrangement for the LII measurements. The flame was excited with an Nd:YAG pumped dye laser at 410.18 nm. The LII laser sheet has a height of 20 mm and a sheet thickness of 0.3 mm. The laser fluence of the excitation laser sheet was kept at ~0.2 J/cm^2 to ensure that the LII signal is independent of the excitation laser fluence variation [43]. The planar LII signal was collected using an ICCD camera fitter with a 430 ± 5 nm interference filter, with a time delay of 50 ns to temporally separate the LII signal from interferences from scattered laser light and fluorescence of species such as PAH [44]. The LII signal was calibrated by performing laser beam extinction measurements in the Santoro-type flame, with a continuous wave laser at 1064 nm for the extinction measurement. The extinction measurements were performed at various heights in the steady calibration flame to reduce the influence of primary particle evolution in the flame on calibration. The details of the experimental arrangement for the extinction measurement and the LII measurements can be found in our previous work [36].

3. Results and discussion

3.1. Interference sources

Figure 2a presents the prompt spectrographic image recorded for the Stokes processes. The excitation laser wavelength was 410.18 nm. The measurements were performed at a height above burner (HAB) = 22 mm in the Santoro-type sooting flame, where the peak soot volume fraction was measured by LII to be ~5.0 ppm. Laser scattering is strong and can even be found at ~425 nm from the two soot layers at the radial position of $r = \pm 3$ mm. The LIF signal from atomic indium appears at 451 nm in the spectra and is distributed from $r = 0$ mm (i.e., in the fuel-rich region) to $r = \pm 8$ mm (i.e., in the oxidation region). In the region $0 < r < 5$ mm, broadband interferences were found with varied intensity, which is attributed both to the fluorescence from PAHs and to the LII from soot particles [28,29,33]. To distinguish the two interferences in space, a time-delayed spectrographic image was also recorded 50 ns after the laser pulse, as shown in Fig. 2b. This captures only the interference generated by the LII emission because the lifetime of the LII emission is of the order of 100 ns while that of the fluorescence from PAH is only around 10 ns [28,45,46]. Consistent with this expectation, the time-delayed image is devoid of any emission in the central region of the flame.

Figure 2c and d present the emission spectrum of the flame after the Stokes laser excitation (i.e. the cross sections through the previous at $r = 0$ and 3 mm, respectively, for both Fig. 2a and b). These spectra were collected at two different radial locations at HAB = 22 mm, centered at $r = 0$ mm and $r = 3$ mm, each over a radial distance of ~0.38 mm. At $r = 0$ mm, the signal from the indium peak

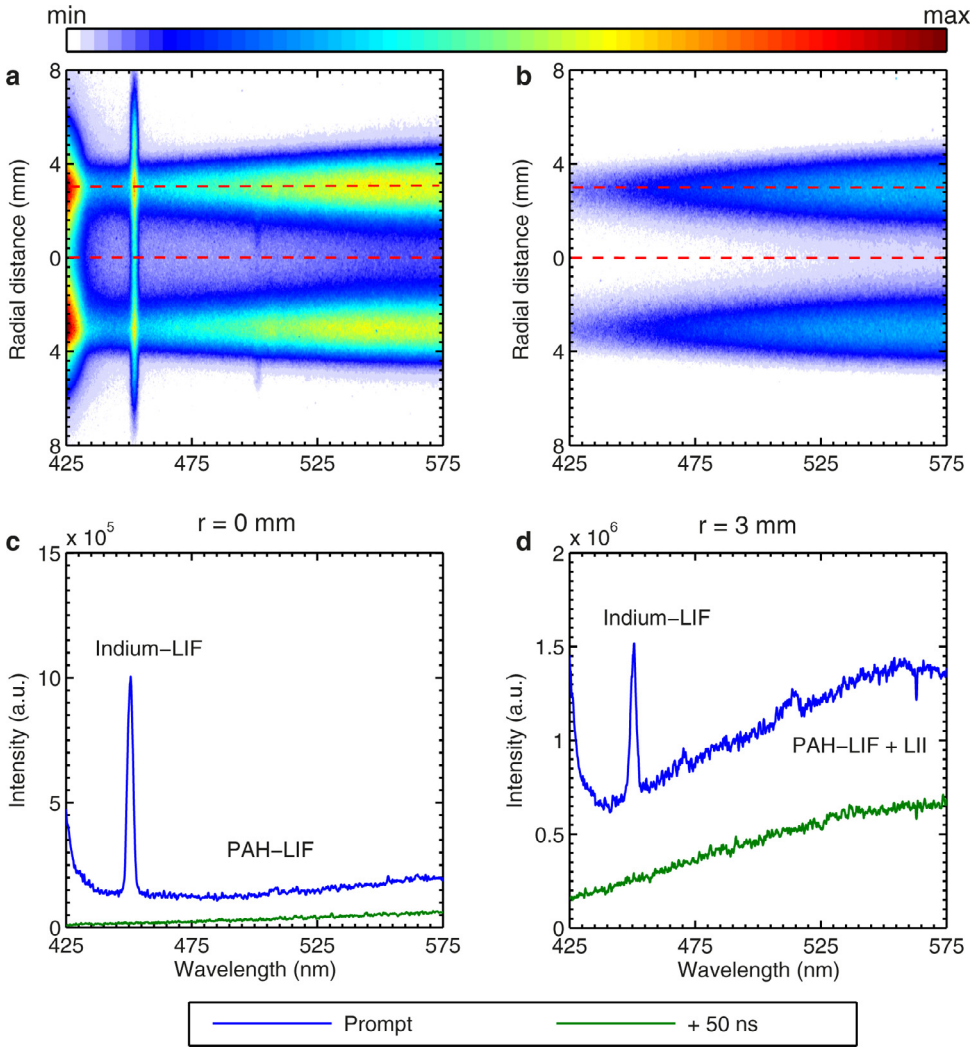

Fig. 2. Assembled spectrograph image for the Stokes process (excitation wavelength at 410 nm) as collected (a) with prompt timing and (b) with a 50 ns delay in a non-premixed ethylene laminar sooting flame burning in air. The cross-sections of prompt spectrograph image at radial distance of 0 mm (c) and 3 mm (d), as indicated by the dashed red lines in (a) and (b). HAB = 22 mm. (For interpretation of the references to colour in this figure legend, the reader is referred to the web version of this article.)

during prompt collection (Fig. 2c) is 7 times higher than the surrounding emission, while at $r = 3$ mm it is only about 2.2 times higher (Fig. 2d), for the current spectral resolution of ~1.8 nm and indium seeding load. This confirms that it is necessary to suppress/correct the interference when NTLAF is applied to sooting regions with soot volume fraction of a few ppm, which is typical for non-premixed sooting flames at atmospheric pressure. It can also be seen that in both Fig. 2c and 2d, the effect of delaying the time of collection has little influence on the shape of the emission (in the region either side of the indium peak), relative to the prompt case. The intensity is also lower from the delayed signal, as expected. This suggests that LII emission is the dominant contributor to the interferences within the wings of the flame where soot is significant (Fig. 2d), while PAH-LIF is dominant on the flame axis (Fig. 2c). This is consistent with knowledge that the PAH density is highest in the low-temperature, fuel-rich side of the reaction zone [47] while soot is dominant in the higher-temperature fuel-rich region. This finding that different types of interference are dominant in different regions of the reaction zone makes it problematic to use the method of intensity subtraction to correct for interferences especially in turbulent flames [25]. This is because different types of interference possess difference spectral characteristics, making intensity subtraction less reliable. Moreover, each intensity subtraction correction doubles the error associated with the imaging acquisition because two more images are required for the correction and therefore introduces additional uncertainty to the temperature measurements. It has been noted that a weak peak appears at ~516 nm in the prompt spectrum in Fig. 2d, which is deduced to arise from laser-induced sublimation of C_2 species [32].

Figure 3 presents the equivalent spectral assessment of interference to the anti-Stokes process, for which the laser wavelength was 451 nm. Spectrographic images presented in Fig. 3a and 3b are combined from two spectral assessments around 451 nm, which were recorded using the same grating as used in Fig. 2. The obvious difference is the presence of the dominant emission from Mie scattering (here at 451 nm) in Fig. 3, which is not visible in Fig. 2 (at 410 nm), due to the difference in the spectral range (150 nm for Fig. 2 and 360 nm for Fig. 3). In addition, the NTLAF signal is weaker relative to the background interference, consistent with the weaker signal from the anti-Stokes excitation than from the Stokes excitation. The anti-Stokes emission can be seen to comprise both LII and LIF of PAH components, which is consistent with the results shown in Fig. 2. However, the intensities of the peak relative to the shoulder is about 40% lower at $r = 0$ mm and is the same at $r = 3$ mm relative to the Stokes cases. This is because the flame temperature is lower in the central region compared with the soot region and therefore the ratio between anti-Stokes and Stokes signals (which is proportional to the flame

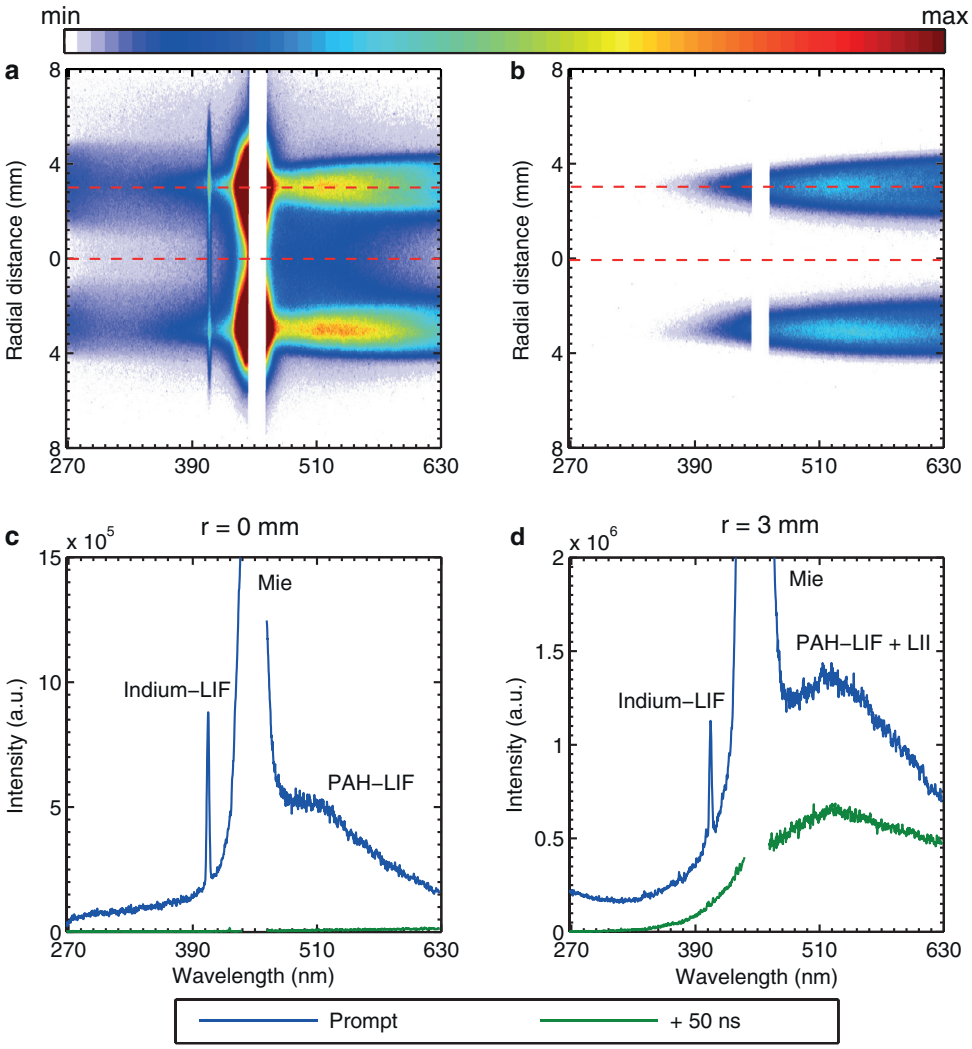

Fig. 3. Assembled spectrograph image for the anti-Stokes process (excitation wavelength at 450 nm) as collected (a) with prompt timing and (b) with a 50 ns delay in a non-premixed ethylene laminar sooting flame burning in air. The white vertical band around 450 nm in a and b represents the region of emission from Mie scattering. The cross sections of prompt spectrograph image at radial distance of 0 mm (c) and 3 mm (d), as indicated by the dashed red lines in (a) and (b). HAB = 22 mm. (For interpretation of the references to colour in this figure legend, the reader is referred to the web version of this article.)

temperature) is lower in the central region than in the soot region. As with the Stokes case, the LII emission dominates the interference source in the sooting layer, while the PAH-LIF dominates in the central region.

3.2. *Interference suppression using the narrow band-pass filter*

The efficacy of the narrow band-pass filter for signal collection was assessed by comparing the high resolution spectra from Stokes excitation in the Santoro-type sooting flame. The spectra were detected through the broad-band and narrow-band filters at a high spectral resolution of ~0.1 nm, together with the reference case without a filter (Fig. 4). The spectral measurements were performed at two different radial locations at HAB = 22 mm, at $r = 0$ mm (Fig. 4a) and $r = 3$ mm (Fig. 4b) in the Santoro-type sooting flame. It can be the peak to shoulder intensity ratio is about one and a half and two orders of magnitude higher at $r = 0$ mm and $r = 3$ mm when comparing results between narrow- and broad-band filters, respectively. Therefore, the narrow-band-pass filter suppresses interference much more effectively than the broad-band filter to achieve a peak to shoulder intensity ratio that is one and a half orders of magnitude higher both because of the narrower bandwidth (at ~1.32 nm) and the higher transmission (at ~95%) at 450 nm.

The efficacy of the narrow-band filter was then tested by performing planar measurements at different heights within the laminar non-premixed ethylene flame burning in air. The excitation wavelength was tuned to be the resonant absorption line of indium at 410.18 nm and the emissions were collected with the HSPC pro camera system. Figures 5a and 4b present pure interference emissions, including both LIF of PAH and LII, as recorded with the broad- and narrow- band filters, respectively, at ~451 nm. The flame was without any indium seeding. It can be seen that the narrow-band filter suppresses the interference emissions more effectively than the broad-band filter by a factor of ~4 at all locations in the flame. To isolate the spatial locations of LII emission, one case was recorded with the camera time-delayed by 50 ns using the filter at 430 ± 5 nm, as shown in Fig. 5c. This shows that the interference from LIF of PAH occurs mostly in the lower, central region of the flame and that interference from LII occurs mostly in the outer and downstream regions of the flame, consistent with understanding about their relative spatial locations and the findings from Figs. 2 and 3.

Figure 5d to 5f present prompt laser-induced emissions including both interference and indium LIF signal collected with broad- and narrow-band filters and at 430 ± 5 nm, where indium is seeded into the flame. The asymmetry of the indium LIF signal shown in Fig. 5d

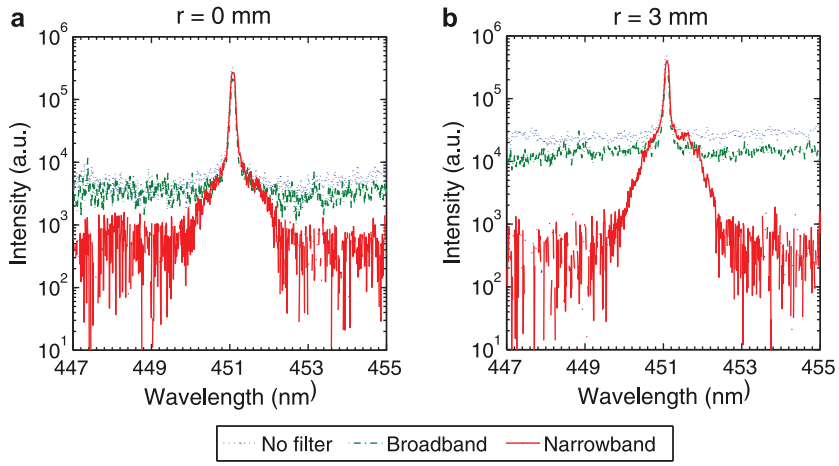

Fig. 4. Emission recorded with high spectral resolution around the indium LIF line at a single point (HAB = 22 mm) at (a) $r = 0$ mm and (b) $r = 3$ mm, as collected through no filter, a broadband filter (FWHM = 10 nm) and a narrowband filter (FWHM = 1.32 nm). Signals were promptly recorded with a gate width of 30 ns and for the Stokes process.

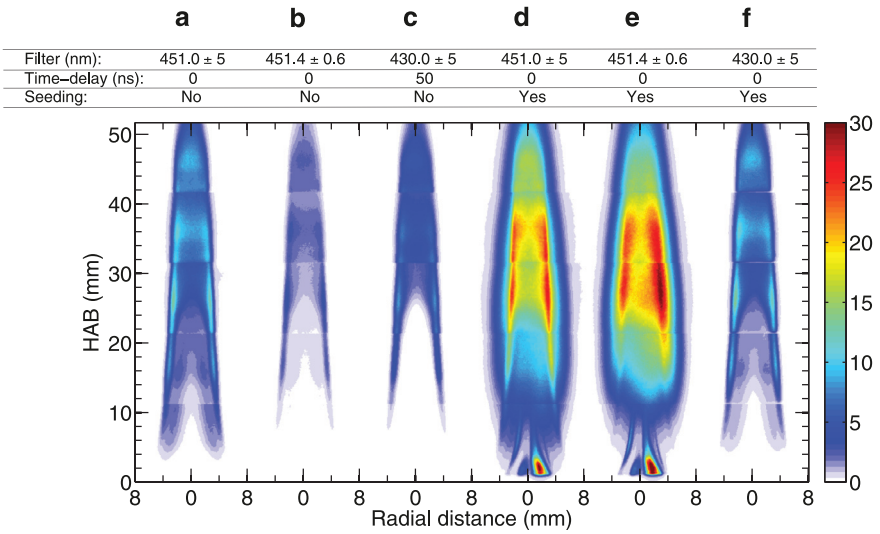

Fig. 5. Laser-induced emissions as collected with the different combinations of band-pass filters, delay times and seeding shown in the key. These image collages are assembled from the average of 400 instantaneous measurements at multiple heights. The gate width was kept constant at 30 ns and the excitation was at 410.18 nm for all cases.

and 5e is due to asymmetry in the seeding distribution in the flame rather than to laser attenuation, because the propagation direction of the laser beam was from left to right. This was also checked by rotating the burner. Significant differences between signals collected through the broad- and narrow-band filters are evident. Firstly, the signal intensity is typically higher everywhere for the narrow-band filter (Fig. 5e) than for the broad-band filter (Fig. 5d), consistent with the higher transmission noted previously. Secondly, the structure is more pronounced with the broad-band filter (Fig. 5d) than for the narrow-band filter (Fig. 5e), i.e. the intensity is more uniform in the latter image. This is because the interference from the LII, which has a distinct two-layer structure at the outer edge of the flame for most of flame heights (Fig. 5c) caused by the presence of soot, penetrates more strongly through the broad-band filter than the narrow-band filter to augment the structure in the final image. This provides further evidence of the efficacy of the narrow-band filter in suppressing interference, especially in regions where interference from LII in the maximum range typically encountered in laboratory flames, where it is measured to be ~10 ppm [37,48,49].

Figure 6 presents the radial profiles obtained from the data corresponding to the cases shown in Fig. 5d and 5e, for the four axial locations HAB = 17, 27, 37 and 47 mm. These figures present the total emission for each of the two filters, the total interference emissions from Fig. 5a and 5b and the resulting corrected NTLAF signal, which is derived by subtracting the interference emission from the total emission (Figs. 5d and 5e). This quantifies the extent to which the narrow-band filter increases the SIR relative to the broad-band filter, which varies throughout the flame. Indeed at some locations, notably on the centerline at HAB = 47 mm (Fig. 6a), the interference is greater than the signal for the broad-band filter, but much less for the narrow-band filter. Indeed, the SIR is found from these profiles to increase by an average factor of about ~6.

Figure 7a presents the radial distributions at HAB = 27 mm of the same emissions shown in Fig. 6, together with the corresponding SIR (Fig. 7b) and the corresponding soot volume fraction (Fig. 7c). The radial distributions of total interference and indium LIF signal (Stokes) shown in Fig. 7a for both broad- and narrow-band filters, are the same as those in Fig. 6c. Fig. 7b depicts the corresponding profiles of SIR and the ratio between SIR of narrow- and broadband filters. This shows that, at the outer edges of the flame ($r > 6.5$ mm), the SIR for the broad-band filter is less than 3, while it is 20 for the narrow-band filter, even though the magnitude of the indium LIF signal is low there. Significantly, the SIR for the narrow-band filter in this region is similar to the best SIR obtained with the broad-band filter. Importantly too, the radial location at $r = 8$ mm is well outside the edge of the flame, so that the high SIR is maintained beyond $r = 6$ mm for

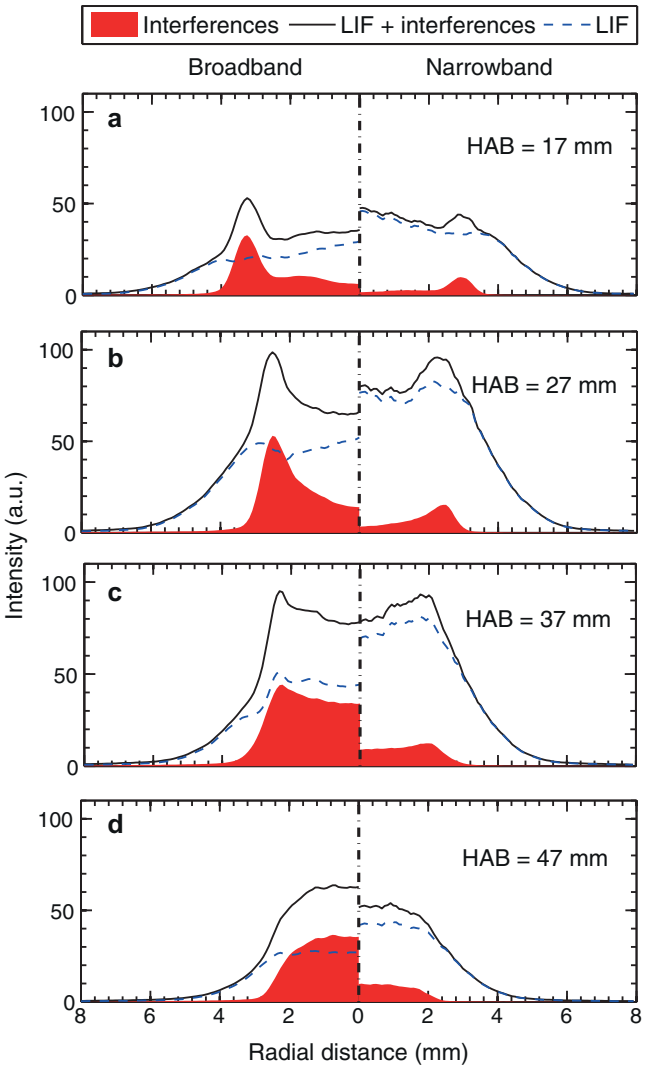

Fig. 6. Radial profiles of the total laser-induced emission from the Stokes process, the total interference emission (from LIF of PAH and LII) and the deduced pure indium LIF signal (derived from subtraction of the interferences from the total), as collected through the narrowband and broadband filters, at (a) HAB = 17 mm, (b) HAB = 27 mm, (c) HAB = 37 mm and (d) HAB = 47 mm.

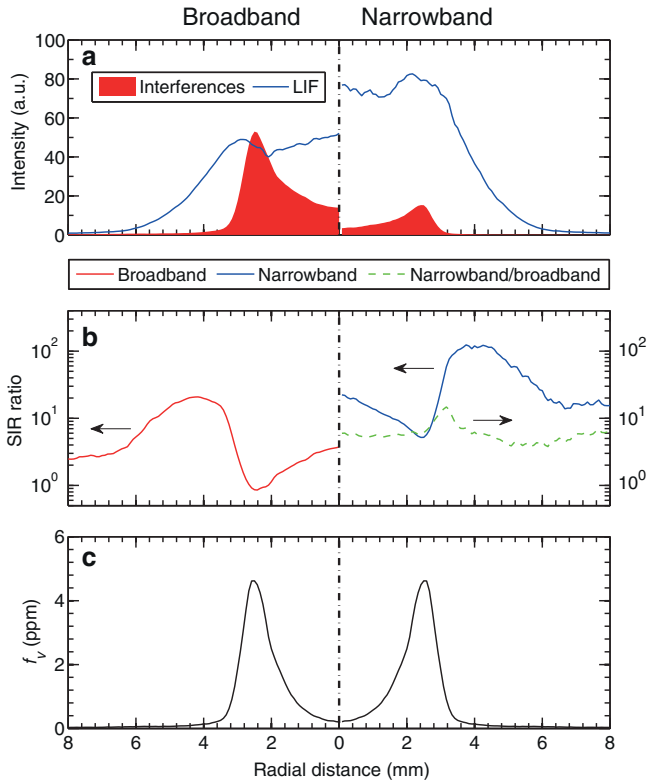

Fig. 7. (a) Radial profiles at HAB = 27 mm of the total interferences emission (including LIF of PAH and LII) and of the deduced total NTLAF signal (derived from subtracting the interference from the total emission), (b) signal-interference-ratio (SIR) and the ratio of SIR between broadband and narrowband filters (green dash line) (c) soot volume fraction.

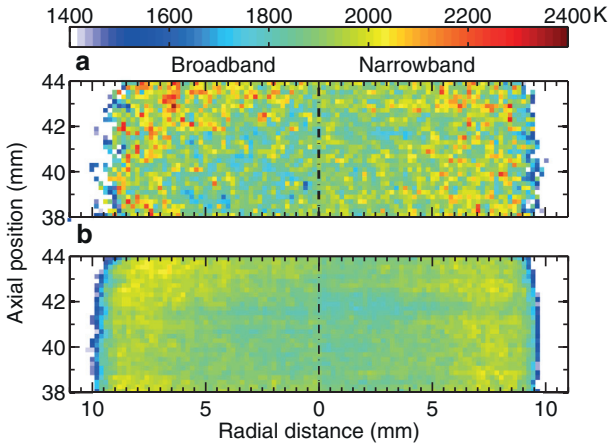

Fig. 8. Temperature maps in an interference-free premixed ethylene/air flame, acquired using broad- and narrow-band filters of (a) an instantaneous temperature measurement, and (b) an averaged temperature profile from 50 instantaneous temperature measurements.

the narrow-band filter, in contrast to the broad-band filter, where the SIR is ~2. This is a very significant finding, because it shows that the narrow-band filter extends the range for which measurements can be obtained into the oxidizing side of the reaction zone, which was deduced not to be possible previously because indium is known to be oxidized through the reaction zone and its low concentration on the fuel-lean side [13,14,22]. The SIR can be seen to increase further as r is moving toward the reaction zone. The magnitude of SIR peaks at $r \sim 5$ mm, with values of ~110 (with narrow-band filter) and of ~20 (with broad-band filter), at a location where the signal is high and the soot volume fraction is relatively low (Fig. 7c), so that the interference from LII is also low. This zone of high SIR extends throughout the region of $3 < r < 5$ mm. The lowest value of SIR is located at $r \sim 2.8$ mm, which corresponds to the position of maximum soot loading as shown in Fig. 7c. This provides further evidence that the dominant source of interference is LII from soot. In the central zone of the flame, $r < 1.5$ mm, the SIR increases to values of a low SIR ratio of ~3 (broad-band) and ~15 (narrow-band). This confirms that the interference from PAH-LIF is less significant than that from LII in this region.

3.3. Temperature measurements in the non-sooting flame

Figure 8 presents the planar temperature measurements of flame temperature in the non-sooting flame for the two sets of band-pass filters. A typical instantaneous image is shown in Fig. 8a, while the averaged temperature around HAB = 41 mm is shown in Fig. 8b, each for half of the flame. The averaged temperature image was derived from 50 instantaneous temperature images. Interference is negligible in this non-sooting flame, so that the noise is attributable to the ICCD cameras. It can be seen that the instantaneous and the

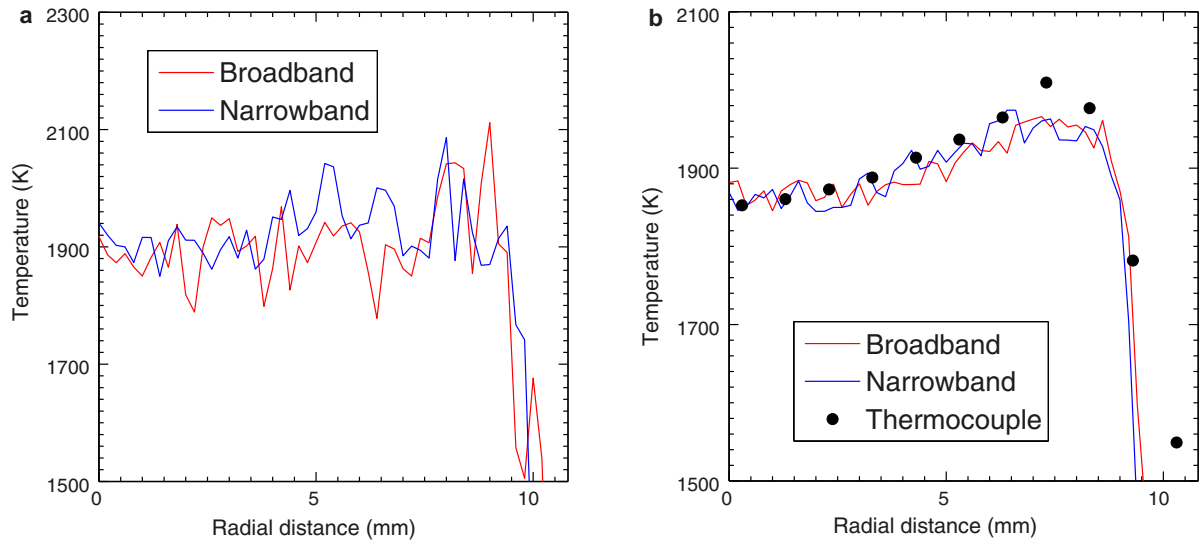

Fig. 9. Radial temperature profiles at HAB = 41 mm in a soot-free premixed ethylene/air flame (Fig. 7) as acquired using broad- and narrow-band filters of (a) instantaneous NTLAF radial temperature profiles, and (b) NTLAF radial temperature profiles averaged from 50 instantaneous temperature measurements and thermocouple temperature measurements. The adiabatic temperature calculated using ChemKin is 2100 K.

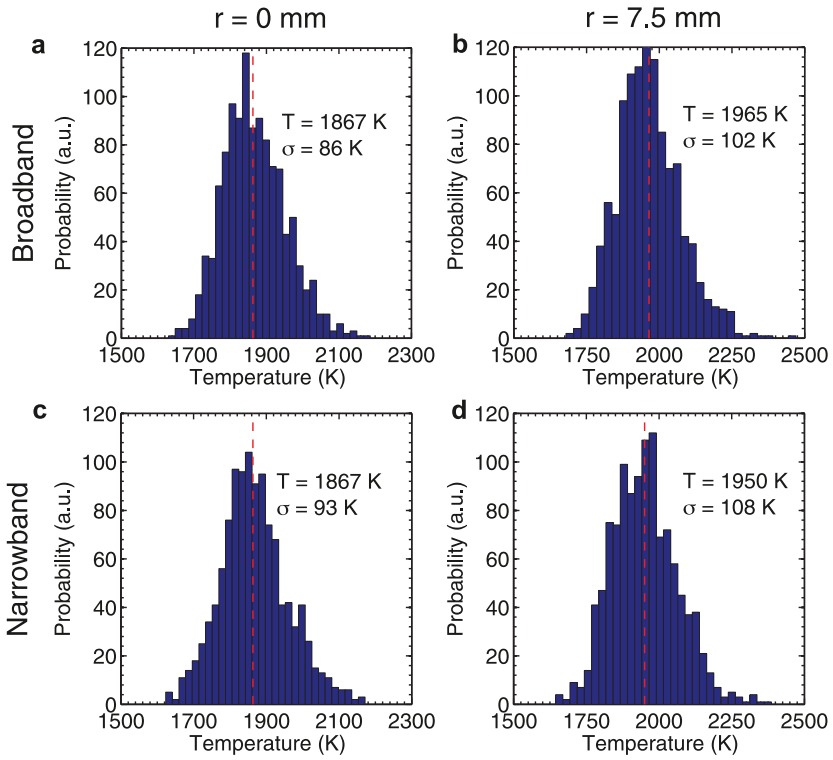

Fig. 10. The temperature histograms from 1000 instantaneous shots using (a, b) broad- and (c, d) narrow-band filters. The red dashed line indicates the mean temperature. Data are extracted from an area of 0.25 × 0.25 mm^2 at HAB of ~ 41 mm on the axis (a, c) and at r = 7.5 mm (b, d). (For interpretation of the references to colour in this figure legend, the reader is referred to the web version of this article.)

averaged images obtained with the two sets of filter are generally in good agreement in non-sooting flames. Notably, the maximum flame temperature is ~134 K lower than the adiabatic temperature of 2100 K calculated with the ChemKin.

Figure 9 presents radial profiles for the instantaneous and averaged temperature images, shown in Fig. 8, integrated at axial location HAB = 41 ± 0.5 mm. As noted earlier, for all radial locations, the two temperature measurements using the two sets of filter agree to within 30 K, although the scatter in the instantaneous data for narrow-band filter (Fig. 9a) is about ± 80 K, which is close to half that with the broad-band filter. Comparison between NTLAF and thermocouple temperature measurements reveals good agreement in the region r < 6.5 mm. However, discrepancy starts to appear toward the reaction zone and reaches ~50 K at r = 7 mm. At the outer radial locations r > 7 mm, the NTLAF results and thermocouple temperature measurements agree within 30 K. This indicates the NTLAF technique

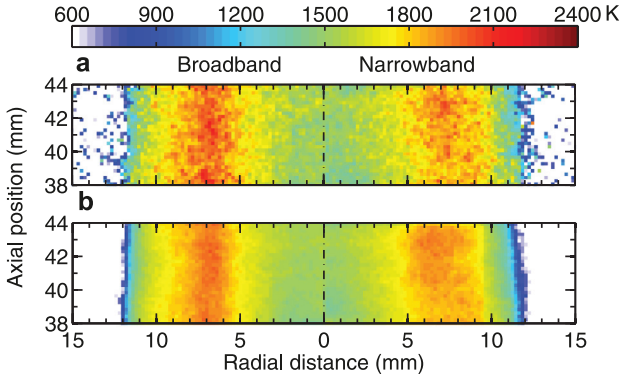

Fig. 11. Temperature maps in a partially premixed ethylene/air sooting flame as acquired using the broad- and narrow-band filters of (a) an instantaneous temperature measurement, and (b) an averaged temperature profile from 50 instantaneous temperature measurements.

in soot-free flames can reliably be applied for temperature measurements, with the use of both broad- and narrow-band filters.

Figure 10 presents histograms of temperatures around HAB = 41 mm and at $r = 0$ mm and $r = 7.5$ mm, shown in Fig. 8a. Data presented are acquired from 250 instantaneous temperature measurements using the two sets of band pass filters. The data were then extracted from four neighboring regions in which temperature is homogeneous, each of 0.25 × 0.25 mm^2 to provide a statistical interpretation based on 1000 instantaneous measurements. It can be seen that both measured data sets yield a mean temperature of 1876 K, with standard deviations of 86 K and 93 K, for the broad- and narrow-band filters, respectively. At $r = 7.5$ mm, the measured mean temperatures are 1965 K and 1950 K, with standard deviations of 102 K and 108 K, respectively. The consistency in the measurement precision in this interference-free flame leads to the conclusion that the customized narrow band filter is reliable.

3.4. Temperature measurements in the sooting flame

Figure 11 presents the temperature images from the partially premixed ethylene/air sooting flame. The averaged temperature images, as shown in Fig. 11b, were averaged from 50 instantaneous temperature images. Significant difference appears in the region of 5 mm $< r <$ 9 mm, i.e., the soot layer zone, while in the central zone, the temperature measured using the 10 nm filters is slightly higher than that measured using the narrow band filter.

To assess the reason for the difference between the measured temperatures, the emissions for non-resonant laser excitations were also collected. Figures 12a and 11c present radial profiles of laser induced emissions with on- and off-resonant excitations at HAB = 41 mm for the Stokes and the anti-Stokes processes, respectively. All signals are averaged over 50 single-shot measurements. Significant interference is observed in the signals collected using the broadband filters. In contrast, the interference is relatively weak and even negligible when the narrow band filters were used. Figure 12b and 12d present the SIR for the Stokes and anti-Stokes processes, derived from Fig. 12a and 12c. In both processes, the SIR has been increased by a factor of 7–9 times across the radial profile of the flame

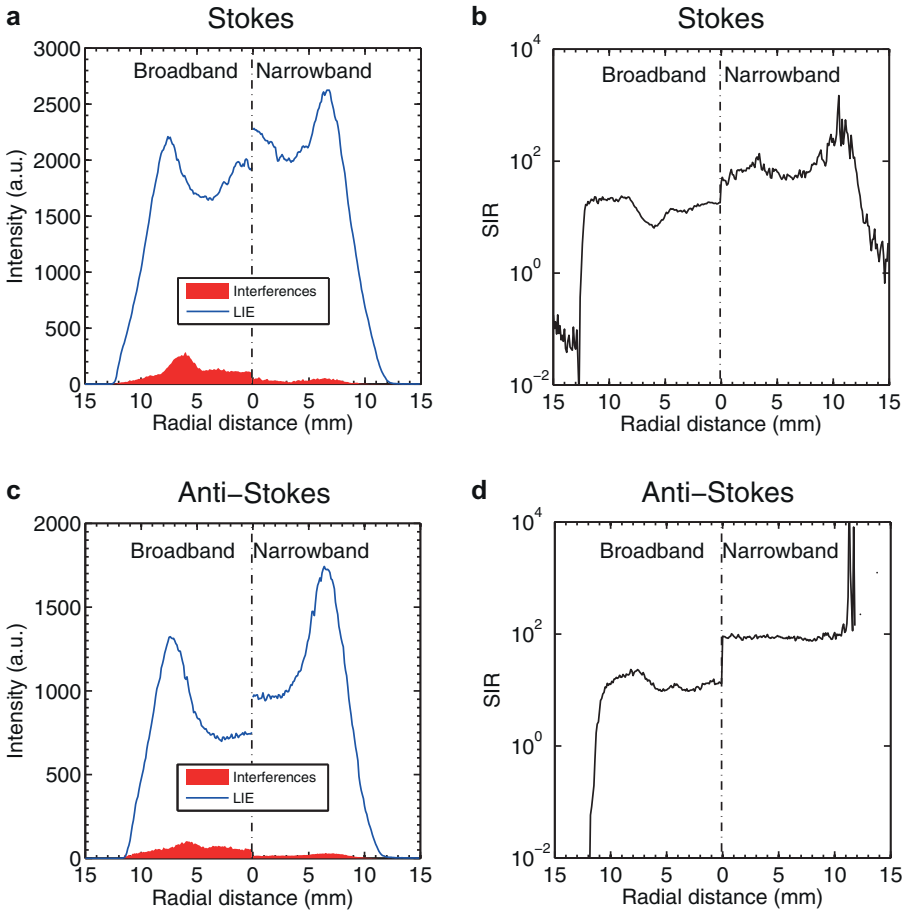

Fig. 12. Radial profiles of the partially-premixed ethylene/air flame at HAB = 41 mm of total interference emissions (including LIF of PAH and LII) acquired through off-resonant excitations, laser-induced emissions (signal plus interferences) acquired through on-resonant excitations and signal to interference ratio, acquired using broad- and narrow-band filter. (a, b) are Stokes processes and (c, d) are anti-Stokes processes.

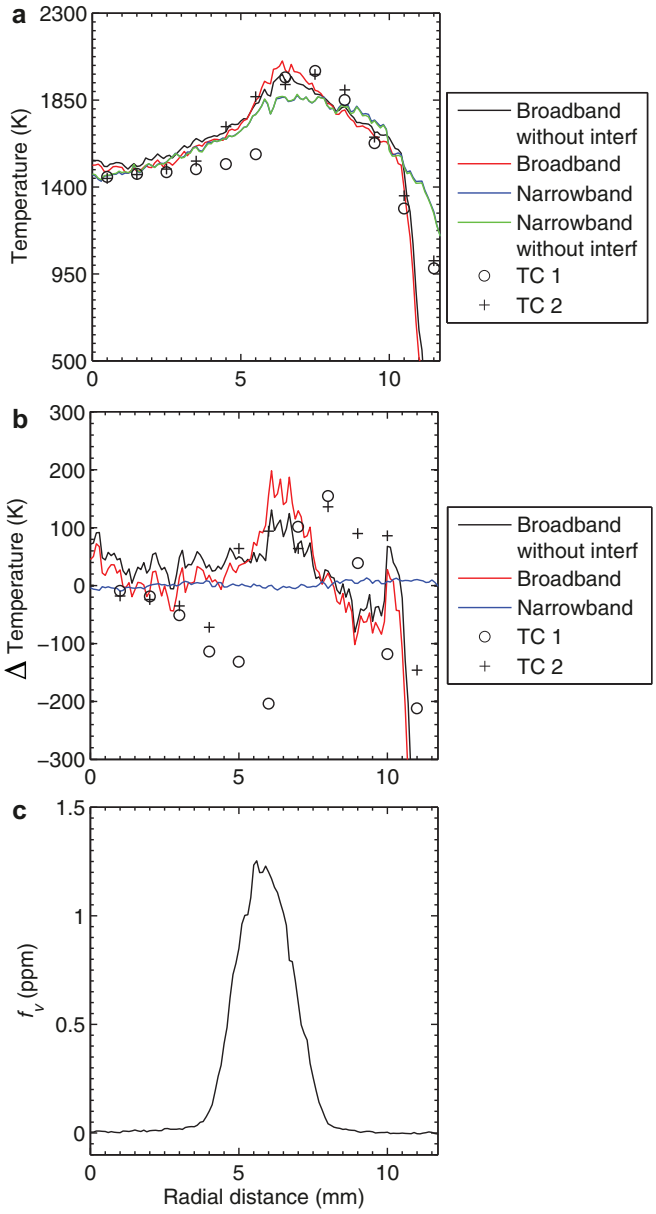

Fig. 13. (a) Radial temperature profiles acquired using broad- and narrow-band filters and thermocouple, respectively. Thermocouple measurements were performed by traversing the bead through the flame in two directions (TC 1 and TC 2). NTLAF temperature profiles displayed are calculated from both including the interference emissions and with the correction for interference emissions. (b) Difference in radial temperature profile when compared with temperature acquired using narrow-band filters with interference correction. (c) Radial profile of soot volume fraction.

when narrow-band filters are used for signal collection, which is consistent with a theoretical estimation.

Figure 13a presents radial profiles of the averaged temperatures calculated based on signals shown in Fig. 12a and 12c. The temperature profiles were calculated with and without interference subtractions. Figure 13a shows clear differences between the two sets of measured temperature using different band pass filters. The radial temperature profile derived from using narrow-band filters with interference correction was used as a reference and the difference between this profile and other temperature profiles were plotted, as shown in Fig. 13b. At radial positions, 0 mm $< r <$ 2 mm and 5.5 mm $< r <$ 7 mm, the measured temperatures using the narrow-band filter are about ~30 K and 150 K lower than those measured using the broad-band filters, and at 7 mm $< r <$ 10 mm, temperature measured by the narrow-band filters are 50 K higher than those measured using the broad-band filters, even though they show the same trend as a function of radial distance r. The maximum differences of temperature between two sets of measurement is ~160 K at $r = 6.5$ mm, which is the oxidation shoulder of the soot layer, as shown in Fig. 13c. It should be noted that, even though the measured temperatures are consistent with each other within 200 K, this consistency is based on the fact that large uncertainties exist in the results measured using the broadband filters due to residual interferences. Notably, the maximum flame temperatures of 1880 K (narrow-band) and 2080 K (broad-band) are ~352 K and 272 K below the adiabatic temperature of 2232 K, respectively, as predicted from the calculation using the ChemKin software package. The difference is due to that the radiative heat transfer from the soot and the enthalpy contained in the soot particles are not included in the model.

Figure 13 also present results from thermocouple temperature measurements. The two results converge for 0 mm $< r <$ 3 mm and 8 mm $< r <$ 9 mm, as shown in Fig. 13a. However, the thermocouple measurement can be biased due to the deposition of soot particles on the bead. To examine the effect of soot deposition on the thermocouple, the measurements were performed by traversing the bead through the flame in two reversed directions, as represented by crosses and hollow black circles in Fig. 13a. The results presented in Fig. 13a shows that discrepancies between the two direction measurements occur at the soot layer locations (4 mm $< r <$ 7 mm) and a maximum difference of ~300 K occurs at $r \sim 5.5$ mm. The NTLAF results agree well with the thermocouple measurements in the regions of $r <$ 3 mm. However, results from NTLAF and thermocouple across the soot layer differ dramatically, reaching a maximum of ~200 K at $r = 5.5$ mm. This implies that thermocouples are not reliable for thermometry in the sooting flames.

Figure 13b presents the differences in measured radial temperature between the results acquired using broad- and narrow-band filter, thermocouple and results from narrow-band filters with interferences subtractions (shown in Fig. 13a). While the uncertainties in the measurements with narrow-band filters are constantly low and vary within 10 K along the radial direction, for measurements using the broad-band filters these values vary from 90 K in the central region to 198 K in the high soot loading region of 5 mm $< r <$ 7 mm. Notably, at the peak soot loading position, $r = 5.5$ mm, the uncertainty of the interference-corrected broad-band measurement is 131 K, about 67 K lower than the results acquired from broad-band filter without interference correction. The discrepancy between the thermocouple measurements and the narrow-band filter without interference results also follow the same trend. The difference is small for $r <$ 3 mm and reaches a maximum of ~200 K at $r = 6$ mm. It should be noted that the uncertainty in temperature measurement due to the presence of interference scales with the uncertainty in the ratio of the two LIF signals and it is lower than summing the uncertainty of each individual processes. This is because the sources of interference are identical for both the Stokes and anti-Stokes signals, so that they are correlated, and because interference can only cause an increase in the measured signal to the actual indium LIF signals.

Figure 14 presents histograms of temperatures over an area of 0.25 × 0.25 mm^2 at a flame position of HAB of 41 mm, at $r = 0$ mm, 5.5 mm and 6.5 mm, in the partially premixed ethylene/air sooting flame (Fig. 11). Data presented are averaged from 300 instantaneous measurements using the two sets of band pass filters, respectively. The mean values of the measured temperatures, as well as the significant difference between the two sets of measurements, are consistent with those shown in Fig. 13. Besides this, the statistics of the measured temperature results are different, in particular for the results measured in the central zone as shown in Figs. 14a and 14d. At $r = 0$ mm, where interfering signals are mainly from LIF of PAH (see Fig. 12a and 12c), the standard deviation of the results from measurements with broadband filters (Fig. 14a) is 178 K, which is much larger

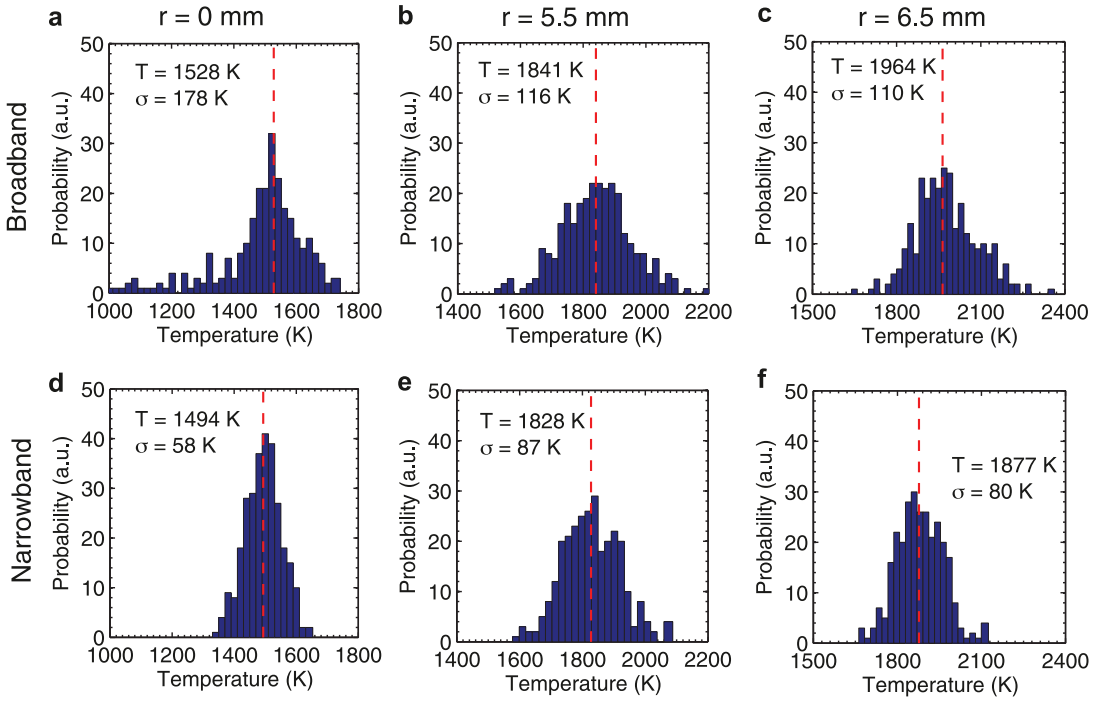

Fig. 14. Temperature histograms from 300 instantaneous shots using: (a, b, c) broad- and (d, e, f) narrow-band filters at $r = 0$ mm (a, d), $r = 5.5$ mm (b, e) and $r = 6.5$ mm (c, f), respectively. The red dashed line indicates the mean temperature. Data are extracted from an area of 0.25×0.25 mm^2 at HAB = 41 mm of an ethylene/air flames with $\Phi = 7.2$. (For interpretation of the references to colour in this figure legend, the reader is referred to the web version of this article.)

than that measured with the narrow-band pass filters, i.e., 58 K, as shown in Fig. 14b. At $r = 5.5$ mm, i.e., in the region of the soot layer, the standard deviations are 116 K and 87 K, respectively. Similar trend can also be found at $r = 6.5$ mm, the standard deviation are 110 K and 80 K for broad- and narrow-band filters where the differences of temperature between two sets of measurement is maximum of 87 K. These results also indicate that by using of high transmission filters in the NTLAF measurements, higher precision, corresponding to a reduction in the standard deviations of measured temperature of 67%, 25% and 27% (average reduction is ~40%) at $r = 0$ mm, and 5.5 mm and 6.5 mm, respectively, can be obtained.

Figure 14 shows that the temperature span, measured using both the band-pass filters, differs at each radial location and is narrower for the narrow-band filter especially at the region of high interference. For the centerline ($r = 0$ mm) the temperature spans the range 1000–1720 K when using the broad-band filter while this range is reduced to between 1360 K and 1640 K when a narrow-band filter is used. Similarly, at $r = 5.5$ mm, where the soot volume fraction peaks, the temperature distribution using narrow-band filters ranges from 1610 K to 2070 K, while the temperature distribution spans from 1540 K to 2130 K using the broad-band filters. The same trend holds for $r = 6.5$ mm, where the measured temperature spans from 1650 K to 2350 K for broad-band filters and from 1670 K to 2110 K for the narrow-band filters. The corresponding differences in the mean temperatures acquired using broad- and narrow-band filters are found to be 34 K ($r = 0$ mm), 13 K ($r = 5.5$ mm) and 87 K ($r = 6.5$ mm). This indicates that when broad-band filters are used in sooting flames, an overestimation of the temperature is likely.

4. Conclusions

Three types of interferences on the NTLAF fluorescence have been identified when this thermometry technique is applied to sooting flames. The identified interferences are: laser-induced fluorescence by PAH species, laser Mie scattering and laser-induced incandescence from soot particles. The LIF of PAH and LII interferences are both broadband, and spatially, spectrally and temporally overlapped with the fluorescence signals for both the Stokes and anti-Stokes processes. It has been found that conventional band-pass filters (FWHM = 10 nm) cannot efficiently suppress these interferences in highly sooting flames to provide high fidelity temperature measurements. Therefore, a set of custom-made narrow-band filters (FWHM = 1.2 nm) has been developed and experimentally verified for interference suppression. The experimental results show that the signal to interference ratio can be enhanced by a factor of ~6 by using the narrow band filters, resulting in reduced temperature measurement uncertainty and enabling reliable planar temperature measurements in sooting flames.

Good agreements have been found between the evaluated temperatures using the two kinds of filters in a non-sooting flame. In the moderately sooting flame, both the accuracy and the precision of the measurements have been improved by using the new narrow-band filter to suppress the interference and to increase the indium LIF signal collection. At the peak soot volume fraction location with a value of 1.2 ppm, the measurement accuracy due to the presence of interferences has been increased from 198 K to 10 K with using the narrow-band filters. A maximum temperature overestimation of ~160 K was found at a location slightly outside of peak soot volume fraction in the soot layer when comparing the results derived from the two sets of filters. An average reduction of 40% in the standard deviation of measured temperature in single-shot measurements can be obtained by use of high transmission filters. This significantly reduces the inter-pixel and inter-shot uncertainty and therefore increases measurement precision. Moreover, with the combined use of narrow-band filters and shorter camera gate-width the measurement uncertainty of NTLAF in sooting flames is expected to be further reduced.

Acknowledgments

The support of the Centre for Energy Technology (CET) and The University of Adelaide is gratefully acknowledged. The support of the

Australian Research Council (ARC) is also gratefully acknowledged for funding this work through its Discovery and LIEF schemes. Mr Peter Egerton from Alluxa is greatly acknowledged for help in supplying the narrow-band filters used in the present study.

References

[1] D. Hofmann, A. Leipert, Temperature field measurements in a sooting flame by filtered Rayleigh scattering (FRS), Symp. (Int.) Combust. 26 (1996) 945–950.
[2] S.P. Kearney, R.W. Schefer, S.J. Beresh, T.W. Grasser, Temperature imaging in non-premixed flames by joint filtered Rayleigh and Raman scattering, Appl. Opt. 44 (2005) 1548–1558.
[3] E. Kristensson, A. Ehn, J. Bood, M. Aldén, Advancements in Rayleigh scattering thermometry by means of structured illumination, Proc. Combust. Inst. 35 (2015) 3689–3696.
[4] D. Most, A. Leipertz, Simultaneous two-dimensional flow velocity and gas temperature measurements by use of a combined particle image velocimetry and filtered Rayleigh scattering technique, Appl. Opt. 40 (2001) 5379–5387.
[5] F.-Q. Zhao, H. Hiroyasu, The applications of laser Rayleigh scattering to combustion diagnostics, Prog. Energy Combust. Sci. 19 (1993) 447–485.
[6] A. Bohlin, C.J. Kliewer, Diagnostic imaging in flames with instantaneous planar coherent Raman spectroscopy, J. Phys. Chem. Lett. 5 (2014) 1243–1248.
[7] Z. Yin, I. Adamovich, W. Lempert, OH radical and temperature measurements during ignition of H 2-air mixtures excited by a repetitively pulsed nanosecond discharge, Proc. Combust. Inst. 34 (2013) 3249–3258.
[8] Q.N. Chan, P.R. Medwell, P.A. Kalt, Z.T. Alwahabi, B.B. Dally, G.J. Nathan, Simultaneous imaging of temperature and soot volume fraction, Proc. Combust. Inst. 33 (2011) 791–798.
[9] J. Engström, J. Nygren, M. Aldén, C. Kaminski, Two-line atomic fluorescence as a temperature probe for highly sooting flames, Opt. Lett. 25 (2000) 1469–1471.
[10] C. Kaminski, J. Engström, M. Aldén, Quasi-instantaneous two-dimensional temperature measurements in a spark ignition engine using 2-line atomic fluorescence, Symp. (Int.) Combust. 27 (1998) 85–93.
[11] P.R. Medwell, Q.N. Chan, B.B. Dally, S.M. Mahmoud, Z.T. Alwahabi, G.J. Nathan, Temperature measurements in turbulent non-premixed flames by two-line atomic fluorescence, Proc. Combust. Inst. 34 (2013) 3619–3627.
[12] P.R. Medwell, Q.N. Chan, P.A. Kalt, Z.T. Alwahabi, B.B. Dally, G.J. Nathan, Development of temperature imaging using two-line atomic fluorescence, Appl. Opt. 48 (2009) 1237–1248.
[13] P.R. Medwell, Q.N. Chan, P.A. Kalt, Z.T. Alwahabi, B.B. Dally, G.J. Nathan, Instantaneous temperature imaging of diffusion flames using two-line atomic fluorescence, Appl. Spectrosc. 64 (2010) 173–176.
[14] J. Nygren, J. Engström, J. Walewski, C. Kaminski, M. Aldén, Applications and evaluation of two-line atomic LIF thermometry in sooting combustion environments, Meas. Sci. Technol. 12 (2001) 1294.
[15] I.S. Burns, X. Mercier, M. Wartel, R.S. Chrystie, J. Hult, C.F. Kaminski, A method for performing high accuracy temperature measurements in low-pressure sooting flames using two-line atomic fluorescence, Proc. Combust. Inst. 33 (2011) 799–806.
[16] O.M. Feroughi, S. Hardt, I. Wlokas, T. Hülser, H. Wiggers, T. Dreier, C. Schulz, Laser-based in situ measurement and simulation of gas-phase temperature and iron atom concentration in a pilot-plant nanoparticle synthesis reactor, Proc. Combust. Inst. 35 (2015) 2299–2306.
[17] H. Kronemayer, P. Ifeacho, C. Hecht, T. Dreier, H. Wiggers, C. Schulz, Gas-temperature imaging in a low-pressure flame reactor for nano-particle synthesis with multi-line NO-LIF thermometry, Appl. Phys. B 88 (2007) 373–377.
[18] A.C. Eckbreth, Laser diagnostics for combustion temperature and species, CRC Press, 1996.
[19] Q.N. Chan, P.R. Medwell, B.B. Dally, Z.T. Alwahabi, G.J. Nathan, New seeding methodology for gas concentration measurements, Appl. Spectrosc. 66 (2012) 803–809.
[20] D.H. Gu, Z.W. Sun, P.R. Medwell, Z.T. Alwahabi, B.B. Dally, G.J. Nathan, Mechanism for laser-induced fluorescence signal generation in a nanoparticle-seeded flow for planar flame thermometry, Appl. Phys. B 118 (2015) 209–218.
[21] A. Manteghi, Y. Shoshin, N. Dam, L. de Goey, Two-line atomic fluorescence thermometry in the saturation regime, Appl. Phys. B 118 (2014) 1–13.
[22] P.R. Medwell, Q.N. Chan, B.B. Dally, Z.T. Alwahabi, S. Mahmoud, G.F. Metha, G. Nathan, Flow seeding with elemental metal species via an optical method, Appl. Phys. B 107 (2012) 665–668.
[23] R. Whiddon, Application of laser-based diagnostics to a prototype gas turbine burner at selected pressures (Ph.D. thesis), Lund University, 2014.
[24] Z.W. Sun, Z.T. Alwahabi, D.H. Gu, S.M. Mahmoud, G.J. Nathan, B.B. Dally, Planar laser-induced incandescence of turbulent sooting flames: the influence of beam steering and signal trapping, Appl. Phys. B 119 (2015) 731–743.
[25] Q.N. Chan, P.R. Medwell, Z.T. Alwahabi, B.B. Dally, G.J. Nathan, Assessment of interferences to nonlinear two-line atomic fluorescence (NTLAF) in sooty flames, Appl. Phys. B 104 (2011) 189–198.
[26] S. Bejaoui, X. Mercier, P. Desgroux, E. Therssen, Laser induced fluorescence spectroscopy of aromatic species produced in atmospheric sooting flames using UV and visible excitation wavelengths, Combust. Flame 161 (2014) 2479–2491.
[27] T. Furuhata, Y. Kobayashi, K. Hayashida, M. Arai, Behavior of PAHs and PM in a diffusion flame of paraffin fuels, Fuel 91 (2012) 16–25.
[28] F. Goulay, P.E. Schrader, X. López-Yglesias, H.A. Michelsen, A data set for validation of models of laser-induced incandescence from soot: temporal profiles of LII signal and particle temperature, Appl. Phys. B 112 (2013) 287–306.
[29] F. Goulay, P.E. Schrader, L. Nemes, M.A. Dansson, H.A. Michelsen, Photochemical interferences for laser-induced incandescence of flame-generated soot, Proc. Combust. Inst. 32 (2009) 963–970.
[30] K. Hayashida, K. Amagai, K. Satoh, M. Arai, Experimental analysis of soot formation in sooting diffusion flame by using laser-induced emissions, J. Eng. Gas Turbines Power 128 (2006) 241–246.
[31] S. Schraml, S. Dankers, K. Bader, S. Will, A. Leipertz, Soot temperature measurements and implications for time-resolved laser-induced incandescence (TIRE-LII), Combust. Flame 120 (2000) 439–450.
[32] R. Vander Wal, K. Weiland, Laser-induced incandescence: development and characterization towards a measurement of soot-volume fraction, Appl. Phys. B 59 (1994) 445–452.
[33] R.L. Vander Wal, K.A. Jensen, M.Y. Choi, Simultaneous laser-induced emission of soot and polycyclic aromatic hydrocarbons within a gas-jet diffusion flame, Combust. Flame 109 (1997) 399–414.
[34] D.H. Gu, Z.W. Sun, P.R. Medwell, Z.T. Alwahabi, G.J. Nathan, Spectral assessment of interferences to two-line atomic fluorescence (TLAF) in Turbulent Sooty Flames, 4th Australian Combustion Symposium, 2013.
[35] J. Hult, I. Burns, C. Kaminski, Two-line atomic fluorescence flame thermometry using diode lasers, Proc. Combust. Inst. 30 (2005) 1535–1543.
[36] N. Qamar, Z.T. Alwahabi, Q.N. Chan, G. Nathan, D. Roekaerts, K.D. King, Soot volume fraction in a piloted turbulent jet non-premixed flame of natural gas, Combust. Flame 156 (2009) 1339–1347.
[37] R. Santoro, H. Semerjian, R. Dobbins, Soot particle measurements in diffusion flames, Combust. Flame 51 (1983) 203–218.
[38] S.B. Dworkin, Q. Zhang, M.J. Thomson, N.A. Slavinskaya, U. Riedel, Application of an enhanced PAH growth model to soot formation in a laminar coflow ethylene/air diffusion flame, Combust. Flame 158 (2011) 1682–1695.
[39] C.S. McEnally, L.D. Pfefferle, Experimental study of nonfuel hydrocarbons and soot in coflowing partially premixed ethylene/air flames, Combust. Flame 121 (2000) 575–592.
[40] C.R. Shaddix, J. Zhang, W. Scheffer, J. Doom, J.C. Oefelein, S. Kook, L.M. Pickett, H. Wang, Understanding and predicting soot generation in turbulent non-premixed jet flames, Report No. Sand2010-7178, 2010.
[41] G.P. Smith, D.M. Golden, M. Frenklach, N.W. Moriarty, B. Eiteneer, M. Goldenberg, C.T. Bowman, R.K. Hanson, S. Song, W.C. Gardiner Jr, V.V. Lissianski, Z.W. Qin, GRI-Mech 3.0, 1999. http://www.me.berkeley.edu/gri_mech/
[42] J.E. Sansonetti, W. Martin, Handbook of basic atomic spectroscopic data, J. Phys. Chem. Ref. Data 34 (2005) 1559–2259.
[43] C. Schulz, B.F. Kock, M. Hofmann, H. Michelsen, S. Will, B. Bougie, R. Suntz, G. Smallwood, Laser-induced incandescence: recent trends and current questions, Appl. Phys. B 83 (2006) 333–354.
[44] F. Cignoli, S. Benecchi, G. Zizak, Time-delayed detection of laser-induced incandescence for the two-dimensional visualization of soot in flames, Appl. Opt. 33 (1994) 5778–5782.
[45] F. Ossler, T. Metz, M. Aldén, Picosecond laser-induced fluorescence from gas-phase polycyclic aromatic hydrocarbons at elevated temperatures. I. Cell measurements, Appl. Phys. B 72 (2001) 465–478.
[46] F. Ossler, T. Metz, M. Aldén, Picosecond laser-induced fluorescence from gas-phase polycyclic aromatic hydrocarbons at elevated temperatures. II. Flame-seeding measurements, Appl. Phys. B 72 (2001) 479–489.
[47] K.C. Smyth, C.R. Shaddix, D.A. Everest, Aspects of soot dynamics as revealed by measurements of broadband fluorescence and flame luminosity in flickering diffusion flames, Combust. Flame 111 (1997) 185–207.
[48] B. Quay, T.W. Lee, T. Ni, R.J. Santoro, Spatially resolved measurements of soot volume fraction using laser-induced incandescence, Combust. Flame 97 (1994) 384–392.
[49] D.R. Snelling, K.A. Thomson, G.J. Smallwood, Ö.L. Gülder, Two-dimensional imaging of soot volume fraction in laminar diffusion flames, Appl. Opt. 38 (1999) 2478–2485.

Chapter 5

Simultaneous imaging of flame temperature and soot volume fraction in a sooting lifted turbulent jet diffusion flame

Statement of Authorship

Title of Paper	Simultaneous imaging of flame temperature and soot volume fraction in a sooting lifted turbulent jet diffusion flame
Publication Status	☐ Published ☐ Accepted for Publication ☑ Submitted for Publication ☐ Unpublished and Unsubmitted work written in manuscript style
Publication Details	Proceedings of the Combustion Institute

Principal Author

Name of Principal Author (Candidate)	Dahe Gu
Contribution to the Paper	Under supervision of G. J. Nathan, Z. W. Sun, P. R. Medwell, Z. T. Alwahabi and B. B. Dally, I developed experimental methods, performed experiments, analysed data and wrote the manuscript.
Overall percentage (%)	55%
Certification:	This paper reports on original research I conducted during the period of my Higher Degree by Research candidature and is not subject to any obligations or contractual agreements with a third party that would constrain its inclusion in this thesis. I am the primary author of this paper.
Signature	Date: 01/02/2016

Co-Author Contributions

By signing the Statement of Authorship, each author certifies that:

i. the candidate's stated contribution to the publication is accurate (as detailed above);

ii. permission is granted for the candidate to include the publication in the thesis; and

iii. the sum of all co-author contributions is equal to 100% less the candidate's stated contribution.

Name of Co-Author	Graham J. Nathan
Contribution to the Paper	I acted as principal supervisor for the Ph.D. candidate, Dahe Gu, aided in development of the experimental methods, revision of the manuscript and evaluation of the final manuscript. I give consent to Dahe Gu to present this paper for examination towards the Doctorate of
Signature	Date: 1/2/16.

Name of Co-Author	Paul R. Medwell
Contribution to the Paper	I acted as co-supervisor for the Ph.D. candidate, Dahe Gu, aided in revision of the manuscript and evaluation of the final manuscript. I give consent to Dahe Gu to present this paper for examination towards the Doctorate of Philosophy.
Signature	Date: 11-FEB-2016

Name of Co-Author	Zeyad T. Alwahabi
Contribution to the Paper	I acted as co-supervisor for the Ph.D. candidate, Dahe Gu, aided in revision of the manuscript and evaluation of the final manuscript. I give consent to Dahe Gu to present this paper for examination towards the Doctorate of Philosophy.
Signature	Date: Feb 11, 2016

Name of Co-Author	Bassam B. Dally
Contribution to the Paper	I acted as co-supervisor for the Ph.D. candidate, Dahe Gu, aided in revision of the manuscript and evaluation of the final manuscript. I give consent to Dahe Gu to present this paper for examination towards the Doctorate of Philosophy.
Signature	Date: 4-2-16

Name of Co-Author	Zhi Wei Sun
Contribution to the Paper	I am a postdoc, co-supervised the experiments, aided in development of the experimental methods, performing experiments, data analysis and results discussion, revision of the manuscript and evaluation of the final manuscript. I give consent to Dahe Gu to present this paper for examination towards the Doctorate of
Signature	Date: 11/02/2016

Please cut and paste additional co-author panels here as required.

Simultaneous measurements of gas temperature, soot volume fraction and primary particle diameter in a sooting lifted turbulent ethylene/air non-premixed flame

Dahe Gu[1,2,*], Zhiwei Sun[1,2], Bassam B. Dally[1,2], Paul R. Medwell[1,2], Zeyad T. Alwahabi[1,3], Graham J. Nathan[1,2]

[1]*Centre for Energy Technology, The University of Adelaide, S.A. 5005, Australia*
[2]*School of Mechanical Engineering, The University of Adelaide, S.A. 5005, Australia*
[3]*School of Chemical Engineering, The University of Adelaide, S.A. 5005, Australia*

*Author to whom correspondence should be addressed:
Dahe Gu
Phone: +61 8 8313 5460
Email address: dahe.gu@adelaide.edu.au

Abstract

Simultaneous, planar measurements of flame temperature (T), soot volume fraction (f_v), primary particle diameter (d_p) and the derived number density of primary particles (N_p) are reported in a well characterized, lifted ethylene jet diffusion flame (fuel-jet Reynolds number = 10,000), both to increase confidence in measurement accuracy and to provide new joint statistics. Planar measurements of temperature were performed using non-linear excitation regime two-line atomic fluorescence (nTLAF) of indium with an improved optical arrangement over those reported previously, and were found to yield good agreement with previous measurements obtained with coherent anti-Stokes Raman spectroscopy (CARS). Planar measurements of soot volume fraction and primary particle diameter were performed using time-resolved laser-induced incandescence (TiRe-LII). The number density of primary particles was then derived from the values of f_v and d_p. The measurements of T were found to yield good agreement with previous measurements obtained with coherent anti-Stokes Raman spectroscopy (CARS). On the centreline, the measured d_p starts to grow with f_v and peaks at $x/d = 105$, shows a similar trend to previously simulated d_p profile. The joint probability density functions (PDF) of the measured T, f_v, d_p and derived N_p were obtained from the two-dimensional images and assessed at 15 locations in the flame (5 radial × 3 axial locations). Strong correlations were found between d_p and f_v, d_p and f_v, N_p and T, N_p and f_v , and N_p and d_p for all flame regions. The changes in PDFs with radial and axial locations and the most probable values are also reported.

Keywords: *flame temperature, soot volume fraction, primary particle diameter, turbulent flame, simultaneous and planar measurement*

1. Introduction

Reliable measurements of well characterised turbulent sooting flames are needed to support the development and validation of predictive models, which in turn are needed to mitigate soot emissions from practical combustion systems that cause deleterious effects on human health and climate change [1-3]. It is also highly desirable that such measurements not only be well resolved spatially and temporally, but also record multiple parameters simultaneously and in multiple dimensions, due to the complex coupling between soot, turbulence, radiation and chemistry. Of these, four parameters of particular interest for modelling soot evolution are soot volume fraction (f_v), primary particle diameter (d_p), number density of primary soot particle (N_p) and flame temperature (T), which influence radiative heat transfer in turbulent flames. However, measurements of these key parameters are rare. Previous studies reported measurements of planar f_v and laser-induced fluorescence (LIF) of polycyclic aromatic hydrocarbons (PAHs) [4], of simultaneous f_v and qualitative hydroxyl radical (OH) concentrations [5] and of simultaneous f_v and velocity [6]. Only a few simultaneous measurements have been reported of T and f_v in turbulent jet flames [7-10] and in pool fires [11, 12] and of f_v, d_p and N_p in turbulent flames [13, 14]. However, none of these are well resolved both spatially and temporally and of known absolute accuracy, which is desirable for model validation. There is therefore a need for new, more accurate and comprehensive data in a well-characterised flame.

A vital aspect of determining absolute measurement accuracy is the need for independent measurements of identical and well characterized flames, which requires measurement by different groups with different methods. However, to date, such independent assessments in turbulent sooting are rare, due the difficulties imposed by the challenging environment of high fluctuations in key parameters for diagnostic techniques [15]. To the best of authors' knowledge, such measurements are yet to be performed for T, f_v, d_p and N_p. While there are several target turbulent sooting flames available [16-20], a good candidate flame for such measurements is that reported by Köhler *et al*. [16, 20], which is a non-premixed lifted turbulent ethylene/air jet flame, due to the relatively simple burner configuration, well studied fuel of ethylene and sufficient soot concentration for accurate

measurement. These characteristics satisfy modelers' needs regarding boundary conditions and flame characteristics [21, 22]. Moreover, the authors performed comprehensive optical measurements, including flame temperature using shifted-vibrational coherent anti-Stokes Raman spectroscopy (CARS), flow velocity using particle image velocimetry, f_v using PLII and planar laser-induced fluorescence (PLIF) of OH and PAHs [16, 20]. This relatively extensive data set makes this flame a good candidate firstly for assessment of measurement accuracy through independent measurements, for example, of T and f_v, secondly, for the provision of new insight and data, though the simultaneous (and planar) measurements.

A key statistical information that is yet to be obtained for the above flame is the joint probability density function (PDF) of T and f_v, which is important for accurate predictions of radiation and validation of soot models. Indeed, very limited data of the joint PDFs of these key parameters are available [7-12], which is attributed to the challenging environments encountered by the diagnostic techniques for simultaneous planar measurements. In particular, simultaneous measurements of f_v using laser-beam extinction and soot particle temperature using two-color pyrometry was performed in piloted ethylene jet flames [7-10] and in JP-8 pool fires [11, 12], which involves a semi-intrusive, two-ended optical-fiber probe integrates over a length of 5 or 10 mm. Alternative non-intrusive optical thermometry methods, such as CARS, are challenging to perform concurrently with the LII technique and have only moderate spatial resolution, typically of a few of millimeters [16, 20]. Simultaneous and instantaneous imaging of T and f_v with a high spatial resolution of ~ 400 μm, using nTLAF and LII, has been demonstrated [17, 23]. However, these flames do not have sufficient soot concentration with peak f_v below 1.0 ppm and the temperature measurements by Mahmoud *et al*. [17] have a relatively high uncertainty (~ 180 K). Particularly, neither of these work provided joint PDFs of T and f_v [17, 23]. Hence, there is a need for reliable joint PDFs in turbulent sooting flames, such as the chosen target flame studied by Köhler *et al*. [16, 20]. This study is driven not only by the need for complete data in well characterized flames, but also by the need for comparison of this with previous measurements of the joint PDFs in other flames. There is also a need for a quantitative comparison of

the accuracy of the nTLAF method against the more well-established CARS method. Such a direct comparison is yet to be reported in turbulent sooting flames and is highly sought after prior to the application of nTLAF in highly turbulent sooting flames to provide dataset for model validation.

The measurements of N_p and d_p are also important for advancing understanding the mechanisms of soot formation and oxidation and validation of soot models. However, available experimental data on N_p and/or d_p are mostly limited to laminar flames [24, 25] and are rare for turbulent flames [14], especially simultaneous and planar data. While the thermophoretic sampling technique can provide reliable and statistical information [26, 27], it has been limited to point-wise measurements. The utilization of Rayleigh scattering and laser-induced incandescence (LII)imaging for measurements of N_p and d_p suffers from the assumption of scattering behavior for soot aggregates is neglected [28] and has unknown accuracy in non-premixed flames. Planar measurements of d_p in atmospheric flames with time-resolved laser-induced incandescence (TiRe - LII) has been found to yield good agreement with results obtained with sampling thermophoretic method [29]. However, TiRe-LII have mostly been applied for steady laminar flames [24, 25], with one exception of using four sequential LII images in an unsteady premixed flame [30]. Therefore, there is a need to extend the application of the instantaneous planar TiRe-LII technique into the turbulent flames, both to advance the ongoing development of the TiRe-LII technique and to provide measurements of d_p in turbulent flames, as well as N_p that can be approximately derived from d_p and f_v.

In light of above background, the present work firstly assessed the accuracy of nTLAF through comparison with previous results measured with CARS in the selected turbulent flame. Then, simultaneous and planar measurements of T, f_v and d_p using the combination of nTLAF with TiRe-LII were presented for 15 different heights in the flame. Results of f_v and d_p along the flame centerline were also compared with previous experimental and simulation results, as well as the joint PDFs of the four key parameters, i.e. T, f_v, d_p and N_p.

2. Experimental arrangement

2.1 Burner configuration

The lifted non-premixed turbulent ethylene flame at atmospheric pressure of Köhler *et al*. [16, 20] was chosen to allow for direct comparison of their measurements of T and f_v to the data acquired in the present study. The burner consists of a stainless steel tube with an inner diameter of 2.0 mm and an outer diameter of 6.0 mm. The fuel tube is tapered from the outer edge to a sharp edge at the exit nozzle over a distance of 10 mm. A co-flow of air flow was delivered through a contraction with a square cross-section of 310 mm × 310 mm at the upstream end, converging to 150 mm × 150 mm over a distance of 450 mm, which differs slightly from the previous geometry [16, 20]. The tip of fuel tube extends 50 mm above the air co-flow nozzle. The annular co-flow was conditioned, first through a marble layer of 50.0 mm thickness and then by a stainless steel honeycomb immediately upstream from the contraction. The burner was mounted vertically and positioned ~ 1.5 m beneath an exhaust hood and no influence of the exhaust hood on the flame was observed. The burner was mounted on a traverse to translate the burner, with the hood, through the optical measurement system.

The flame conditions are listed in Table 1. The instantaneous visible flame length fluctuates between 400 mm and 500 mm and the lift-off height was 26.3 ± 3.9 mm, determined by CH* chemiluminescence. Both the flame length and lift-off height match well with values previously reported [16], indicating that the flame has been reproduced reliably in the present study.

Table 1: Operational conditions for the sooting, turbulent non-premixed ethylene flame.

Exit Reynolds number	10,000
Fuel mass flow	10.4 g min^{-1}
Co-flow air mass flow	320 g min^{-1}
Fuel temperature	298 ± 2 K
Ambient temperature	294 ± 2 K

Mean fuel jet velocity	44 ms^{-1}
Lift off height	26.3 ± 3.9 mm*
Power	8.7 kW
Flame length	~ 450 mm

DLR flame reported a lifted height of 26 mm, as determined by OH chemiluminescence [16] and 22.3 ± 1.5 mm by OH-LIF [20].

2.2 Temperature measurements with nTLAF

For the nTLAF measurement, two Nd:YAG pumped dye lasers (Quantel, TDL 90) were employed to produce laser beams centred at 410.18 nm (the Stokes beam) and 451.13 nm (the anti-Stokes beam) to excite seed indium [31]. Indium nanoparticles was seeded into the flame with an in-house laser ablation system [32, 33]. The nanoparticles undergo thermal decomposition within the flame to release indium atoms. The excitation laser pulse energies were kept at 2.5 mJ and 3 mJ, respectively, which are in the non-linear excitation regime, while the linewidths were 0.4 cm^{-1} and 0.3 cm^{-1}, respectively. The two laser beams with a ~ 120 ns temporal separation were first combined using a dichroic mirror and then focused into a laser sheet using a telescope, which results in an interrogation region with a thickness of ~ 0.4 mm and a height of ~ 10 mm. The vertical energy profile of laser sheets was recorded with a CCD camera (MegaPlus II, ES 4020) and used for the reference laser power to derive temperature.

Laser-induced fluorescence (LIF) of indium were imaged using two intensified CCD (ICCD) cameras (Princeton Instruments, PM4-1024f) both with a constant gate width of 30 ns and mounted with an image-splitter (TwinCam, Cairn). The image-splitter was mounted with a common Nikon *f*/1.4 lens (f = 50 mm) for collection of the two LIF signals and a long-pass dichroic beam-splitter (DMLP425, Thorlabs) for separation of the two LIF signals. This arrangement avoids any influence of differential beam-steering on signal collection, unlike early work [17, 23]. The in-plane spatial resolution was 67 × 67 μm^2. The linearity response of both cameras has an R-squared value of > 0.99

for over 50% of their full dynamic range. Two customized narrow band-pass filters (Alluxa) were employed for fluorescence signals collection and spectral interference suppression, centred at 451.4 nm (FHMW = 1.32 nm) and 410.4 nm (FHMW = 1.08 nm), respectively. The narrow band-pass filters both have a peak transmission of 95% and a high specified optical density (OD) of ~ 6.0 at the excitation laser wavelengths to further suppress laser ELS signals from the soot particles. These narrow-band filters increase both the precision and the accuracy of the measurement, while an uncertainty that is due to the presence of the spectral interferences of 10 K at a location where the f_v is 1.2 ppm, has been reported [34]. The collection angle was verified to achieve uniform collection efficiency in the field of view in the present study. For each flame height, 499 instantaneous shots were acquired. The acquired images were then spatially matched, and corrected for both dark charge and the laser sheet energy profile on a row-by-row basis.

A soot-free premixed ethylene/air flame in a Santoro-type burner was employed for the calibration of the nTLAF system, using the approach adopted previously [31]. The burner consists of two concentric brass tubes of 11 mm and 98 mm inner diameter. Gaseous fuel was injected through the central tube while air was passed through the annular co-flow passage. The central fuel tube extends 4 mm above the surface of the annular air co-flow tube. The flow rates were 0.53 L/min for the C_2H_4 fuel, 3.91 L/min and 127.7 L/min for the premixed air and co-flow air stream, respectively. The flame temperature was measured along the centerline of the flame through the height of the laser sheets using an *R*-type Pt/Pt-Rh 13% thermocouple with a wire diameter of 75 μm (Omega, P13R-003). A correction of 61 K was added to the raw measurement to correct for radiation heat loss.

2.3 TiRe-LII results

Soot volume fraction and primary particle diameter were measured with the TiRe-LII technique described previously [33], while primary particle number density was derived from the values of these two measured parameters by $N_p = f_v/(d_p^3)$. The soot particles were heated with a fundamental output (1064 nm) from a Nd:YAG laser (Quantel, Brilliant B) formed into a laser sheet of ~ 0.6 mm thickness

and co-aligned with the nTLAF laser sheets. The laser fluence of the excitation laser sheet was kept at ~ 0.30 J/cm^2 to ensure that the LII signal is independent of the excitation laser fluence variation without generating significant soot sublimation [35]. Four sequential LII images were collected using four ICCD camera heads (HSFC Pro, PCO) mounted with a 435 ± 20 nm interference filter (Semrock, Brightline FF02-435/40). The gate width of four cameras were all kept at 30 ns and were delayed at 0, 60, 120 and 180 ns relative to the start of the laser pulse. The in-plane spatial resolution of each camera images was 85 × 85 μm^2.

The prompt LII signal was used to determine f_v and was calibrated by performing laser beam extinction measurements in a steady ethylene/air non-premixed flame burned on the Santoro-type burner. The flow rate of ethylene through the central tube was kept at 0.175 L/min and the flow rate of the coflow air was 136.1 L/min, resulting in a flame length of 64 mm and a co-flow velocity of 0.3 m/s. A continuous wave laser at 1064 nm was used for the extinction measurement, which were performed at various heights to reduce the influence of primary particle variation through the flame on the calibration. A value of K_e = 5.66 was chosen for the dimensionless extinction coefficient to the determine soot volume fraction.

The value of d_p was evaluated from the four sequential LII images by comparing the ratios of the collected signals with predictive ratios from a LII model [33, 36]. In this model, the soot particles are assumed to be non-aggregated and the soot particles size to have a mono-disperse size distribution. This model was used to calculate theoretical values of intensity ratio between four collected signals for d_p between 5 and 100 nm with a 5 nm step. A constant gas temperature of 1800 K was assumed in the model, the uncertainty associated with temperature variation is considered to be second order [37] when compared to the precision of the current TiRe-LII technique of ± 20%. For example, a temperature variation of ± 200 K can only result in a change of ± 3 nm for soot particles with d_p = 15 nm or ± 5 nm for d_p = 40 nm [33].

3. Results and discussion

3.1 Images of temperature, soot volume fraction and primary particle size

Figure 1 presents a collage of images of flame temperature, soot volume fraction and primary particle diameter, all averaged over 499 shots, with their corresponding root-mean-square (RMS), and an instantaneous counterpart. Images were collected at 15 heights above the burner to provide data in all key regions of the flame. Mean temperature data in the present work were calculated in two alternative ways to account for the minimum detection threshold of ~ 800 K in the nTLAF method, which is due to the temperature sensitivity of the seeded indium [38, 39] or to the lack of indium LIF signal in some locations due to insufficient seeding or oxidation of indium atoms in the flame. In one method, the averaged flame temperature is calculated assuming that the temperature of any data point for which no temperature measurement was obtained is ambient, i.e. 300 K, which is denoted $T_{<800K=300K}$. The second method removes such measurements, which corresponds to a conditional measurement, denoted $T_{>800K}$. These two measurements can be considered as the lower and upper bounds of the mean temperature, respectively, to provide confidence in the mean data where the two methods agree. In addition, even in some regions where temperature > 800 K, there are some local regions in which atomic indium may not be available. The significance of this is assessed by reporting the fraction of the data set for which good data are obtained, termed $F_{good\ data}$, which is defined by calculating the fraction of the temperature data that is greater than 800 K. Slight asymmetry was found in all mean images of T, f_v and d_p, which have higher value on the left side (laser entrance) than the right side (not shown in Fig. 1, see radial profiles of f_v in Fig. 4). Since the asymmetry persists after rotating the burner, it may be deduced that this asymmetry was not caused by an uneven flow distribution. Furthermore, this finding is consistent with the asymmetry in f_v reported by Köhler *et al*. [20]. This asymmetry is likely to be associated with the local laser fluence decrease when nTLAF and LII laser sheets cross the flame, caused by beam steering and laser attenuation due to high local f_v, and signal trapping [40, 41].

Figure 1a shows that a measurement of $T_{<800K=300K}$ is obtained in most regions of the flame, except near to the axis and with a flame height (h) between 40 mm and 120 mm. Figure 1b shows that the soot starts to become detectable at a height of ~ 120 mm and extends to the flame tip ~ 420 mm, similar to the temperature distribution detected with nTLAF. In the middle height regions of the flame, i.e. between 200 mm and 350 mm, the radial width of measured temperature is wider than f_v and d_p, indicating nTLAF is capable of measuring temperature on either side of soot sheets. The instantaneous images in Fig. 1d and 1e confirm that the region of measureable temperature is instantaneously over a wider region than that of the soot, which is important for reliable joint PDFs. The temperature RMS image shows the radial fluctuations are small for $h < 230$ mm and increase towards the flame tip, consistent with single-shot image shown in Fig. 1d.

The peak f_v in the mean image is ~ 0.52 ppm and ~ 4.7 ppm at $h = 310$ mm in the instantaneous image, compared with corresponding values of 0.54 ppm and 4.5 ppm at $h = 300$ mm reported by Köhler *et al*. [20]. The average values of f_v (Fig. 1b) are an order of magnitude lower than the instantaneous values (Fig 1d), consistent with previous measurements [5, 42], which is due to both the highly intermittent nature of the soot distributions [18] and the isolated, highly-wrinkled structure of the soot distribution. In the burnout region of the flame, i.e. $h \sim 375$ mm, although the mean f_v decays from the peak of 0.52 ppm at $h = 310$ mm, the instantaneous f_v can still reach a maximum of 4.6 ppm, indicating the number of occurrence of detectable f_v is less than at the lower flame positions, consistent with findings from previous measurements [Kohler Qamar Crosland]. The dimension of the soot sheets was found to be larger in the burnout region than that of lower flame locations, consistent with the previous measurements [16, 18] . It should also be noted that f_v is detectable at $h \sim 425$ mm in the mean image while T is not detectable at this height. This may be because: 1) nTLAF measurements were biased since indium was consumed and temperature is relatively cold in this region; and 2) the fluctuation in f_v is much larger than that of T due to quick oxidation. The f_v RMS image is wider and higher in magnitude than the mean image, also indicating the highly fluctuating

nature of the soot sheets in turbulent flames, both in magnitude and spatial distribution. The comparison of instantaneous T and f_v images (Fig. 1d and 1e) reveals that soot sheets are generally found in the low temperature regions on the rich side of the high temperature reaction zones, consistent with earlier measurements [7, 9, 11].

Figures 1c and 1f show that d_p grows from the outer edge of the flame at h = 120 mm towards the central region at downstream locations, peaks at h = 310 mm on the axis with an averaged value of 16 nm and ~ 80 nm in the instantaneous images and oxidises at the flame tip. The measured values of d_p are comparable with the measured values of d_p by TiRe-LII in laminar ethylene diffusion flames [25, 37], an unsteady ethylene/air premixed flame [33] and simulated results in a different ethylene turbulent jet diffusion flames [43]. For h > 150 mm, the d_p RMS image has a similar width and magnitude to the mean image, indicating the fluctuation in d_p is less than that of f_v, but larger than that of T.

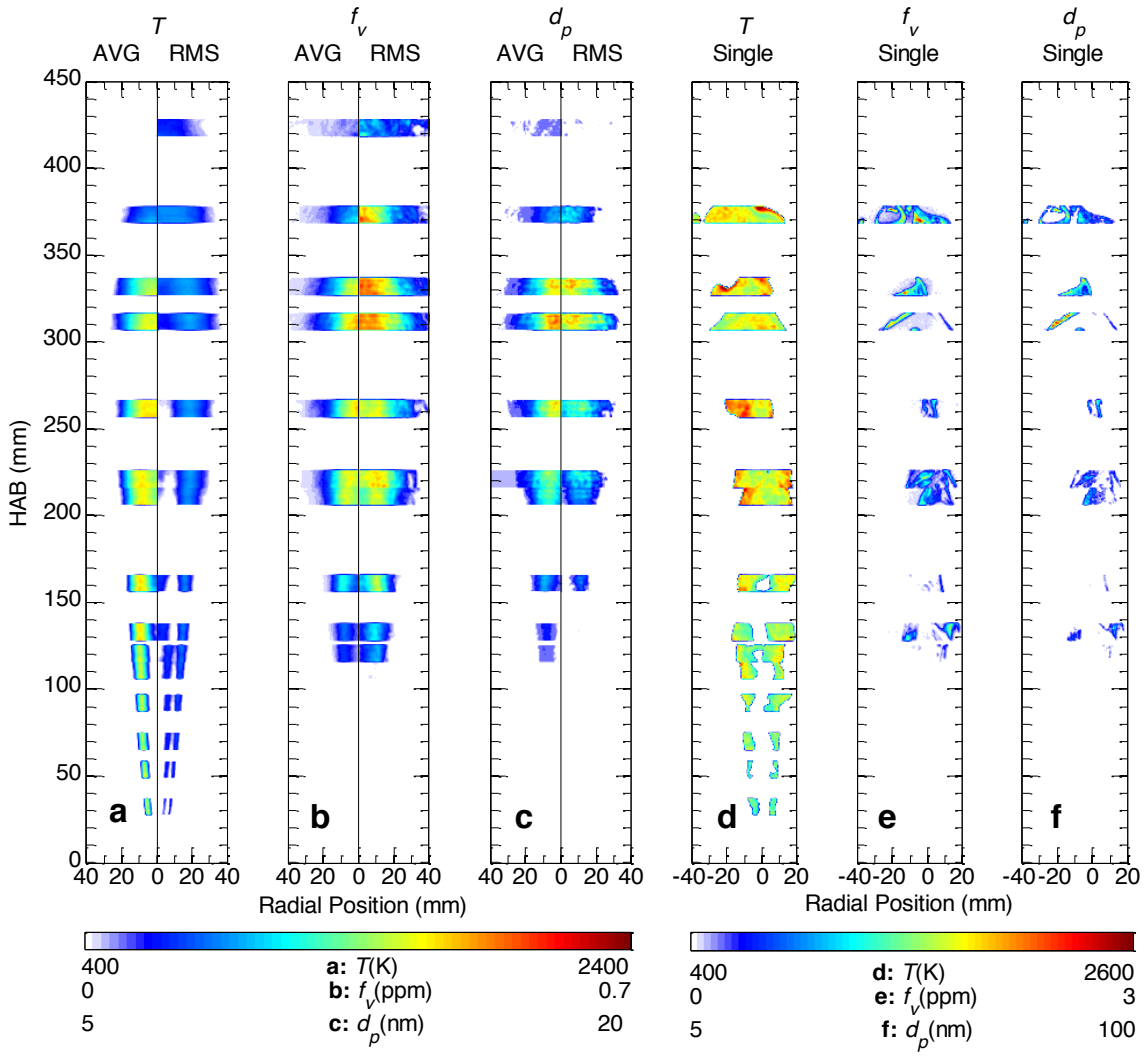

Figure 1: Pseudo colour images of: (a) the averaged flame temperature ($T_{<800K=300K}$) and corresponding RMS; (b) the averaged soot volume fraction (f_v) with a maximum $f_v = 0.52$ ppm and corresponding RMS; (c) the averaged primary soot particle diameter (d_p) and corresponding RMS; typical single-shot images of T; (d) single-shot images of f_v with a peak f_v of ~ 4.7 ppm and (e) single-shot images of d_p.

3.2 Temperature data

Figure 2 presents the probability density functions of flame temperature on the axis at selected heights, together with the Gaussian fits, both for the present nTLAF measurements and for the previous CARS measurements [20]. The nTLAF data presented were extracted from 499 (for Figs. 2a, c, d, e and f) and 998 (for Figs. 3b and g) instantaneous image pairs, respectively, with each measurement averaged

from a sub-array of adjacent pixels to increase signal-to-noise ratio in the raw LIF images. Most data are reported from a 5×5 pixels array (0.33×0.33 mm^2) that is comparable with the light sheet thickness of ~ 0.4 mm, while some data are reported for smaller resolutions, as shown in Fig. 2e. The PDFs at measurement each location are calculated from a further array of 5×5 neighbouring points, i.e. each measurement location has a total sample size of either 12475 or 24950 measurement points. The corresponding spatial resolution of the CARS measurement is 2.2×0.3 mm^2 and the corresponding number of samples is 1200 shots.

The temperature distributions from the nTLAF and CARS measurements are in good agreement over the region between $158 < h < 418$ mm, as shown in Figs. 2c-g. The poor agreement for $h < 78$ mm, where the nTLAF distribution over-predicts the temperature statistics, can be explained by the high probability that the temperature is below the lower detection limit of the nTLAF technique as evident that $F_{good\ data} < 0.36$. This shows that the nTLAF measurements in these regions of high probability of low temperature should be treated with caution. The significance of the fraction of the conditions for which no data are recorded can be assessed from the values of $F_{good\ data}$, as presented in Fig. 2h. This shows that $F_{good\ data}$ is larger than 0.9 over the region $158 < h < 308$ mm and is also greater than that of corresponding CARS measurements in this same region. Furthermore, while the value of $F_{good\ data}$ decreases towards the flame tip for $h > 308$ mm, the values of measured temperature are comparable with the CARS measurement except for the region very close to the flame tip ($h = 420$ mm), where $F_{good\ data}$ is 24.1% and 61.2% for nTLAF and CARS measurements, respectively.

The most probable values of measured temperature, denoted T_{mp}, are found to agree within 30 K for the nTLAF and CARS data over the range $158 < h < 418$ mm. The width of the nTLAF data distribution is slightly wider than that of the CARS data for $208 < h < 308$ mm. This is attributed to the combination of inter-pixel noise in the raw LIF images and to the variation in the laser mode from shot-to-shot. Figure 2e presents the influence of spatial resolution on the measured temperature. It can be seen that increasing the spatial resolution, and hence lowering the signal-to-noise ratio, results both

in a wider distribution of the PDF and in a higher value of T_{mp} than that from the low spatial resolution. This trend is real, because high spatial resolution is subject to increased noise in the temperature calculated from a larger number of samples, which will increase the scatter in the temperature data. The spatial resolution of 0.33 × 0.33 mm^2 gives generally good agreement with the CARS data, with the slightly wider distribution consistent with a slightly smaller probe value, which is the reason that this spatial resolution has been selected for further analysis.

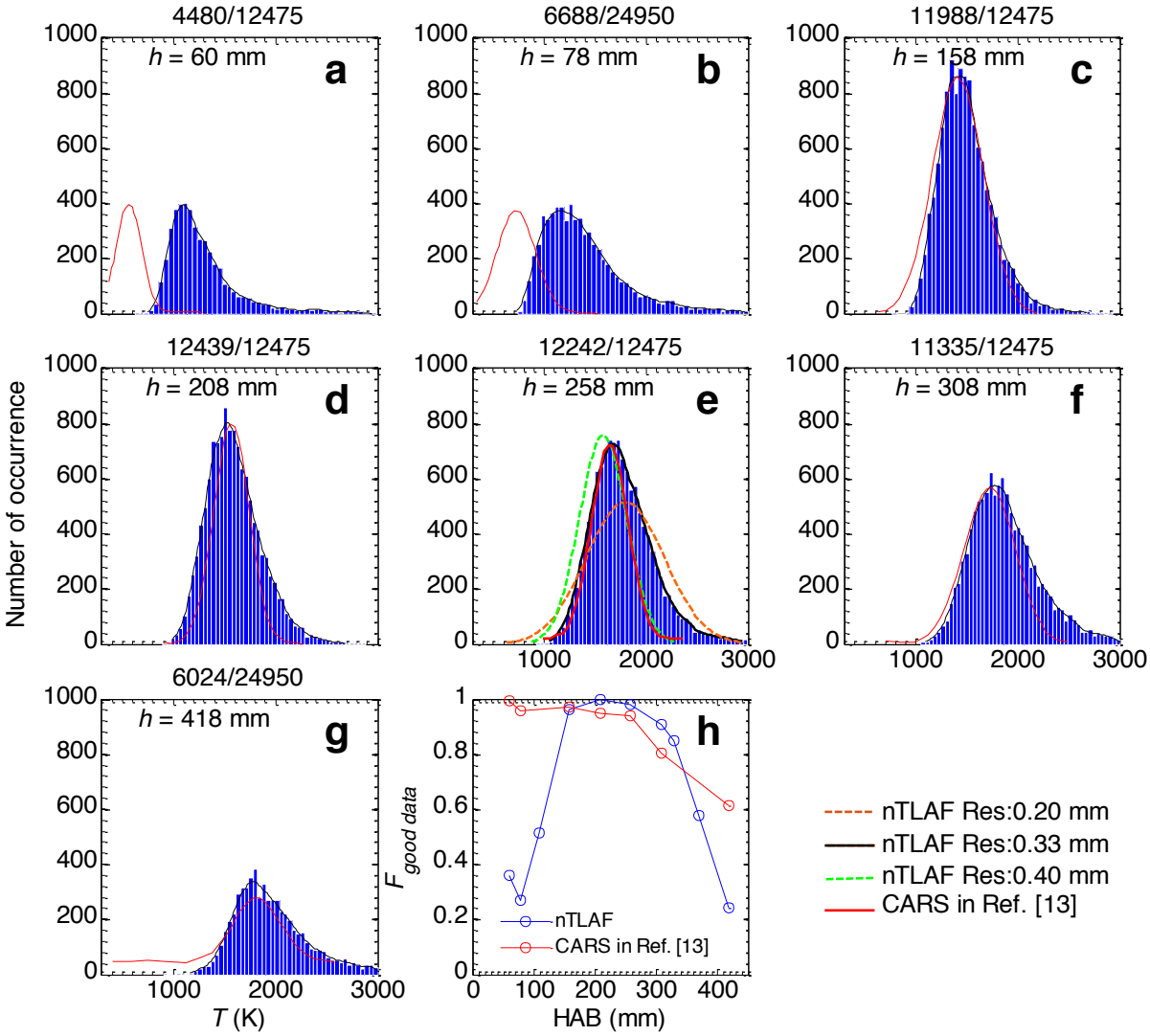

Figure 2: (a-g) Probability density functions (PDF) of instantaneous temperature at selected centreline locations. The number above each figure correspond to the number of good temperature measurements and the sample size of temperature measurements for the nTLAF measurements. Fitted

curves from CARS measurement [20] are shown in red lines. Part (h) presents the axial evolution of the fraction of good temperature data, along the centreline. Part (e) presents the various fitted curves acquired from nTLAF data with different spatial resolutions to the 0.33×0.33 mm^2 reference case.

Figure 3 presents the axial and radial profiles of temperature from the nTLAF and CARS measurements [20]. As shown in Fig. 3a, both the values of $T_{<800K=300K}$ (black circles), corresponding to the lower bound of mean nTLAF temperature and the values of $T_{>800K}$ (blue circles) yield good agreement with the CARS data in the central region of the flame ($140 < h < 300$ mm). The convergence of $T_{<800K=300K}$ with $T_{>800K}$ implies a high reliability of the statistical measurements at that location. For $150 < h < 130$ mm and $h > 300$ mm, the value of $T_{<800K=300K}$ is lower than CARS data while the value of $T_{>800K}$ is larger, which is consistent with low values of $F_{good\ data}$ there. The same trends can be found in the radial profiles. The good agreement between $T_{<800K=300K}$ and CARS data, and the overestimation of $T_{>800K}$ compared with the CARS data for $r < 5$mm at $h = 113$ mm show that gases below 800 K within this region are dominated by entrained ambient air. There is some disagreement between the three methods at $h = 113$ mm and $r = 9$ mm, where $T_{<800K=300K}$ matches well with $T_{>800K}$ at 1721 K, but both nTLAF results are lower than T_{mp} and T_{mean} of CARS data by 186 K and 400 K, respectively. Towards the outer region, i.e. $r > 9$ mm, the $T_{>800K}$ and $T_{<800K=300K}$ increasingly deviate from each other again as expected, due to the increasing significance of the temperatures below 800 K caused by the turbulent fluctuations of the flame. While no comparisons with the CARS data are available here, these upper and lower-bounds to the data are nevertheless useful, and it can be expected that the lower bound will yield a good approximation of the unconditional data.

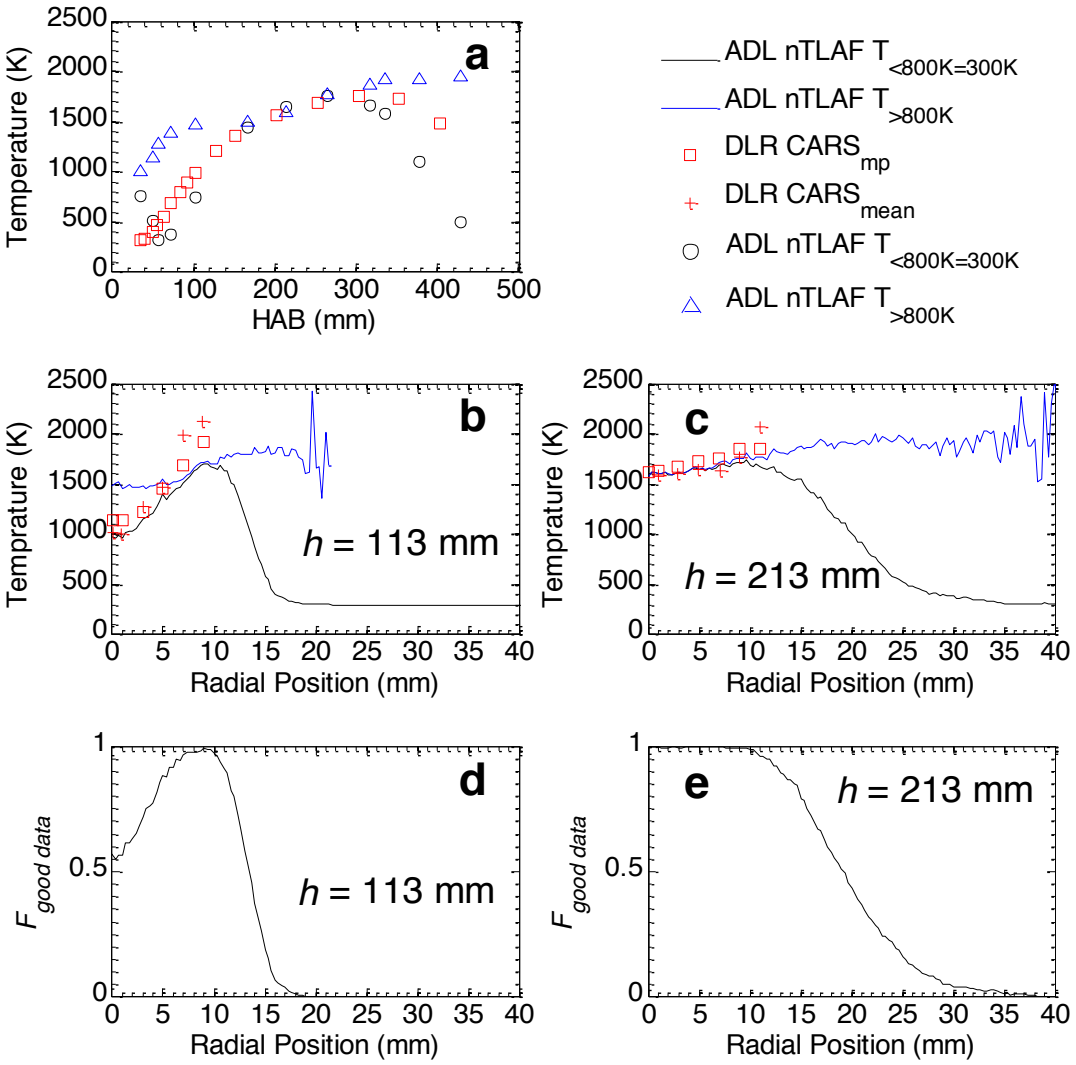

Figure 3: Comparison of the nTLAF data (0.33 mm resolution) obtained from 499 images with CARS data obtained from 1200 shots. (a) Axial profiles; radial profiles at (b) h = 113 mm and (c) h = 213 mm. The averaged lower-bound temperature ($T_{<800K=300K}$) from nTLAF data is shown in black lines, while the upper-bound conditional mean temperature ($T_{>800K}$) is shown in blue lines. The most probable (T_{mp}) and mean (T_{mean}) temperature from CARS measurements [20] are shown in red stars and circles, respectively.

3.3 Soot volume fraction and primary particle diameter data

Figures 4a and 4b present comparisons of the axial profiles of measured f_v and d_p from the present work with previous values of the measured f_v and simulated d_p [20]. The two measured axial profiles of f_v are in good agreement with each other, with a maximum difference of ~ 13% for $200 < h < 300$ mm and an agreement of within 5% for the other positions. For $h < 150$ mm along the axis, d_p is below the detection limit of 5 nm. The measured d_p starts to grow with f_v and peaks at $h = 310$ mm on the axis with an averaged value of 16 nm. The mean d_p then decreases towards the flame tip at a rate faster than it grows, similar to the f_v trend. Although the measured mean d_p axial profile disagrees with simulated d_p profile in absolute soot particle size, the trends are similar, except for $h > 350$ mm, where the measured d_p continues to decrease and the simulated d_p rises again.

The radial profile of f_v at $h = 120$, 160, 310 and 330 mm are shown in Fig. 4c, and compared with the previous measurements [16]. The profiles show that the peak value is away from the axis for $h \leq 160$ mm on the axis at more downstream locations. Very good agreement is found between the two sets of the f_v measurements, although the width of the present f_v profile is somewhat less than the previous one [16], as shown in Fig. 4c. Since the centerline f_v profiles agree well, this is unlikely to be due to misalignment of the laser sheet with the axis of the flame. It is possible that slight difference in the environment, such as the influence of the ambient, may play a role, but the reason for this discrepancy is still unclear. Distinct asymmetry can be seen for $h \geq 120$ mm in both f_v profiles, which is attributable to a reduction in the laser fluence with propagation distance by the high f_v and/or by the influence of beam steering due to turbulence.

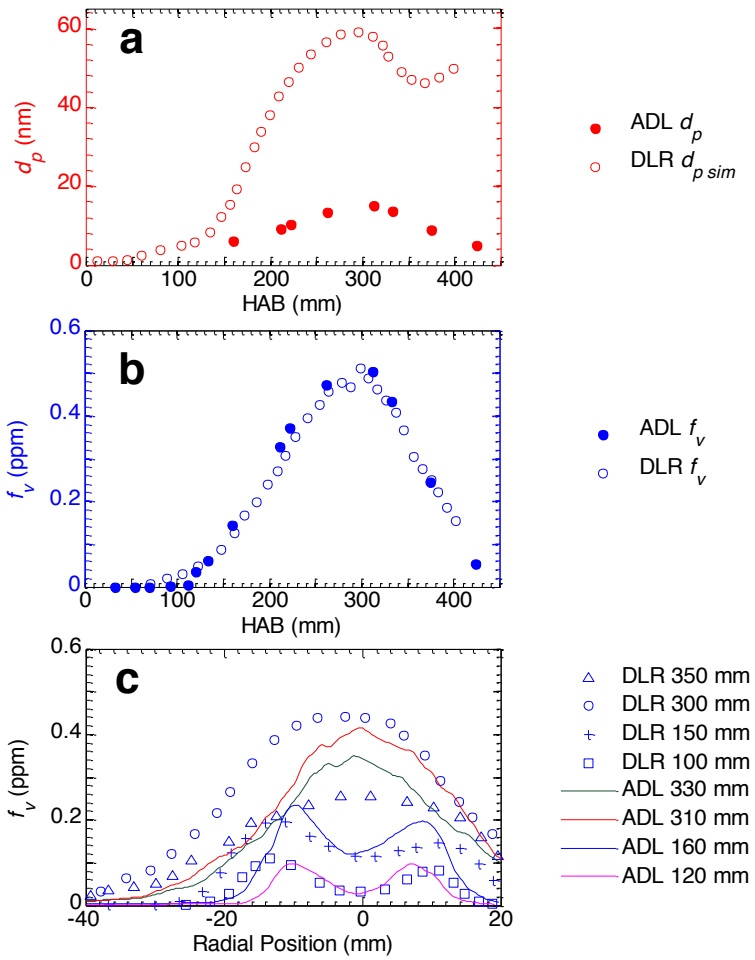

Figure 4: Comparison of the present and previously measured f_v, and of the present measured d_p with previously simulated d_p [16]. (a) Axial profiles of f_v and d_p. (b) Radial profiles of f_v at selected heights.

3.4 Joint statistics of T, f_v, d_p and N_p

Three radial locations at five flame heights have been selected to analyse the instantaneous correlations between T, f_v, d_p and N_p. The three radial locations at each flame height are on the centreline, 50% and 90% of the half width of the flame (denoted as W_f), respectively and are all on the laser entrance side of the flame. i.e. left side. The flame width is determined by the contour of f_v. The position at which the joint statistics were obtained relative to the mean f_v image, is illustrated by the black dots in Fig. 5.

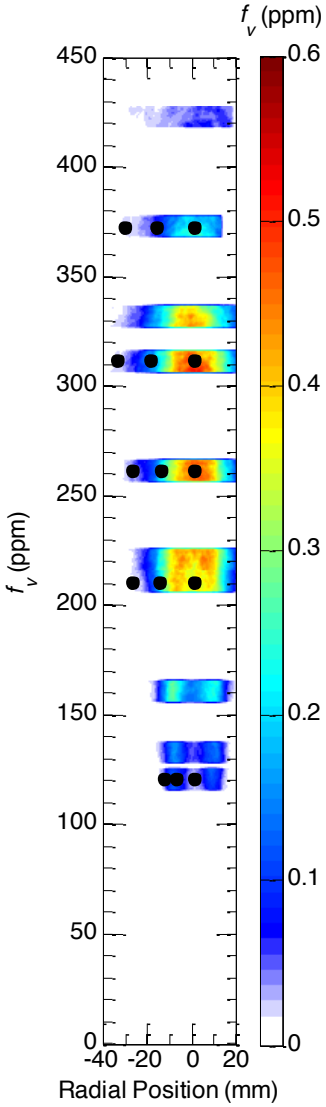

Figure 5: Pseudo colour images of the averaged soot volume fraction overlayed with selected positions for the joint PDFs presented below (*black dots*).

Figure 6 presents the joint PDFs between T and f_v. The pseudo colour contours represent the probability while the outer blue line defines the boundary at which probability approached zero. These statistics from the instantaneous data show that a strong but not circular correlation distribution exists between T and f_v at all chosen locations. The distributions of the PDFs show a strong dependence on axial distance, while the dependence on radial distance is much stronger near to the base of the flame than at the tip. This is broadly consistent with previous findings reported by Mahmoud *et al*. [17], Coppalle *et al*. [7] and Shaddix *et al*. [10], although the present work finds a stronger dependence on radial distance near to the base of the flame. On the axis of the flame, soot is typically formed between 1400 and 2000 K with the peak f_v found between 1550 and 1750 K. These temperatures are higher than previously reported values between 1500 and 1700 K [7] and between 1350 and 1550 K [10], which were obtained at different flame conditions and with different measurement techniques. The range of f_v is very large, varying over some two orders of magnitude, similar to earlier findings [7, 10]. The distribution of T along the axis is widest near to the middle of the flame where f_v peaks, while the width of this peak also increases with radial distance, particularly at upstream locations, i.e. near to the base of the flame. This is slightly different from the trends reported previously, it was found that the joint PDF between T and f_v is mainly dependent on the axial distance and only very weakly depend on radial location [17]. That is, the nature of the distribution depends strongly on the position within the flame, a simple relationship between T and f_v may not be applied generally throughout the flame.

Along the centreline of the flame, at $x/d = 67$, it was found the most probable f_v is ~ 0.02 ppm, increasing to ~ 0.1 ppm for $105 < x/d < 132$ mm and then decreasing slightly to 0.08 ppm at $x/d = 155$. At the flame tip of $x/d = 187$, it decreases to ~ 0.02 ppm. The most probable corresponding temperature, which increase with axial distance and then slightly decrease at the flame tip, are 1420 K,

1500 K, 1640 K, 1900 K and 1850 K respectively. These trends of most probable T and f_v are with good qualitative agreement with the measurement of Shaddix *et al*. [10] at $x/d = 140$ and $x/d = 200$ and, although their most probable values of f_v are somewhat higher at ~ 0.4 ppm for $x/d = 140$ and 0.1 ppm for $x/d = 200$. However, these differences are not inconsistent given the larger size of their flame, their use of a pilot to achieve an attached flame instead of the present lifted flame and different measurement techniques were employed. As shown in Fig. 6, similar trends in the most probable values of T and f_v can be found at $R = 0.5W_f$ with a slightly less change in the most probable f_v with the axial distance. At the flame edge of $R = 0.9W_f$, neither the most probable values of T nor f_v change much. From the flame centreline to $R = 0.5W_f$, both the value of the most probable f_v and the number of events with high f_v decrease, while the most probable value of T increases, consistent with an increasing probability of oxidation through the high temperature region. It is worth noting that, the most probable values of f_v in the joint PDFs are some four to five times lower than the corresponding mean values of $f_v = 0.45$ ppm at $x/d = 132$. They are also lower at $x/d = 105$ and 155 by factors of about three and five, respectively. This is found not only consistent with the large value of RMS of f_v shown in Fig. 1b, but also consistent with the very large difference between instantaneous and mean values.

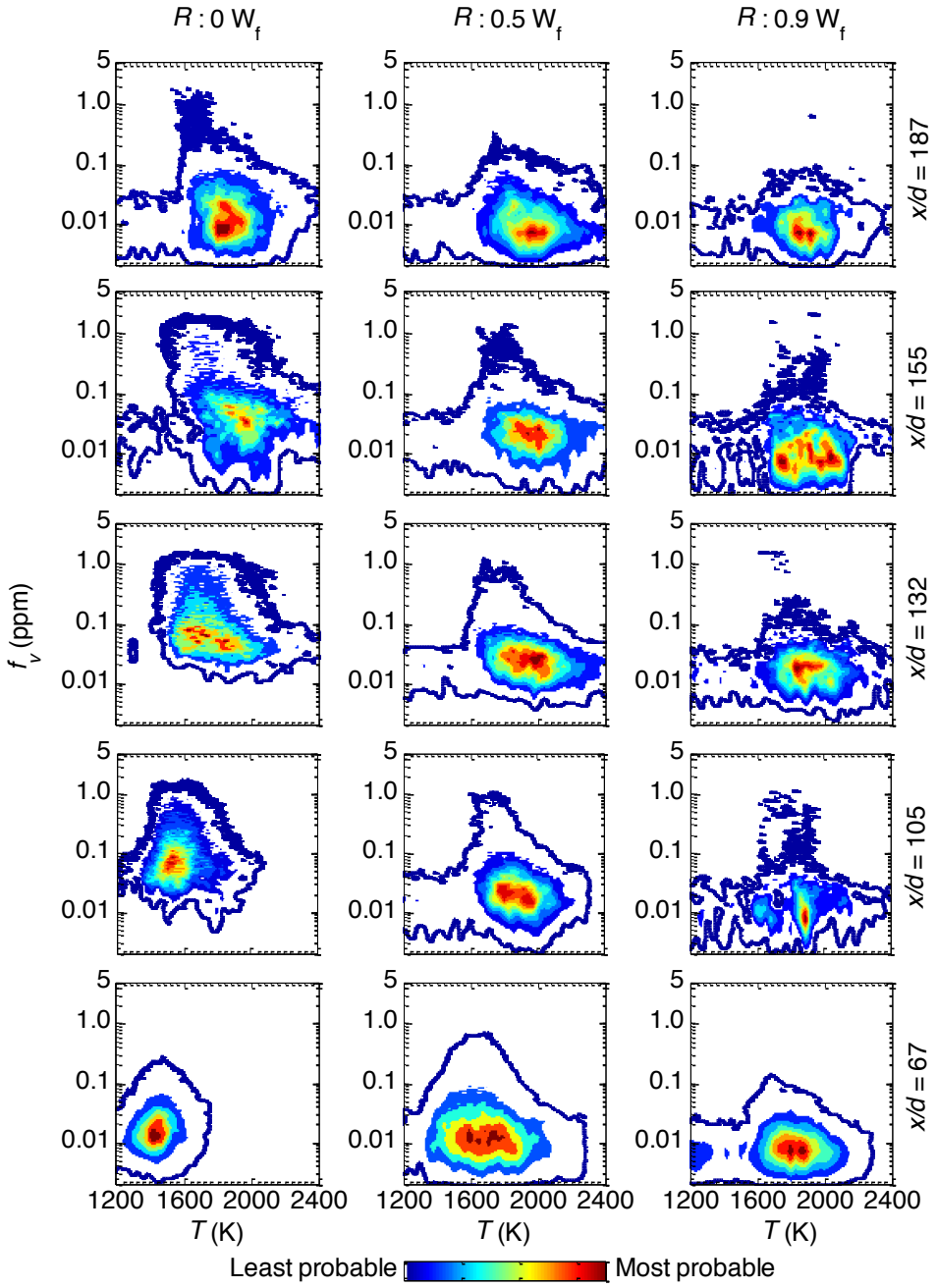

Figure 6: Joint PDFs of T and f_v at selected axial and radial locations (see Fig. 5 for positions). Statistics were calculated from 499 image sets over an area of 5 (radial) × 3 (axial) mm^2, i.e. 15 × 9 neighbouring points, each binned from 5 × 5 pixels.

Figure 7 presents the joint PDFs between d_p and f_v. A strong correlation exists between d_p and f_v at all locations, which also exhibits some consistency with both radial and axial distance. The trend is clearly shown by comparing the joint PDFs data with a reference curve shown in all subfigures. The reference curve is fitted for the joint PDF data at $x/d = 105$ and $R = 0\ W_f$ based on the power-law function: $f_v(d_p) = 0.127 \times {d_p}^{0.694} - 0.318$. For all locations, the most probable value of d_p is between 8 and 18 nm, while the corresponding most probable f_v is between 0.1 and 0.5 ppm. Large primary soot particles with $d_p > 30$ nm mostly correspond to $f_v > 1$ ppm. There is a slight trend of data being below the reference power-law curve near to the edge of the flame, showing that diameter relative to volume fraction decreases with radial distance due to oxidation. It is also significant that the distribution of range of d_p increases with both axial and radial distance because of surface growth and coagulation. The span of d_p is much greater toward the flame tip, even though it falls closely on the power-law curve throughout. At downstream flame locations, the increase in the distribution range of d_p with axial distance is consistent with a much wider range of evolution of soot particle histories. At the centreline, both d_p and f_v grow from $x/d = 67$ to $x/d = 155$ mm and the mean value of d_p decreases slightly at the flame tip. Similar trends can be found at $R = 0.5W_f$ and $R = 0.9W_f$. The width of d_p for a given f_v value decreases radially from the centreline to the flame edge, while the maximum d_p increases radially for a given height.

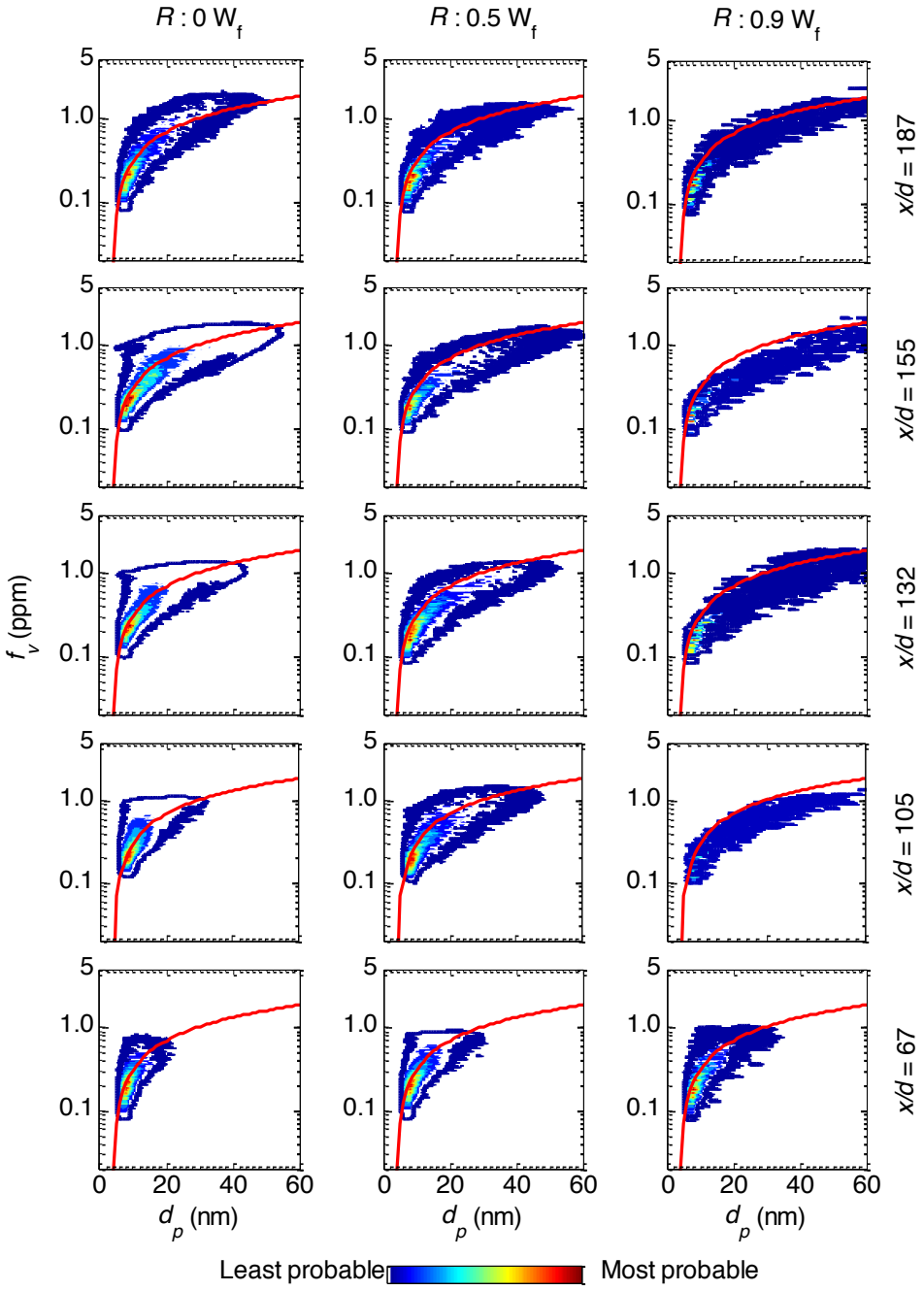

Figure 7: Joint PDFs of d_p and f_v at selected axial and radial locations. Statistics were calculated from 499 image-sets over an area of 5 (radial) × 3 (axial) mm^2, i.e. 15 × 9 neighbouring points (with each point binned from 5 × 5 pixels). The red line corresponds to a power-law function fitted from experimental data.

Figure 8 presents the joint PDFs between T and d_p at selected locations, showing a strong correlation between T and d_p on the axis and near to the base of the flame. This correlation becomes weak with both axial distance towards the tip and with radial distance toward the flame edge. That is, both the value and the range of the most probable d_p increases with axial and radial distance. Also, the small soot particles are found at a wider range of T than the larger soot particles. At any given positions, the most probably T is almost independent of d_p, except near to the tip, where there is a weak trend that the larger soot particles are most likely at relatively low temperature ranges. This is consistent with the joint PDFs of T and f_v, as shown in Fig. 6. It should also be noted that soot particles of different sizes can be found at the flame edge, where f_v is small (see Fig. 6).

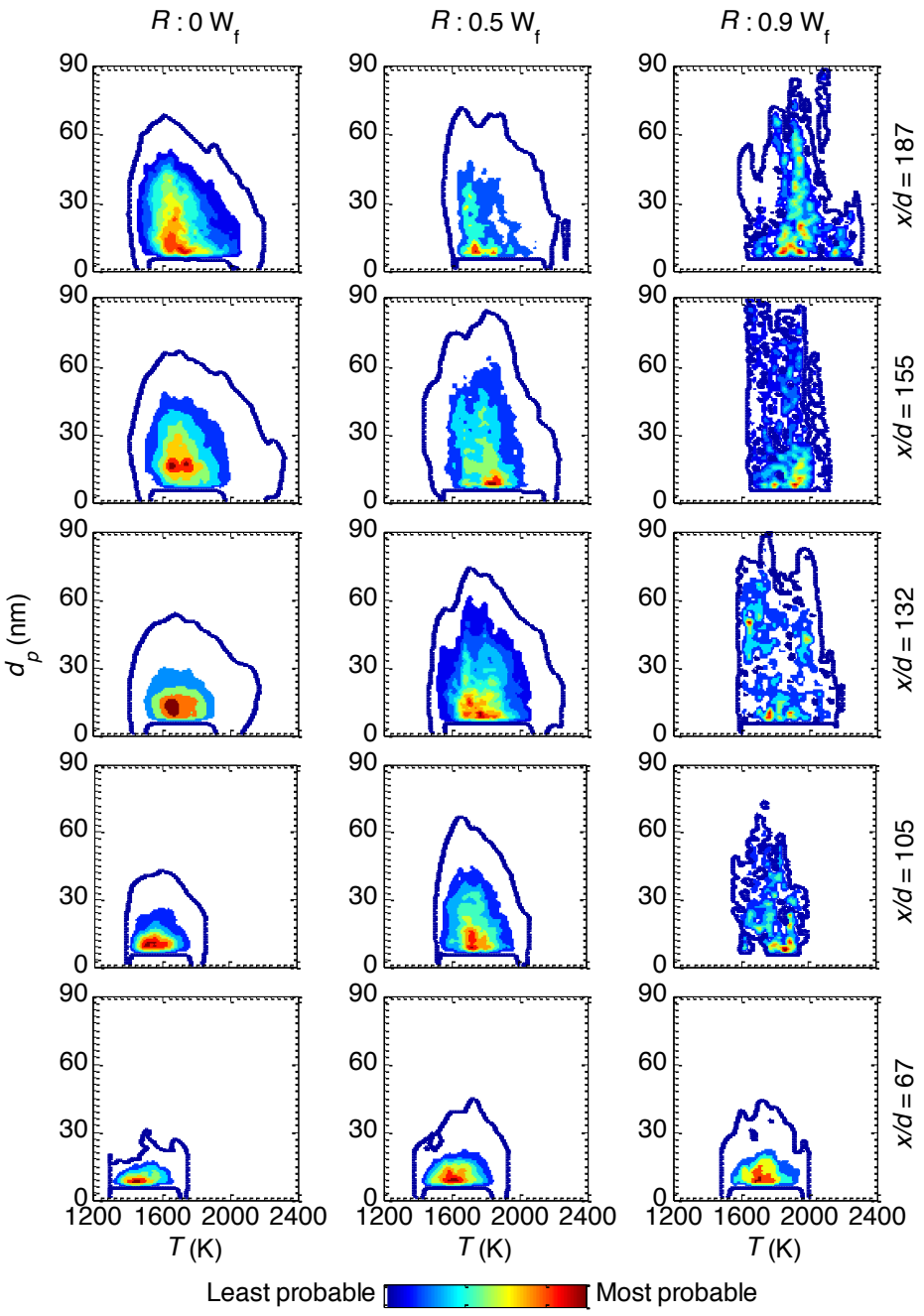

Figure 8: Joint PDFs of T and d_p at selected axial locations and radial locations derived from 499 image sets. Statistics were calculated from an area of 5 (radial) × 3 (axial) mm^2 which consists of 15 × 9 neighbouring points (each point derived from 5 × 5 pixels).

Figure 9 presents the joint PDFs between N_p and T. For all locations, the most probable N_p is between 10^{16} and 10^{17} m^{-3}, and is decreasing from the flame axis towards the flame edge, while the corresponding most probable T varies with flame locations. The most probable N_p increases axially from the flame base to $x/d < 132$, indicating soot inception take places in these regions. The most probable N_p then decreases towards the flame tip, indicating soot particle coagulation and oxidation occur. The value of N_p reaches a maximum of $5.0 \cdot 10^{17}$ m^{-3}at $x/d = 105$ on the flame axis. It was also found that the maximum value of N_p decreases from flame centre towards flame edge at all selected flame heights, while the value of most probable N_p also decrease with radial distance.

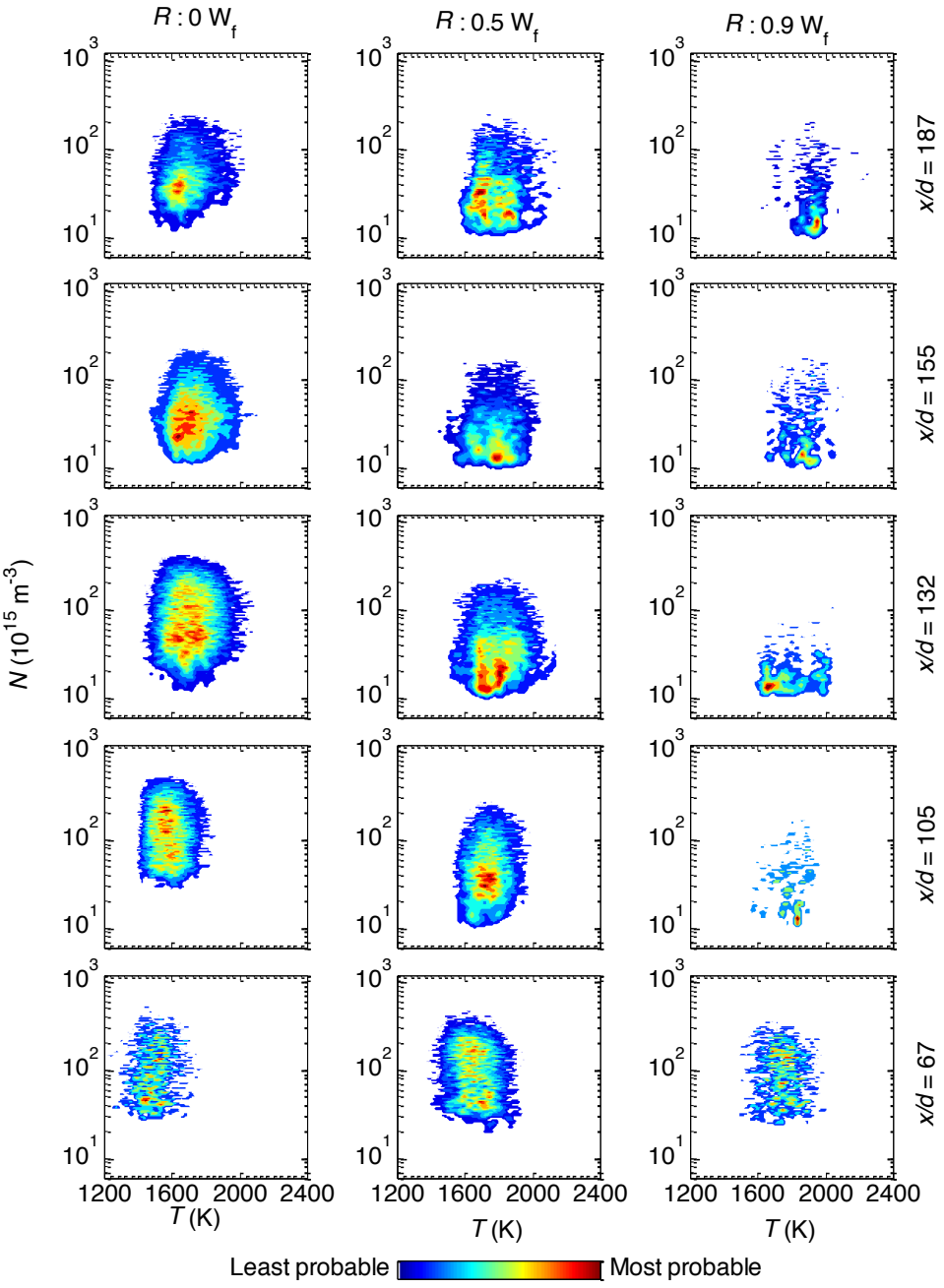

Figure 9: Joint PDFs of N_p and T at selected axial and radial locations. Statistics were calculated from 499 image-sets over an area of 5 (radial) × 3 (axial) mm^2, i.e. 15 × 9 neighbouring points (with each point binned from 5 × 5 pixels).

Figure 10 presents the joint PDFs between N_p and f_v. A strong correlation can be seen between N_p and f_v at selected locations. The most probable value of N_p is between 10^{16} and 10^{17} m^{-3} and the

value of the corresponding most probable f_v is between 0.05 and 0.2 ppm. The value of N_p increases with the increase of f_v for $f_v < 0.4$ ppm and decreases when f_v exceeds 0.4 ppm. The maximum value of N_p in all cases is ~ 5.0×10^{17} m^{-3} and the corresponding f_v is ~ 0.4 ppm. For $f_v > 0.4$ ppm, the joint PDFs of N_p and f_v were fitted with an exponential function, i.e. $N_p(f_v) = a \times f_v^{\,b}$. A reference exponential function, which is calculated from the PDF at $x/d = 132$ and $R = 0W_f$, was plotted against experimental data in all subfigures in Fig. 10, to identify the trend of the PDFs for $f_v > 0.4$ ppm. Figure 11 presents the fitting coefficient, b, here denoted K_{Nf}, for selected axial and radial locations. It can be found that the value of K_{Nf} increases with flame heights at all three selected radial locations, i.e. the decrease in N_p with the increase of f_v decreases at downstream locations when compared to upstream locations, as shown in Fig. 11a. The decrease in N_p with the increase in d_p increases from the centreline of the flame towards the flame edge, as shown in Fig. 11b.

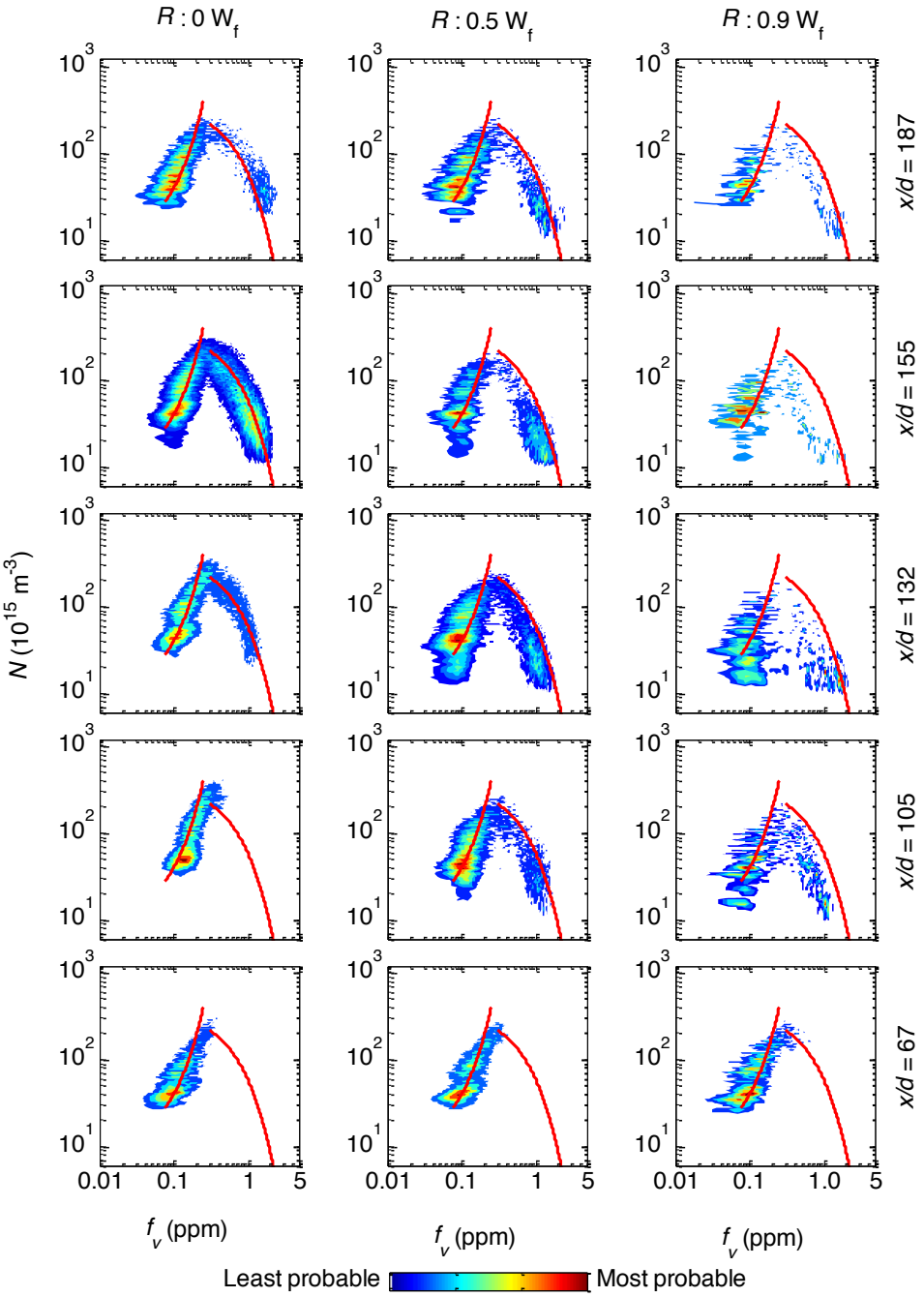

Figure 10: Joint PDFs of N_p and f_v at selected axial and radial locations. Statistics were calculated from 499 image-sets over an area of 5 (radial) × 3 (axial) mm^2, i.e. 15 × 9 neighbouring points (with each point binned from 5 × 5 pixels). The red line corresponds to a reference exponential-law function fitted from experimental data.

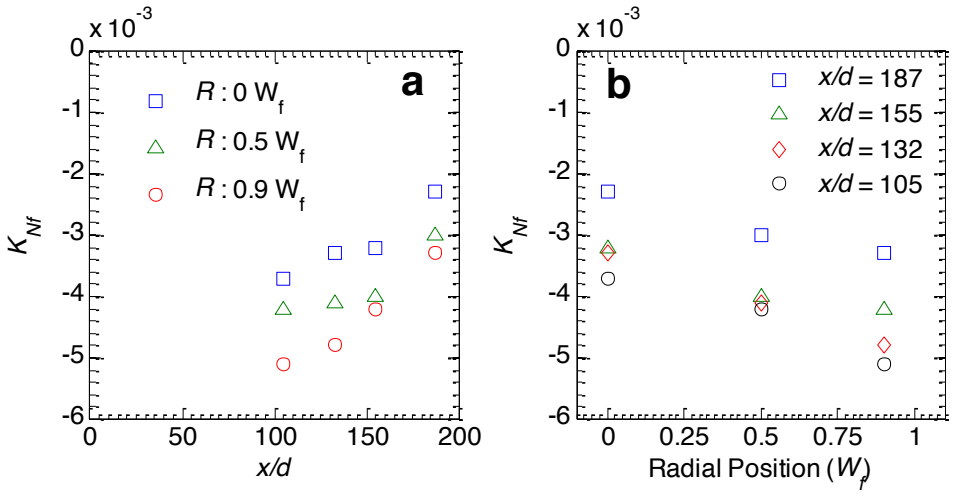

Figure 11: Coefficients of the fitted exponential function for experimental data between N_p and f_v, along (a) the axial and (b) radial direction.

Figure 12 presents the joint PDFs between N_p and d_p. A strong correlation can be seen between N_p and d_p at all selected locations. At the base of the flame (x/d = 67 and x/d = 105), N_p increases with the increase of d_p for d_p < 12 nm, indicating that the soot inception by coagulation of PAHs is taking place in these regions. At downstream and outer radial locations, where d_p > 12 nm, N_p decreases with the increase of d_p. This indicates the soot particles undergo coagulation and oxidation. It is worth noting that at x/d = 132 and x/d = 155, the most probable value of N_p decreases from 5.0×10^{17} m^{-3} to 1.0×10^{17} m^{-3} from the central flame region towards the flame edge, while the corresponding most probable d_p is shifted from 30 nm to 50 nm, indicating the large soot particles are brought by turbulent transport rather than formed by coagulation of small soot particles, consistent with previous findings [14]. The correlation between N_p and d_p can be described by an exponential function: $N_p(d_p) = a \times {d_p}^b$. A reference exponential function, which is calculated from the PDF at x/d = 132 and $R = 0.5W_f$, was plotted against experimental data in all subfigures in Fig. 12, to identify the trend of the PDFs for d_p > 12 nm. Figure 13 presents the fitting coefficient, b, here denoted K_{Nd}, for selected axial and radial locations. It can be found that the value of K_{Nd} increases with flame heights at all three selected radial locations, i.e. the decrease in N_p with the increase of d_p decreases at downstream locations when compared to upstream locations, as shown in Fig. 13a. The decrease in N_p with the increase in d_p decreases from the centreline of the flame towards the flame edge at x/d = 105 and x/d = 132, as shown in Fig. 13b. At the flame tip, the decrease rate of N_p with the increase of d_p is almost same for all selected radial locations.

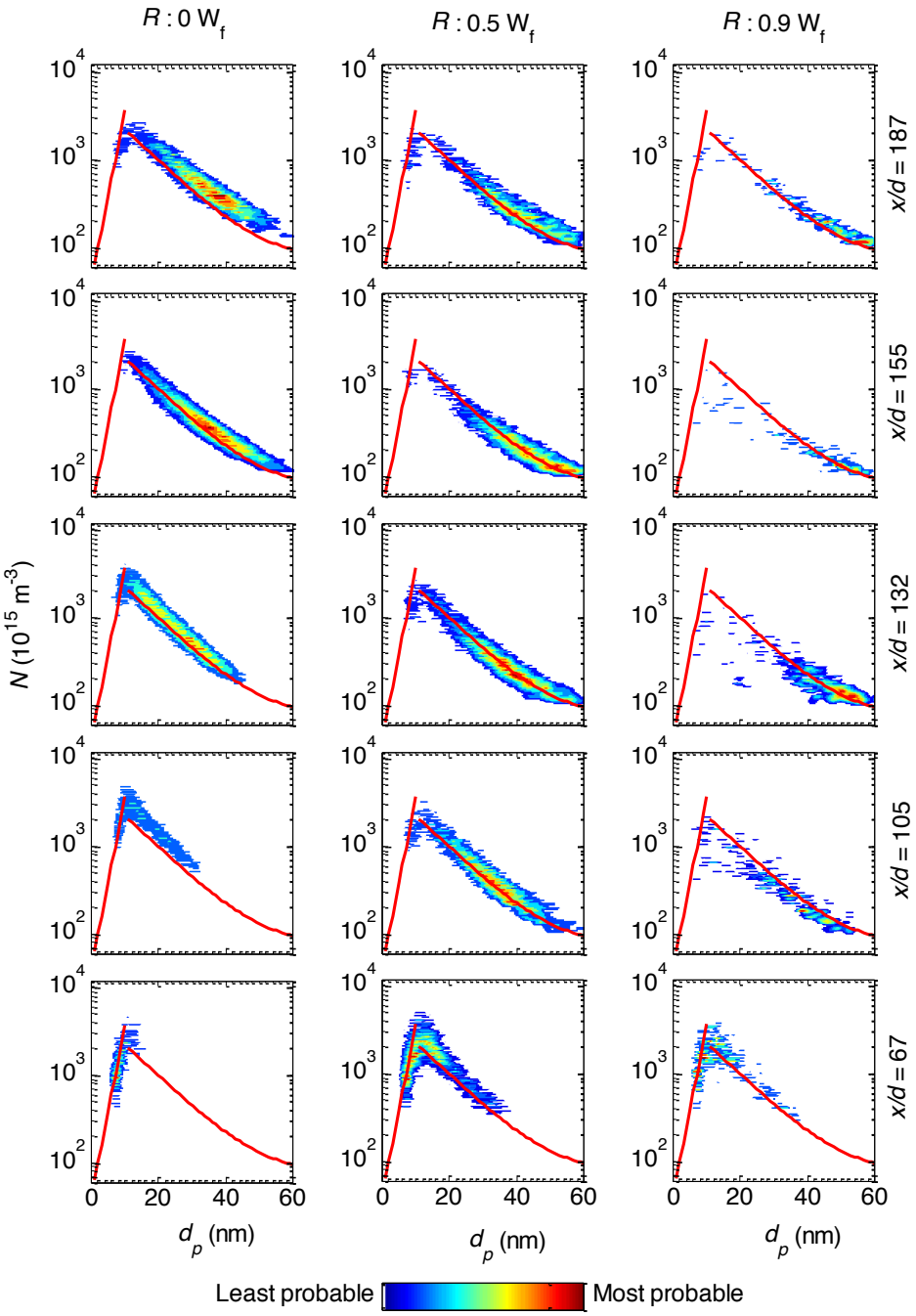

Figure 12: Joint PDFs of N_p and d_p at selected axial and radial locations. Statistics were calculated from 499 image-sets over an area of 5 (radial) × 3 (axial) mm^2, i.e. 15 × 9 neighbouring points (with each point binned from 5 × 5 pixels). The red line corresponds to a reference exponential-law function fitted from experimental data.

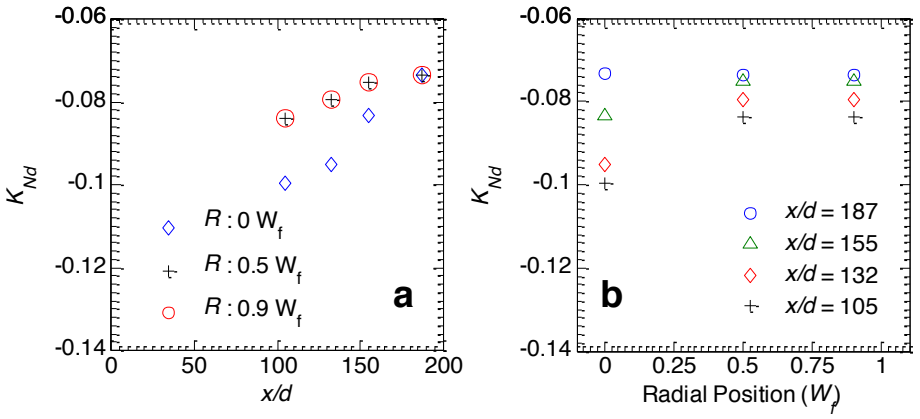

Figure 13: Coefficients of the fitted exponential function for experimental data between N and d_p, along (a) the axial and (b) radial direction.

4. Conclusion

The current simultaneous measurements of T, f_v, d_p and N_p with the nTLAF and TiRe-LII techniques yield generally very good agreement with previous measurements of T and f_v in a well-characterised turbulent ethylene sooting flame obtained using CARS and LII [16] and also provide significant new insight. The most probable temperature matches previous measurements to within 30 K while the mean temperatures agree well at those locations where the more than 90% of the data are within the detection limit. A criterion has also been determined that enables unambiguous determination of where unconditional statistics obtained with nTLAF are reliable, which is where the upper-bound and lower-bound calculations of the mean temperature converge. For the present flame, this condition applies for most of the central region of the flame. The PDF of the temperature measurements also agree well for the nTLAF and CARS measurements where the spatial resolution is similar. However, the desirability of further increasing both the spatial resolution and signal-to-noise ratio was highlighted, with the measurements being sensitive to these parameters.

The key findings of the joint PDFs of T, f_v, d_p and N_p from the present work are as follows:

1. The joint PDF of T and f_v reveals a significant dependence on radial distance near to the base of the flame, beyond which the dependence is mainly on axial distance. This finding is broadly consistent with previous findings [17].

2. Both the qualitative trends and quantitative values of the joint PDF of T and f_v appear to be consistent with previous independent optical measurements [10], given the differences in the flames and measurement techniques. It was found soot is typically formed between 1400 and 2000 K with the peak f_v occurring between 1550 and 1750 K on the axis.

3. In the joint PDFs of T and f_v, the value of T at the most probable f_v was found to increase along the axis from one fourth to three quarter of the flame, while the most probable f_v at these locations was found to be $\sim 0.05 \pm 0.04$ ppm and three to five times lower than the mean f_v values. The distribution of temperature in is widest at the most probable value of f_v values and is widest at the middle of the flame where f_v peaks.

4. A strong correlation was found between d_p and f_v for all selected flame locations and this relationship can be well described by a power-law function that varies little throughout the flame. Nevertheless, the distribution range of d_p increases significantly with both radial and axial distance, particularly the latter. The most probable d_p is between 8 and 18 nm and the corresponding most probable f_v is between 0.1 and 0.5 ppm. Soot particles with $d_p > 30$ nm mostly corresponds to $f_v > 1$ ppm.

5. The joint PDFs between T and d_p reveals that the small soot particles distribute in a wider temperature range than the larger soot particles. The large soot particles are found at relatively low temperatures.

6. A strong correlation was found between N_p and T, which relies on both radial and axial distance in the flame. The most probable N_p is between 10^{16} and 10^{17} m^{-3}, and is

decreasing from the flame axis towards the flame edge, while the corresponding most probable T varies with flame locations.

7. A strong correlation was found between N_p and f_v for all selected flame locations and this relationship varies little throughout the flame. The joint PDFs of N_p and f_v show that N_p increases exponentially with the increase of f_v for $f_v < 0.4$ ppm and then decreases exponentially when f_v exceeds 0.4 ppm, with a maximum value of $N_p \sim 5.0 \times 10^{17}$ m^{-3}.

8. A strong correlation was also found between N_p and d_p for all selected flame locations and this relationship varies little throughout the flame. In the joint PDFs of N_p and d_p, It was also found that N_p increases exponentially with the increase of d_p for $d_p < 12$ nm and decreases exponentially for $d_p > 12$ nm.

5. Acknowledgments

The support of the Australian Research Council is gratefully acknowledged through its Discovery and LIEF scheme. The authors also thank Mr. Kae Ken Foo for his help in the experiment. We also acknowledge Dr. Geigle and Dr. Köhler from the DLR, for their willing cooperation in providing detailed information of the geometry of their burner.

6. References

[1] T.C. Bond, S.J. Doherty, D. Fahey, P. Forster, T. Berntsen, B. DeAngelo, M. Flanner, S. Ghan, B. Kärcher, D. Koch, Bounding the role of black carbon in the climate system: A scientific assessment, J. Geophys. Res. 118 (2013) 5380-5552.
[2] C. de Haar, I. Hassing, M. Bol, R. Bleumink, R. Pieters, Ultrafine carbon black particles cause early airway inflammation and have adjuvant activity in a mouse allergic airway disease model, Toxicol. Sci 87 (2005) 409-418.
[3] M.R. Heal, P. Kumar, R.M. Harrison, Particles, air quality, policy and health, Chem. Soc. Rev. 41 (2012) 6606-6630.
[4] R.L. Vander Wal, LIF-LII measurements in a turbulent gas-jet flame, Exp. Fluids 23 (1997) 281-287.
[5] S.-Y. Lee, S.R. Turns, R.J. Santoro, Measurements of soot, OH, and PAH concentrations in turbulent ethylene/air jet flames, Combust. Flame 156 (2009) 2264-2275.
[6] V. Narayanaswamy, N. Clemens, Simultaneous LII and PIV measurements in the soot formation region of turbulent non-premixed jet flames, Proc. Combust. Inst. 34 (2013) 1455-1463.
[7] A. Coppalle, D. Joyeux, Temperature and soot volume fraction in turbulent diffusion flames: measurements of mean and fluctuating values, Combust. Flame 96 (1994) 275-285.
[8] C.R. Shaddix, J. Zhang, W. Scheffer, J. Doom, J.C. Oefelein, S. Kook, L.M. Pickett, H. Wang, Understanding and predicting soot generation in turbulent non-premixed jet flames, Sandia Report 2010-7178, (2010).
[9] Y. Sivathanu, G.M. Faeth, Temperature/soot volume fraction correlations in the fuel-rich region of buoyant turbulent diffusion flames, Combust. Flame 81 (1990) 150-165.

[10] C.R. Shaddix, J. Zhang. Joint temperature-volume fraction statistics of soot in turbulent non-premixed jet flames, Proceedings of the 8th US Combustion Meeting (2013)
[11] L. Gritzo, Y. Sivathanu, W. Gill, Transient Measurements of Radiative Properties, Soot Volume Fraction and Soot Temperature in a Large Pool Fire, Combust. Sci. Technol. 139 (1998) 113-136.
[12] J.J. Murphy, C.R. Shaddix, Soot property measurements in a two-meter diameter JP-8 pool fire, Combust. Sci. Technol. 178 (2006) 865-894.
[13] H. Bockhorn, H. Geitlinger, B. Jungfleisch, T. Lehre, A. Schön, T. Streibel, R. Suntz, Progress in characterization of soot formation by optical methods, Phys. Chem. Chem. Phys. 4 (2002) 3780-3793.
[14] H. Geitlinger, T. Streibel, R. Suntz, H. Bockhorn, Twenty-Seventh Sysposium (International) on Combustion Volume OneTwo-dimensional imaging of soot volume fractions, particle number densities, and particle radii in laminar and turbulent diffusion flames, Symp. (Int.) Combust. 27 (1998) 1613-1621.
[15] G.J. Nathan, P.A.M. Kalt, Z.T. Alwahabi, B.B. Dally, P.R. Medwell, Q.N. Chan, Recent advances in the measurement of strongly radiating, turbulent reacting flows, Prog. Energy Combust. Sci. 38 (2012) 41-61.
[16] M. Köhler, K. Geigle, W. Meier, B. Crosland, K. Thomson, G. Smallwood, Sooting turbulent jet flame: characterization and quantitative soot measurements, Appl. Phys. B 104 (2011) 409-425.
[17] S.M. Mahmoud, G.J. Nathan, P.R. Medwell, B.B. Dally, Z.T. Alwahabi, Simultaneous planar measurements of temperature and soot volume fraction in a turbulent non-premixed jet flame, Proc. Combust. Inst. 35 (2015) 1931-1938.
[18] N. Qamar, Z. Alwahabi, Q. Chan, G. Nathan, D. Roekaerts, K. King, Soot volume fraction in a piloted turbulent jet non-premixed flame of natural gas, Combust. Flame 156 (2009) 1339-1347.
[19] J. Zhang, C.R. Shaddix, R.W. Schefer, Design of "model-friendly" turbulent non-premixed jet burners for C2+ hydrocarbon fuels, Rev. Sci. Instrum 82 (2011) 074101.
[20] M. Köhler, K.-P. Geigle, T. Blacha, P. Gerlinger, W. Meier, Experimental characterization and numerical simulation of a sooting lifted turbulent jet diffusion flame, Combust. Flame 159 (2012) 2620-2635.
[21] R.S. Barlow, Laser diagnostics and their interplay with computations to understand turbulent combustion, Proc. Combust. Inst. 31 (2007) 49-75.
[22] M. Di Domenico, P. Gerlinger, M. Aigner, Development and validation of a new soot formation model for gas turbine combustor simulations, Combust. Flame 157 (2010) 246-258.
[23] Q.N. Chan, P.R. Medwell, P.A. Kalt, Z.T. Alwahabi, B.B. Dally, G.J. Nathan, Simultaneous imaging of temperature and soot volume fraction, Proc. Combust. Inst. 33 (2011) 791-798.
[24] B. Axelsson, R. Collin, P.-E. Bengtsson, Laser-induced incandescence for soot particle size and volume fraction measurements using on-line extinction calibration, Appl. Phys. B 72 (2001) 367-372.
[25] R. Hadef, K.P. Geigle, J. Zerbs, R.A. Sawchuk, D.R. Snelling, The concept of 2D gated imaging for particle sizing in a laminar diffusion flame, Appl. Phys. B 112 (2013) 395-408.
[26] B. Hu, B. Yang, U.O. Koylu, Soot measurements at the axis of an ethylene/air non-premixed turbulent jet flame, Combust. Flame 134 (2003) 93-106.
[27] Ü.Ö. Köylü, C.S. McEnally, D.E. Rosner, L.D. Pfefferle, Simultaneous measurements of soot volume fraction and particle size/microstructure in flames using a thermophoretic sampling technique, Combust. Flame 110 (1997) 494-507.
[28] H. Oltmann, J. Reimann, S. Will, Single-shot measurement of soot aggregate sizes by wide-angle light scattering (WALS), Appl. Phys. B 106 (2012) 171-183.
[29] E. Cenker, K. Kondo, G. Bruneaux, T. Dreier, T. Aizawa, C. Schulz, Assessment of soot particle-size imaging with LII at Diesel engine conditions, Appl. Phys. B 119 (2015) 765-776.
[30] Z.W. Sun, D.H. Gu, G.J Nathan, Z.T. Alwahabi, B.B. Dally, Single-shot, Time-Resolved planar Laser-Induced Incandescence (TiRe-LII) for soot primary particle sizing in flames, Proc. Combust. Inst. 35 (2015) 3673-3680.
[31] P.R. Medwell, Q.N. Chan, P.A. Kalt, Z.T. Alwahabi, B.B. Dally, G.J. Nathan, Development of temperature imaging using two-line atomic fluorescence, Appl. Opt 48 (2009) 1237-1248.
[32] Q.N. Chan, P.R. Medwell, B.B. Dally, Z.T. Alwahabi, G.J. Nathan, New seeding methodology for gas concentration measurements, Appl. Spectrosc. 66 (2012) 803-809.
[33] D.H. Gu, Z.W. Sun, P.R. Medwell, Z.T. Alwahabi, B.B. Dally, G.J. Nathan, Mechanism for laser-induced fluorescence signal generation in a nanoparticle-seeded flow for planar flame thermometry, Appl. Phys. B 2 (2015) 209-218.
[34] D.H. Gu, Z.W. Sun, G.J. Nathan, P.R. Medwell, Z.T. Alwahabi, B.B. Dally, Improvement of precision and accuracy of temperature imaging in sooting flames using two-line atomic fluorescence (TLAF), Combust. Flame 167 (2015) 481-493.
[35] C. Schulz, B.F. Kock, M. Hofmann, H. Michelsen, S. Will, B. Bougie, R. Suntz, G. Smallwood, Laser-induced incandescence: recent trends and current questions, Appl. Phys. B 83 (2006) 333-354.
[36] H. Bladh, J. Johnsson, P.-E. Bengtsson, On the dependence of the laser-induced incandescence (LII) signal on soot volume fraction for variations in particle size, Appl. Phys. B 90 (2008) 109-125.
[37] S. Schraml, S. Dankers, K. Bader, S. Will, A. Leipertz, Soot temperature measurements and implications for time-resolved laser-induced incandescence (TIRE-LII), Combust. Flame 120 (2000) 439-450.
[38] J.E. Sansonetti, W. Martin, Handbook of basic atomic spectroscopic data, J. Phys. Chem. Ref. Data 34 (2005) 1559-2259.

[39] J. Engström, J. Nygren, M. Aldén, C. Kaminski, Two-line atomic fluorescence as a temperature probe for highly sooting flames, Opt. Lett 25 (2000) 1469-1471.
[40] Z.W. Sun, Z.T. Alwahabi, D.H. Gu, S.M. Mahmoud, G.J. Nathan, B.B. Dally, Planar laser-induced incandescence of turbulent sooting flames: the influence of beam steering and signal trapping, Appl. Phys. B 119 (2015) 731-743.
[41] J. Zerbs, K. Geigle, O. Lammel, J. Hader, R. Stirn, R. Hadef, W. Meier, The influence of wavelength in extinction measurements and beam steering in laser-induced incandescence measurements in sooting flames, Appl. Phys. B 96 (2009) 683-694.
[42] C.J. Dasch, D.M. Heffelfinger, Planar imaging of soot formation in turbulent ethylene diffusion flames: fluctuations and integral scales, Combust. Flame 85 (1991) 389-402.
[43] K. Netzell, H. Lehtiniemi, F. Mauss, Calculating the soot particle size distribution function in turbulent diffusion flames using a sectional method, Proc. Combust. Inst. 31 (2007) 667-674.

Chapter 6

Optical thermometry for sooting flames under high-flux irradiation

Statement of Authorship

Title of Paper	Optical thermometry for steady sooting flames under high-flux irradiation
Publication Status	☐ Published ☐ Accepted for Publication ☑ Submitted for Publication ☐ Unpublished and Unsubmitted w ork w ritten in manuscript style
Publication Details	Applied Physics B: Lasers and Optics

Principal Author

Name of Principal Author (Candidate)	Dahe Gu
Contribution to the Paper	Under supervision of G. J. Nathan, Z. W. Sun, P. R. Medwell, Z. T. Alwahabi and B. B. Dally, I developed experimental methods, performed experiments, analysed data and wrote the manuscript.
Overall percentage (%)	55%
Certification:	This paper reports on original research I conducted during the period of my Higher Degree by Research candidature and is not subject to any obligations or contractual agreements with a third party that would constrain its inclusion in this thesis. I am the primary author of this paper.
Signature	Date: 01/02/2016

Co-Author Contributions

By signing the Statement of Authorship, each author certifies that:

i. the candidate's stated contribution to the publication is accurate (as detailed above);

ii. permission is granted for the candidate in include the publication in the thesis; and

iii. the sum of all co-author contributions is equal to 100% less the candidate's stated contribution.

Name of Co-Author	Graham J. Nathan
Contribution to the Paper	I acted as principal supervisor for the Ph.D. candidate, Dahe Gu, aided in development of the experimental methods, revision of the manuscript and evaluation of the final manuscript. I give consent to Dahe Gu to present this paper for examination towards the Doctorate of
Signature	Date: 1/2/16.

Name of Co-Author	Paul R. Medwell
Contribution to the Paper	I acted as co-supervisor for the Ph.D. candidate, Dahe Gu, aided in revision of the manuscript and evaluation of the final manuscript. I give consent to Dahe Gu to present this paper for examination towards the Doctorate of Philosophy.
Signature	Date: 11-FEB-2016

Name of Co-Author	Zeyad T. Alwahabi
Contribution to the Paper	I acted as co-supervisor for the Ph.D. candidate, Dahe Gu, aided in revision of the manuscript and evaluation of the final manuscript. I give consent to Dahe Gu to present this paper for examination towards the Doctorate of Philosophy.
Signature	Date: Feb 11, 2016

Name of Co-Author	Bassam B. Dally
Contribution to the Paper	I acted as co-supervisor for the Ph.D. candidate, Dahe Gu, aided in revision of the manuscript and evaluation of the final manuscript. I give consent to Dahe Gu to present this paper for examination towards the Doctorate of Philosophy.
Signature	Date: 4-2-16

Name of Co-Author	Zhi Wei Sun
Contribution to the Paper	I am a postdoc, co-supervised the experiments, aided in development of the experimental methods, performing experiments, data analysis and results discussion, revision of the manuscript and evaluation of the final manuscript. I give consent to Dahe Gu to present this paper for examination towards the Doctorate of
Signature	Date: 11/02/2016

Name of Co-Author	Xue Dong
Contribution to the Paper	I am a fellow Ph.D. student, aided in performing the experiment and evaluation of the final manuscript. I give consent to Dahe Gu to present this paper for examination towards the Doctorate of Philosophy.
Signature	Date: 11/02/2016

Please cut and paste additional co-author panels here as required.

Optical thermometry for high temperature multiphase environments under high-flux irradiation

Dahe Gu[1,2,*], Zhiwei Sun[1,2], Graham J. Nathan[1,2], Xue Dong[1,3], Bassam B. Dally[1,2], Paul R. Medwell[1,2] and Zeyad T. Alwahabi[1,3]

[1]*Centre for Energy Technology, The University of Adelaide, S.A. 5005, Australia*
[2]*School of Mechanical Engineering, The University of Adelaide, S.A. 5005, Australia*
[3]*School of Chemical Engineering, The University of Adelaide, S.A. 5005, Australia*

**Email address*: dahe.gu@adelaide.edu.au

Abstract

A non-intrusive optical method to measure gas phase temperature in multiphase environments under high-flux, broad-band irradiation, relevant to conditions in high temperature solar reactors was developed and demonstrated. The high-flux irradiation with a peak flux of 450 kW/m^2 was provided by a 6 kW metal-halide lamp coupled with a reflector and two concentrators. An ethylene/air diffusion flame, which contains fine soot particles, was employed to provide a high temperature reacting flow (approximately 1800 K) with strong optical interference from fine particles under conditions of relevance to solar reactors. Under this environment, the proposed laser-based thermometry technique, line-wise two-line atomic fluorescence (TLAF) has been successfully demonstrated to measure flame temperature with good spatial resolution of ~ 1 mm. It was found that the measurement inaccuracy caused by the presence of particle and the high-flux external radiation is only 65 K at a typical flame temperature of ~ 1800 K, while the measurement precision is 38 K. Results reveal that the presence of high-flux irradiation increases the flame temperature by typically 50 - 100 K. This paper presents a thermometry technique that is suitable for temperature measurement within solar reactors, in particularly in hybrid solar-thermal receiver-combustor systems. The experimental setup, measurement methodology and data processing are discussed, followed by temperature results.

Keywords: *High-flux irradiation; multiphase flow; temperature; laser diagnostics.*

1. Introduction

The ultilisation of solar reactors to convert solar energy to chemical energy has been demonstrated to have potential for a wide range of applications, e.g. hydrogen production [1-4], metal production [5], upgrade and decarbonize fossil fuels [6, 7] and solar-combustion hybrid [8]. These devices usually feature a cavity-receiver configuration where concentrated solar energy is directed into a well-insulated enclosure through an aperture. Concentrated solar energy is used as the heat source to drive the high-temperature chemical reactions inside the reactors. Compared with conventional fossil-fuel based processes, these solar-driven processes offer greatly reduced CO_2 emissions for high temperature processing [9]. Despite the recent demonstrations of pilot-scale solar reactor plants [5, 10] and experimentally validated modeling of a 1MW design [11], these technologies still require further development and optimization for them to be economically and technically ready for large-scale commercial applications. However, few, if any, detailed and spatially resolved measurements of the distribution of important parameters such as temperature, which controls the chemical reaction rate, are available [1]. Hence there is a need for accurate and spatially resolved gas temperature measurements in solar reactors.

Gas temperature measurement in solar reactors, however, is very challenging because of the high temperature environment, the presence of high-flux irradiation and, in some cases, the presence of fine particles. Solar reactors operate at temperatures between 1600 and 2400 K [1-3, 11, 12], may also include fine particles with diameter ranging between 0.1 and 10 μm [1, 3, 13] and are subjected to a strong irradiation with flux ranging between 400 and 3500 kW/m^2 [3, 4, 12, 14]. These make accurate gas temperature measurement very difficult to perform, in particular spatially resolved measurements. The presence of fine particles and high-flux irradiation not only prevents the application of contact probes due to the direct exposure under irradiation and deposition of fine particles, but also hinders many optical methods due to the strong scattering. For these reasons, in previous studies, typically only the reactor wall surface temperature and the cavity nominal temperature were measured at several locations with the use of thermocouples [2, 3, 5, 12] and optical pyrometers [2, 3, 12]. However, the distribution of temperature is not homogeneous in the reactor's cavity and the temperature inside the cavity is not as same as the wall temperature [1, 12]. Hence there is a need for a thermometry technique that can provide spatially-resolved temperature measurements as well as being non-intrusive to the flow field inside the solar reactors.

Laser diagnostic tools that are usually employed in the combustion research field may offer solutions to these problems, owing to their non-intrusive nature and good spatial resolution in high temperature environments [15-18]. However, the total radiative power in a solar reactor is much greater than the natural radiation from a soot-free flame, and even an order of magnitude greater than that from a sooting flame [19]. This high radiation may hinder laser-based optical thermometry techniques, which are developed for combustion diagnostics, to be applied reliably. To the best of the authors' knowledge, only coherent anti-Stokes Raman spectroscopy (CARS) has been successfully demonstrated to measure the gas temperature in a solar receiver/reactor to study gas phase chemical reactions in high temperature environment [20]. However, this study has only been demonstrated in an environment without any particles and was limited to point measurement and hence resulted in a relatively poor spatial resolution. Therefore, in the present work, we propose another laser-based technique, i.e., two-line atomic fluorescence (TLAF) with seeded atomic indium as the tracer species, which has been shown to have good potential for two dimensional (2-D) temperature measurements in flames in the presence of fine particles [21-27].

In light of the above background, the present study aims to (1) demonstrate the application of TLAF in high-temperature environments with the presence of fine particles and high-flux external irradiation and (2) assess the precision and accuracy of the technique. The work also assesses the effect of high-flux irradiation on temperature of a typical diffusion sooting flame.

2. TLAF Thermometry

In TLAF measurements, the gas phase temperature is derived from the intensity ratio between the two laser-induced fluorescence (LIF) signals of the tracer (e.g. atomic indium) excited from two different lower states to a common upper state. The population of the two lower states, hence the LIF signals, are related to the environment temperature according to the Boltzmann distribution law [28]. The gas temperature, *T*, can be calculated using the following equation,

$$T = \frac{\Delta E_{10}/k}{\ln\left(\frac{S_{21}}{S_{20}}\right) - \ln\left(\frac{F_{21}(E_{02})}{F_{20}(E_{12})}\right) + C_t}. \qquad (1)$$

Here the subscripts *0* and *1* denote the two lower electronic energy levels while *2* denote the upper energy level. S is the collected LIF signal intensity, E is the laser spectral power density, ΔE_{10} is the difference in energy between electronic levels in [cm^{-1}] and has a value of 2212.599 cm^{-1} for atomic indium [29], and k is the Boltzmann constant. The system-dependent dimensionless calibration constant, C_t, is dependent on a number of experimental factors such as solid angle of signal collection and collection efficiency of detector. The value of C_t needs to be experimentally determined through a calibration process, which is generally performed in a particle-free steady flame, where the temperature can be measured with a thermocouple. The term of *F(E)* in Eq. (1) is used to correct for laser power variations during TLAF measurements, where F is the function of LIF signals dependent on the laser power E. The function F can be a linear function (i.e. for TLAF operating in the linear regime) [22, 30], a non-linear function (i.e. the non-linear TLAF) [26] and even a constant (i.e. saturation TLAF) [25]. The F function also needs to be determined in experiments. TLAF thermometry using atomic indium as tracer species is suitable for temperature measurements between 800 and 2800 K, which is well-matched with the temperature inside the solar reactors.

3. Experimental Details

3.1 TLAF setup

Figure 1 presents a schematic diagram of the TLAF arrangement. Two Nd:YAG pumped dye lasers (Quantel, TDL 90) were employed to produce laser beams centred at 410.18 nm and 451.13 nm, respectively. Atomic indium in the flame was then excited to the same upper state ($6^2S_{1/2}$) from two lower states ($5^2P_{1/2}$ and $5^2P_{3/2}$). The laser pulse energies were kept at 1.0 μJ/pulse and 2.8 μJ/pulse, respectively. The two laser beams with a ~ 120 ns temporal separation were first combined using a dichroic mirror (Thorlabs, DMLP425) and then focused into round laser beams using a spherical lens (f = 1000 mm). The combined laser beams were directed through the centre of the burner and propagated at an angle of 30° relative to the central axis of the solar simulator. An aperture was placed 20 mm from the outer edge of the burner to reject stray light from the incident laser beams. The laser energy was monitored by recording laser beams reflected by a glass plate using a fast photomultiplier tube (PMT) coupled with a 2 GHz oscilloscope (LeCroy, 204MXi-A).

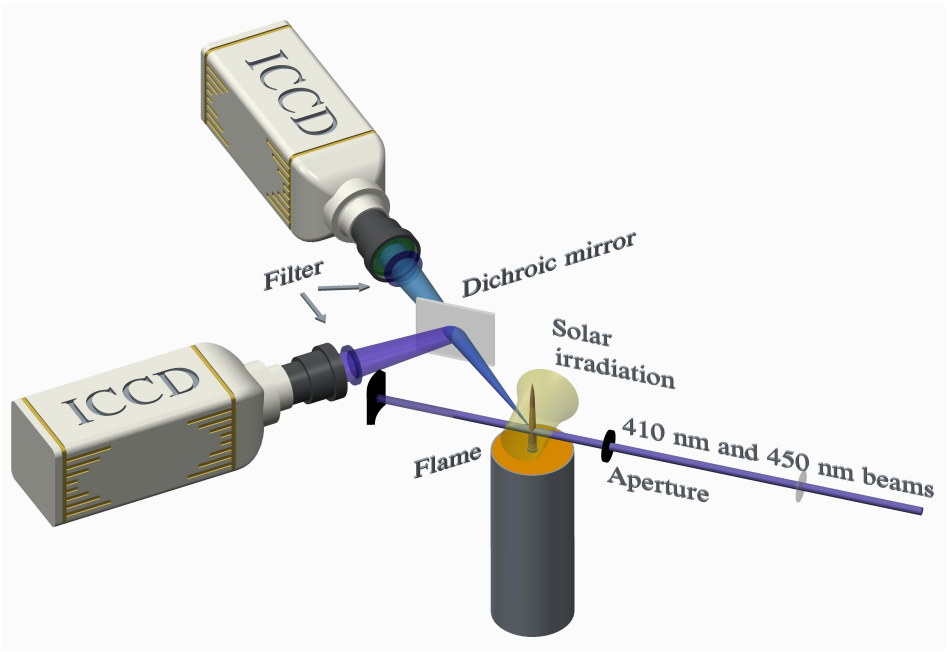

Figure 1: Schematic diagram of the experimental arrangement for the TLAF measurement. The Santoro-type flame and the focal zone of the simulated solar irradiation are also shown.

The two LIF signals were imaged using two intensified CCD (ICCD) cameras (Princeton Instruments, PI-MAX II) mounted with standard Nikon *f*/1.4 lenses (f = 50 mm). Two custom-made narrow-band filters (Alluxa) with a full width at half maximum (FWHM) of ~ 1.2 nm, a peak transmission of 95% and a high optical density (OD) of ~ 6.0 at the excitation laser wavelengths were used for fluorescence signals collection at 451.13 nm ($6^2S_{1/2} \rightarrow 5^2S_{3/2}$ transition, the Stokes signal) and 410.18 nm ($6^2S_{1/2} \rightarrow 5^2S_{1/2}$ transition, the anti-Stokes signal). A dichroic mirror (Thorlabs, DMLP425) was placed in front of the two cameras to allow spectral separation of two LIF signals and that of the elastic laser scattering (ELS) signal from the corresponding LIF signal. The gate width of both cameras was kept at 30 ns. The lasers, cameras and the oscilloscope were synchronized using a digital delay/pulse generator (Stanford, DG535). All LIF images were accumulated from 200 instantaneous shots to enhance the SNR and to allow temporal-dependent light scattering background to be accounted for (more details are discussed below). The TLAF laser beams were passed through the central axis of the flame and translated in the axial direction to measure radial profiles of flame temperature at various flame heights.

In all data processing, the LIF radial profiles were acquired by integrating the LIF signal intensity over an axial distance where the intensity had dropped to ~ 12% of the peak intensity value. The resultant

spatial resolution of line-wise temperature measurement was 0.95 mm. It should be noted that this demonstrated technique is also capable for planar temperature imaging, where the laser energy profile correction needs to be performed. However, to avoid the uncertainty associated with the out-of-plane fluorescence from atomic indium generated by secondary, scattered excitation from soot up-beam in the flame, line-wise configuration was chosen.

3.2 Burner and flames

A laminar ethylene/air diffusion sooting flame burned on a Santoro-type burner was selected to provide a high temperature, particle-laden environment. The burner consists of two concentric brass tubes with inner diameters of 10.5 mm and 97.7 mm, respectively. The central tube surface extends 4 mm above the surface of the annular air co-flow tube. A series of wire meshes and glass beads at the bottom of the burner, together with a stainless steel honeycomb at the final stage were used to condition the flows of fuel and co-flowing gases. Gaseous fuel, C_2H_4, was passed through the central tube at a flow rate of 0.184 standard liters per minute (L/min) or 0.0322 m/s. Co-flowing air was delivered through the annular co-flow passage at a flow rate of 127.7 L/min or 0.288 m/s. The visible flame height (L_f) was 64 mm. All temperature measurements were carried out in this sooting flame, in which the peak volume fraction of soot is ~ 10 ppm without the irradiation and ~ 16 ppm under the irradiation [31].

A soot-free, premixed C_2H_4/air flame was employed for calibrations of the value of C_t and the function of F (see Eq. (1)). The flow rates were 0.53 L/min for the C_2H_4 fuel, and 3.91 L/min and 127.7 L/min for the premixed air and co-flow air stream, respectively. The calibrations were performed in the product zone in the flame with a uniform temperature of 1,840 K, as measured by an *R*-type Pt/Pt-Rh 13% thermocouple with a wire diameter of 75 μm (Omega, P13R-003). A temperature correction of 61 K was added to the raw measurement to correct for radiation heat loss from the thermocouple.

3.3 Seeding arrangement

Indium nanoparticles was seeded into the flame with an in-house laser ablation system [32-34]. The fuel gas stream transports the indium nanoparticles from the ablation chamber into the flame. The nanoparticles undergo thermal decomposition within the flame to release indium atoms. The mass flow rate of the

nanoparticles seeding is approximately 160 μg/min, which results in a seeding concentration of a few parts per million (ppm). This seeding method offers the advantage of imposing minimal disturbance on the flame temperature and chemistry of the relatively small Santoro-type flame. This seeding method is therefore suitable for temperature measurement inside hybrid solar-thermal receiver-combustor where combustion is present. Alternative seeding method such as seeding droplets of dissolved indium salt solvent using a nebuliser [35] or seeding vapor phase tri-methyl-indium [36, 37] may also be employed.

3.4 Solar simulator

A 6 kW metal halide lamp (Osram, HMI 6000), with a 50 Hz single phase AC power supply, was employed as the light source to provide high-flux irradiation. The irradiation of the lamp oscillates at a frequency of 100 Hz. This lamp provides a good match in spectra with the solar resource [38]. An alumina and silica surface coated ellipsoidal reflector, with a focal length of 3000 mm, was close coupled to the lamp to concentrate the irradiation. The irradiation is further focused by co-aligning secondary and tertiary concentrators with the axis of the primary concentrator, following earlier work [38, 39], as shown in Fig. 2. The burner was placed at the focal plane between the secondary and the tertiary concentrators, with a distance of 50 mm from each. To ensure the burner and the flame were not influenced by radiant and convective heat transfer from the concentrators, both concentrators were water-cooled. Their surface temperature was less than 50 ºC, as measured by an infrared thermometer immediately after turning off the lamp.

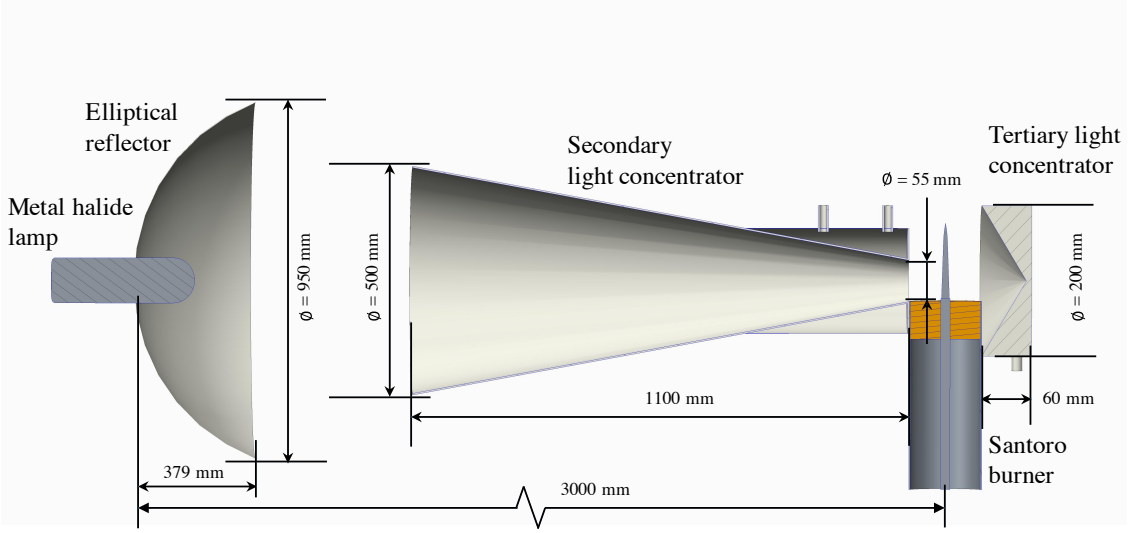

Figure 2: Schematic diagram of the experimental arrangement of the solar simulator and the flame. Note that the distance between the primary and secondary concentrators is truncated.

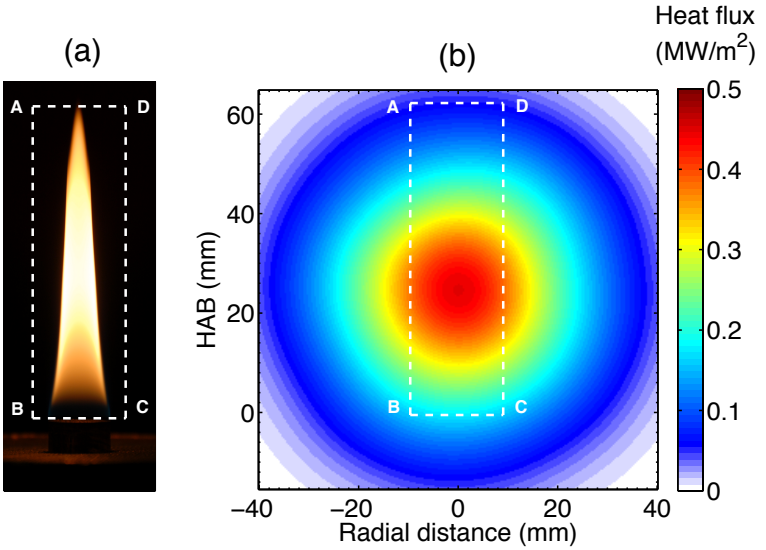

Figure 3: (a) Image of the natural flame luminosity from the sooting flame. (b) Radiative flux distribution at the focal plane of the solar simulator which is on the centreline of the flame. The flame's relative position on this plane is also shown with the square boxes.

The focal point of the solar simulator was positioned 23.5 mm above the burner. The cross section of the radiative flux distribution at the focal plane of the solar simulator, which is also on the centreline of the flame, is presented in Fig. 3b, as calculated with an experimentally validated Monte-Carlo ray tracing simulation [38]. The relative position of the flame to the irradiation at this plane is also shown as a location reference in Fig. 3. The maximum value of this heat flux was 450 kW/m^2 at a height above burner (HAB) of 23.5 mm, while its average within the flame region was 27 kW/m^2.

4. Processing Methodology

4.1 Correction for light scattering

Under irradiation from the high-flux solar simulator, strong and broadband light scattering was generated from the flame regions where soot is present. The scattering can cause a significant background to the LIF signals even though high-quality narrow-band filters were applied, hence resulting in a large measurement

uncertainty if no correction is applied. Since the flame is steady and the scattering from irradiated particles can be recorded in the absence of the TLAF laser beams, the scattering can then be removed by background subtraction from images recorded in the presence of the TLAF laser beams. In measurements, 200 instantaneous images were recorded at ~ 3 Hz and the averaged images were used for background subtraction and temperature derivation. The use of averaged images in data processing is not only because this approach can improve the signal-to-noise ratio of the data, but also because this approach can smoothen the fluctuation of the scattering due to the fact that the irradiation from the lamp oscillates at a frequency of 100 Hz in both intensity (± 30%) and spectrum [38]. The mismatch between the collection frequency and that lamp operation frequency as well as the number of images ensure that aliasing does not have any effect on our results.

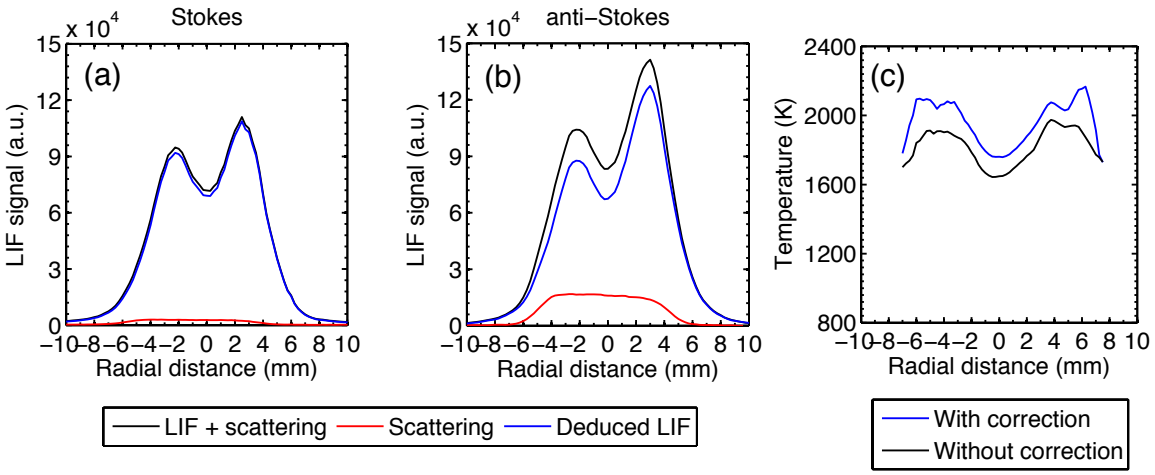

Figure 4: Radial profiles of the total laser-induced emission (black lines), background from scattered light (red lines) and the deduced radial profile of *pure* indium LIF signal (blue lines) obtained by subtraction. Data are shown for (a) the Stokes process and (b) the anti-Stokes process at a HAB of 42 mm. (c) Radial profiles of the temperature calculated from LIF signals without and with correction for scattered light background.

The correction for light scattering is necessary to derive accurate gas temperature. Figure 4 presents the averaged radial profiles of the Stokes (Fig. 4a) and anti-Stokes (Fig. 4b) LIF signals without and without light scattering background correction at a HAB = 42 mm in the flame, in which the laser beams enter from the left side. The asymmetry in the Stokes and anti-Stokes signals stems from the non-uniform seeding of

indium and does not affect the temperature measurements as the temperature is derived from the ratio of the two LIF signals. Figures 4a and 4b reveal the scattered irradiation causes significant interference to LIF signals. For example, the magnitude of the scattered irradiation is about 3% (Stokes) and 17% (anti-Stokes) of the total emission collected at radial distance of 3 mm, respectively. Such amount of interference, if not corrected for, can cause a large error in the derived temperature, as shown in Fig. 4c. Flame temperature can be underestimated by 100 - 250 K without scattered irradiation corrections. In addition, the temperature profile spans from the centerline to r = 8 mm because the lack of signal on the lean side of the reaction zone for r > 8 mm.

4.2 Calibration process

To obtain the calibration function F for the Stokes and anti-Stokes processes, calibration curves between the LIF signal and laser energy were obtained by recording the LIF signal at different laser energies. Figure 5 presents the calibration curves for the Stokes and anti-Stokes processes. Each measurement intensity was integrated over an area of 3.1 mm (14 pixels) × 1.1 mm (5 pixels) in the axial and radial directions, respectively, at HAB = 40 mm on the axis. Since the calibration curves were acquired from averaging 200 single shots rather than from single shots, the function for calibration curves is therefore not limited to the nTLAF equation. Two alternative calibration functions were assessed for both the Stokes and anti-Stokes processes, namely the nTLAF equation and a power-law function, as shown in Table 1. It can be seen that the power-law function yields the higher R-squared values than the nTLAF equation for both the Stokes and anti-Stokes processes. The power-law function was therefore used for the following temperature derivation.

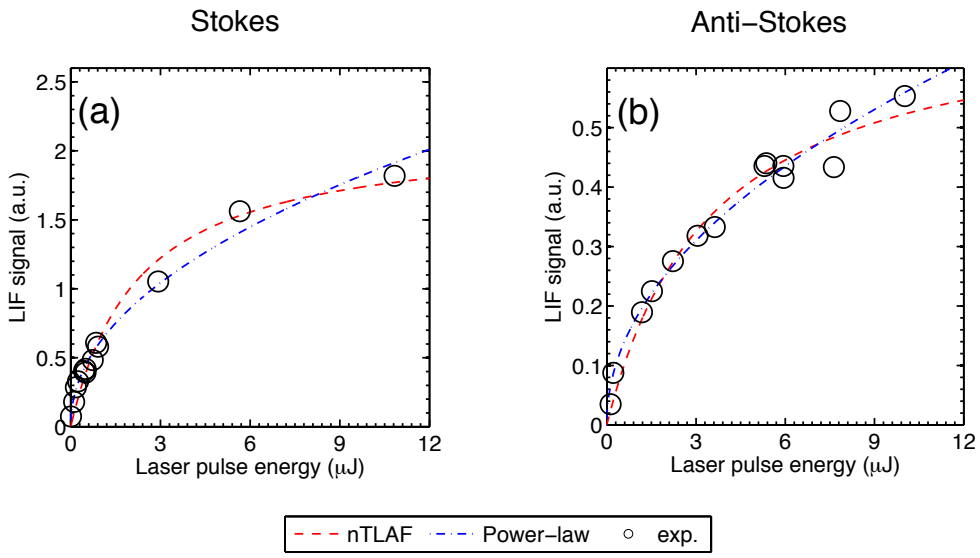

Figure 5: LIF signals (circles) as a function of laser energy for (a) the Stokes and (b) the anti-Stokes processes in TLAF measurements. Dashed lines presents the fitted curves derived from nTLAF and power law equations.

Table 1: Equations for fitting the calibration data (see Fig. 5) for the calibration constants.

Equation description	Equation format	R^2 value	
		Stokes	Anti-Stokes
nTLAF	$F(E) = \frac{aE}{(E+b)}$	0.9754	0.9702
Power-law	$F(E) = aE^b$	0.9873	0.9804

4.4 Measurement precision and accuracy

The precision of the measurement was assessed by calculating the statistics of flame temperature measured within the uniform temperature region in the soot-free calibration flame. Figure 6 presents the histogram of temperature values over an area of 3.1 mm (14 pixels) × 1.1 mm (5 pixels) at HAB = 40 mm on the flame axis. The standard deviation of the measured temperature is approximately ∼ 38 K, or 2.2%, about the mean value of 1857 K.

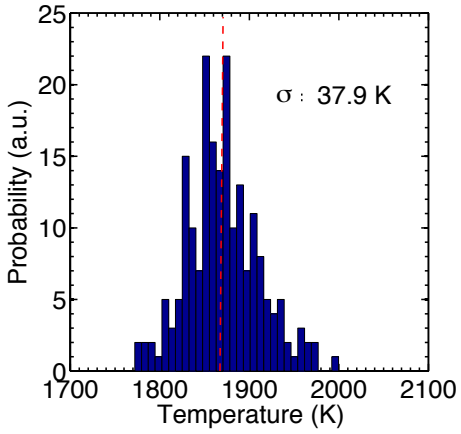

Figure 6: Probability distribution of temperature over an area of 3.1 mm (14 pixels) × 1.1 mm (5 pixels) with uniform temperature distribution at HAB = 40 mm on the axis. The red dashed lines indicate the mean value of temperature.

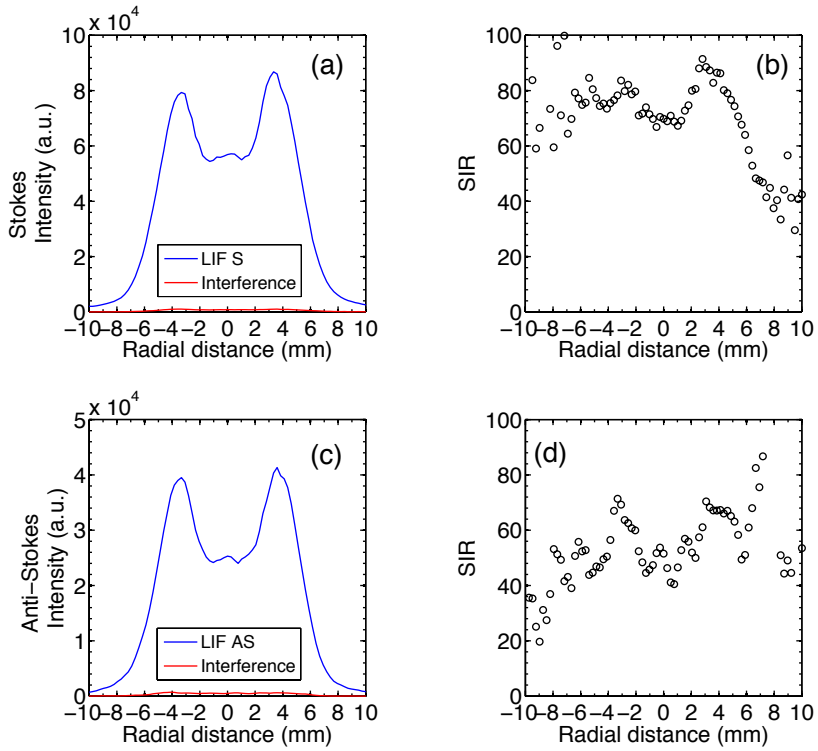

Figure 7: Radial profiles of the laser induced emission at HAB = 35 mm of the sooting flames acquired with off-resonant (*red lines*) and resonant (*blue lines*) excitations, respectively, for (*a*) the Stokes and (*c*) anti-Stokes processes. The corresponding ratios between blue line and red line are shown in (*b*) and (*d*), respectively.

The measurement accuracy of TLAF in sooting flames is mainly related to the uncertainty of temperature measured in the calibration flame and the laser-induced interferences in the sooting flame from particles and polycyclic aromatic hydrocarbons (PAH) [40]. The former uncertainty is directly related to the calibration method and the latter is more complex due to the non-uniform distribution of soot and PAH and their changes in the presence of the external irradiation [23]. The uncertainty associated with the calibration can be improved by employing a more accurate calibration method. Here, only the assessment of the accuracy affected by the spectral interference is presented. The amount of spectral intensity was measured with off-resonant laser excitation. Figure 7 presents the radial profiles of emission recorded with on- and off resonant laser excitations for Stokes (Fig. 7a) and anti-Stokes (Fig. 7c) processes. All results were averaged over 200 single shots and recorded at HAB = 35 mm in the absence of the external irradiation. It was found that the spectral interference from soot and PAH is very weak even with a peak soot volume fractions of ~ 10 ppm , attributing to the good blocking abilities of the filters and beam-splitter. Figure 7b and 7d present the resulting signal-interference ratio (SIR) for Stokes and anti-Stokes processes, respectively. The SIR spans from 60 to 80 in the region from r = -8 mm to r = 0 mm for the Stokes process and from 30 to 70 in the same region for the anti-Stokes process. For the radial position with the lowest SIR values, i.e. at the centreline, the SIR is 70 (Stokes) and 40 (anti-Stokes) and the resulting accuracy of the measurement due to the presence of interference has been estimated to be 45 K. In the presence of the solar irradiation, the spectral interference is expected to increase by 60% due to the increase of soot volume fraction by 60% (peak f_v ~ 16 ppm) [32], whereas the resultant uncertainty is estimated to be 65 K. It should be noted that the SIR can be enhanced by increasing the seeding concentration of indium and hence reducing the uncertainty from spectral interferences.

5. Temperature Results

Figure 8a presents the centreline temperature measured in the sooting flame with and without the high-flux irradiation, respectively. It can be seen that the flame temperature on the centreline increases with irradiation at all flame heights measured. This temperature increase is more clearly shown in Fig. 8b. The temperature increases more gradually with HAB from approximately zero at HAB = 9 mm to a maximum of ~ 100 K in the range of 26 mm < HAB < 41 mm and then decreases to a steady value of ~ 50 K close to the tip of the

flame. This trend of temperature increase along the flame centerline is generally consistent with the distribution of the irradiative flux (see Fig. 3), and it may also be relevant to the distribution of soot which is the primary species to absorb the external irradiation [31].

Figure 9 presents the measured radial profiles of temperature at five flame heights with and without the solar irradiation. At HAB = 12 mm, the two temperature profiles coincide over the range $0 < r < 5.5$ mm. However, the irradiated case has a maximum increase of ~ 150 K at $r = 6.5$ mm relative to the without irradiation case. The temperature profiles also converge at $r = 7.4$ mm where the temperature is 1356 K. At HAB = 26, 32 and 42 mm, the increase in temperature in the irradiated cases occurs throughout the entire radial profile. The maximum increase occurs at HAB = 32 mm, where the average increase across the entire radial profile is 242 K and the maximum increase is 332 K at $r = 4.5$ mm.

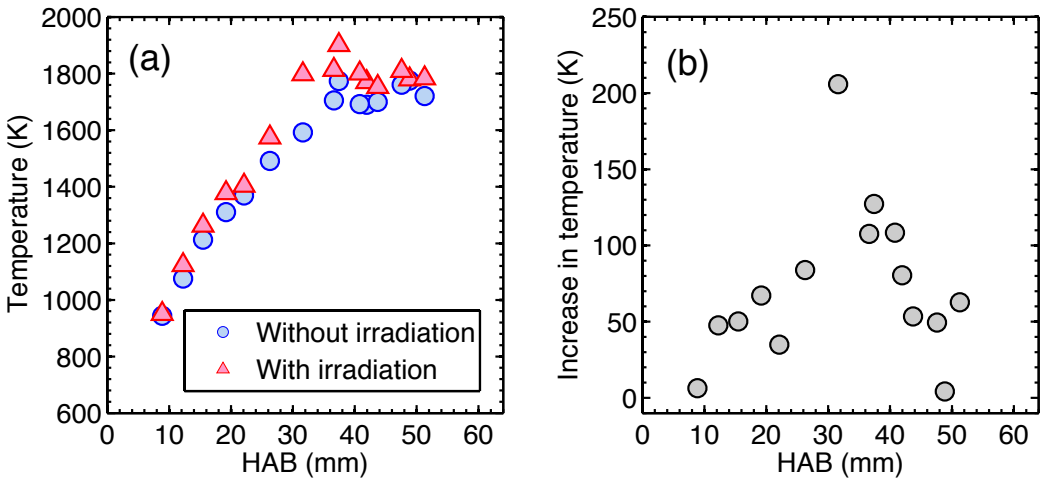

Figure 8: Temperature along the axis of the Santoro flame (a) with and without irradiation from the simulated solar irradiation; and (b) the difference between these two cases. The temperature was integrated over an axial width of 1.8 mm.

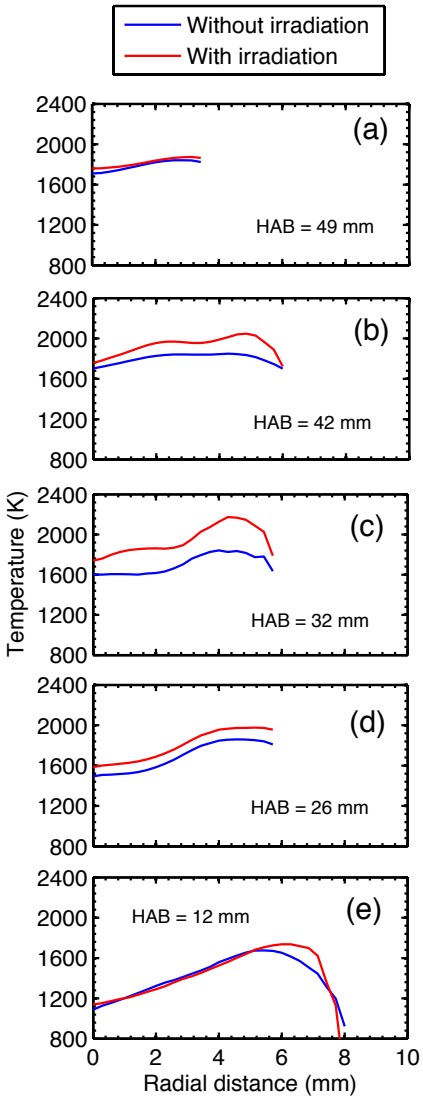

Figure 9: Radial profiles of temperature in a Santoro flame at various flame heights with and without irradiation from simulated solar light.

6. Conclusions

A one-dimensional TLAF technique has been developed to enable accurate gas phase temperature measurements in a particle-laden environment with the presence of high-flux external irradiation (a peak flux of 450 kW/m^2) that is relevant to solar reactors. The method to suppress scattering from the irradiated soot particles was described, which is the main interference to the TLAF signals, while the laser-induced interference from particles and other large molecules is negligible. It was found that the method with a measurement precision of 40 K and an accuracy of 65 K is reliable for gas phase temperature measurements in such a hostile environment.

The high-flux solar irradiation was also found to increase the flame temperature by up to ~ 100 K at heights between 2.5 to 4 diameters and by ~ 50 K elsewhere on the centreline. The radial profiles of temperature show similar trends. The increase in temperature in the flame is attributed to absorption of the simulated solar irradiation by soot particles, followed by heat transfer to the surrounding gases, and by gaseous species in the flame.

Acknowledgments

This work was funded by Australian Research Council Linkage under Project ID: LP110200060. Partial support for the work was also provided by the Australian Government through the Australian Renewable Energy Agency, ARENA Grant 1-US034.

References

1. Abanades S, Charvin P, Flamant G. Design and simulation of a solar chemical reactor for the thermal reduction of metal oxides: case study of zinc oxide dissociation. Chemical Engineering Science. 2007;62(22):6323-33.
2. Abanades S, Flamant G. Experimental study and modeling of a high-temperature solar chemical reactor for hydrogen production from methane cracking. International Journal of Hydrogen Energy. 2007;32(10):1508-15.
3. Hirsch D, Steinfeld A. Solar hydrogen production by thermal decomposition of natural gas using a vortex-flow reactor. International Journal of Hydrogen Energy. 2004;29(1):47-55.
4. Moller S, Palumbo R. The development of a solar chemical reactor for the direct thermal dissociation of zinc oxide. Journal of Solar Energy Engineering. 2001;123(2):83-90.
5. Wieckert C, Frommherz U, Kräupl S, Guillot E, Olalde G, Epstein M, et al. A 300kW solar chemical pilot plant for the carbothermic production of Zinc. Journal of Solar Energy Engineering. 2007;129(2):190-6.
6. Piatkowski N, Wieckert C, Weimer AW, Steinfeld A. Solar-driven gasification of carbonaceous feedstock—a review. Energy & Environmental Science. 2011;4(1):73-82.
7. Steinberg M. Fossil fuel decarbonization technology for mitigating global warming. International Journal of Hydrogen Energy. 1999;24(8):771-7.
8. Nathan G, Battye D, Ashman P. Economic evaluation of a novel fuel-saver hybrid combining a solar receiver with a combustor for a solar power tower. Applied Energy. 2014;113(0):1235-43.
9. Steinfeld A, Palumbo R. Solar thermochemical process technology. Encyclopedia of physical science and technology. 2001;15(1):237-56.
10. Piatkowski N. Solar driven steam gasification of carbonaceous feedstocks: Feedstock characterization to pilot facility testing. Ph.D. thesis, ETH Zurich; 2011.
11. Schunk L, Lipiński W, Steinfeld A. Heat transfer model of a solar receiver-reactor for the thermal dissociation of ZnO—Experimental validation at 10kW and scale-up to 1MW. Chemical Engineering Journal. 2009;150(2):502-8.
12. Müller R, Lipiński W, Steinfeld A. Transient heat transfer in a directly-irradiated solar chemical reactor for the thermal dissociation of ZnO. Applied Thermal Engineering. 2008;28(5):524-31.
13. Melchior T, Steinfeld A. Radiative transfer within a cylindrical cavity with diffusely/specularly reflecting inner walls containing an array of tubular absorbers. Journal of Solar Energy Engineering. 2008;130(2):021013.
14. Piatkowski N, Steinfeld A. Solar-driven coal gasification in a thermally irradiated packed-bed reactor. Energy & Fuels. 2008;22(3):2043-52.
15. Aldén M, Bood J, Li Z, Richter M. Visualization and understanding of combustion processes using spatially and temporally resolved laser diagnostic techniques. Proceedings of the Combustion Institute. 2011;33(1):69-97.
16. Barlow R. Laser diagnostics and their interplay with computations to understand turbulent combustion. Proceedings of the Combustion Institute. 2007;31(1):49-75.
17. Daily J. Laser induced fluorescence spectroscopy in flames. Progress in Energy and Combustion Science. 1997;23(2):133-99.
18. Nathan G, Kalt P, Alwahabi Z, Dally B, Medwell P, Chan Q. Recent advances in the measurement of strongly radiating, turbulent reacting flows. Progress in Energy and Combustion Science. 2012;38(1):41-61.

19. Dong X, Nathan G, Mahmoud S, Ashman P, Gu D, Dally B. Global characteristics of non-premixed jet flames of hydrogen–hydrocarbon blended fuels. Combustion and Flame. 2015;162(4):1326-35.
20. Steinfeld A, Bombach R, Haueter P, Hemmerling B, Kreutner W, Thompson G. Experimental setup of a laser diagnostics system for a high-temperature solar receiver/reactor. Journal of Solar Energy Engineering. 1994;116(4):206-11.
21. Chan Q, Medwell P, Kalt P, Alwahabi Z, Dally B, Nathan G. Simultaneous imaging of temperature and soot volume fraction. Proceedings of the Combustion Institute. 2011;33(1):791-8.
22. Engström J, Nygren J, Aldén M, Kaminski C. Two-line atomic fluorescence as a temperature probe for highly sooting flames. Optics Letters. 2000;25(19):1469-71.
23. Gu D, Sun Z, Nathan G, Medwell P, Alwahabi Z, Dally B. Improvement of precision and accuracy of temperature imaging in sooting flames using two-line atomic fluorescence (TLAF). Combustion and Flame. 2015;167:481-93.
24. Kaminski C, Engström J, Aldén M. Quasi-instantaneous two-dimensional temperature measurements in a spark ignition engine using 2-line atomic fluorescence. Proceedings of the Combustion Institute. 1998;27(1):85-93.
25. Manteghi A, Shoshin Y, Dam N, de Goey L. Two-line atomic fluorescence thermometry in the saturation regime. Applied Physics B. 2015;118(2):281-93.
26. Medwell PR, Chan Q, Dally B, Mahmoud S, Alwahabi Z, Nathan G. Temperature measurements in turbulent non-premixed flames by two-line atomic fluorescence. Proceedings of the Combustion Institute. 2013;34(2):3619-27.
27. Nguyen Q, Dibble R, Carter C, Fiechtner G, Barlow R. Raman-LIF measurements of temperature, major species, OH, and NO in a methane-air bunsen flame. Combustion and Flame. 1996;105(4):499-510.
28. Medwell P, Chan Q, Kalt P, Alwahabi Z, Dally B, Nathan G. Development of temperature imaging using two-line atomic fluorescence. Applied Optics. 2009;48(6):1237-48.
29. Sansonetti J, Martin W. Handbook of basic atomic spectroscopic data. J Phys Chem Ref Data. 2005;34(4):1559-2259.
30. Nygren J, Engström J, Walewski J, Kaminski C, Aldén M. Applications and evaluation of two-line atomic LIF thermometry in sooting combustion environments. Measurement Science and Technology. 2001;12(8):1294.
31. Dong X, Sun Z, Gu D, Ashman P, Alwahabi Z, Dally B, Nathan G. The influence of high flux broadband irradiation on soot concentration and temperature of a sooty flame. Combustion and Flame. 2016:accepted 24 May 2016.
32. Chan Q, Medwell P, Dally B, Alwahabi Z, Nathan G. New seeding methodology for gas concentration measurements. Applied spectroscopy. 2012;66(7):803-9.
33. Gu D, Sun Z, Medwell P, Alwahabi Z, Dally B, Nathan G. Mechanism for laser-induced fluorescence signal generation in a nanoparticle-seeded flow for planar flame thermometry. Applied Physics B. 2015;2(118):209-18.
34. Medwell P, Chan Q, Dally B, Alwahabi Z, Mahmoud S, Metha G, et al. Flow seeding with elemental metal species via an optical method. Applied Physics B. 2012;107(3):665-8.
35. Chan Q, Medwell P, Kalt P, Alwahabi Z, Dally B, Nathan G. Solvent effects on two-line atomic fluorescence of indium. Applied Optics. 2010;49(8):1257-66.
36. Borggren J, Burns I, Sahlberg A-L, Aldén M, Li Z. Temperature imaging in low-pressure flames using diode laser two-line atomic fluorescence employing a novel indium seeding technique. Applied Physics B. 2016;122(3):1-8.

37. Whiddon R, Zhou B, Borggren J, Aldén M, Li Z. Vapor phase tri-methyl-indium seeding system suitable for high temperature spectroscopy and thermometry. Review of Scientific Instruments. 2015;86(9):093107.
38. Dong X, Sun Z, Nathan G, Ashman P, Gu D. Time-resolved spectra of solar simulators employing metal halide and xenon arc lamps. Solar Energy. 2015;115:613-20.
39. Dong X, Nathan G, Sun Z, Gu D, Ashman P. Concentric multilayer model of the arc in high intensity discharge lamps for solar simulators with experimental validation. Solar Energy. 2015;122:293-306.
40. Smyth K, Shaddix C, Everest D. Aspects of soot dynamics as revealed by measurements of broadband fluorescence and flame luminosity in flickering diffusion flames. Combustion and Flame. 1997;111(3):185-207.

Chapter 7

Summary and Conclusions

The aim of this dissertation is to develop and apply an effective single-shot temperature imaging technique for turbulent sooting flames, with a peak soot volume fraction (f_v) of several parts per million. The specific aims of this research are the following: (1) to advance current understanding of the nanoparticle seeding technique and the influences of nanoparticle seeding on the NTLAF technique; (2) to assess the characteristics of interferences to both the Stokes and anti-Stokes LIF signals in highly sooting flames with a peak soot volume fraction of several parts per million; (3) to identify a means to achieve a sufficient signal-to-interference ratio (SIR) in highly sooting flames and to assess the efficacy of the adopted means for reducing the measurement error to the resulting temperature measurement; (4) to assess the accuracy of the improved NTLAF technique in a well-characterised turbulent sooting flame through a comparison with a previous CARS measurements and to increase the understanding of soot evolution in well-characterised flames from simultaneous and planar measurements of the joint probability density function (PDF) statistics of temperature and soot volume fraction; and (5) to develop a line-wise NTLAF configuration to enable temperature measurements in a highly sooting laminar flame under strong interference from high-flux irradiation and to assess the precision and accuracy of temperature measurements.

The mechanisms of a novel seeding method, nanopaticle seeding, which offers the advantage of having less influence on the flames than the nebuliser seeding method does, were investigated. The first mechanism found was that LIF signal generation was associated with the vapourisation of indium nanoparticles into the gas phase by thermal decomposition, particularly in the high temperature region of the flame. A further mechanism for the thermal decomposition of the nanoparticles, that of heating the ablation

products by *in-situ* laser ablation, was also identified. With the identified mechanisms of indium LIF signal generation from nanoparticle seeding, the possible influences of nanoparticle seeding on the NTLAF technique was found to be insignificant in most flame locations, where indium nanoparticles undergo completely decomposition and disappear. The results also suggested that it may be possible to employ an additional pre-ablation laser to accelerate the thermal decomposition of the nanoparticles within the measurement volume slightly before the NTLAF measurement at flame positions close to the burner exit.

The applicability of the NTLAF technique in highly sooting flames has been assessed by investigating the sources of the spectral interferences on indium LIF signals. Three types of spectral interferences have been identified, which are: laser-induced fluorescence by PAH species, laser Mie scattering and laser-induced incandescence from soot particles. The LIF of PAH and LII interferences were both broadband and were spatially, spectrally and temporally over-lapped with the fluorescence signals for both the Stokes and anti- Stokes processes. The understanding of the characteristics of these interferences lead to the design and implementation of a set of custom-made narrow-band filters (FWHM = 1.2 nm) for interference suppression. It has been shown that superb signal-to-interference ratio could be achieved by using the narrow-band filters, resulting in an increase in both the accuracy and the precision of the temperature measurement. It has been found that the measurement accuracy that is due to the presence of spectral interferences has been improved from 198 K to 10 K at a location where the soot volume fraction is 1.2 part per million. An average reduction of 40% in the standard deviation of the measured temperature in single-shot measurements has also been achieved with the use of high transmission filters. The knowledge on the spectral interferences and the utilisation of narrow-band filters have resulted in reduced temperature measurement uncertainty and have enabled reliable planar temperature measurements in highly sooting flames.

The accuracy of the improved NTLAF technique was assessed by comparing results to that obtained with an independent method on a well-characterised, lifted turbulent ethylene jet flame with a peak soot volume fraction of several parts per million. The results showed that the temperature measurements with the NTLAF technique yielded good agreement with previous measurements obtained with CARS technique. In particular, the most probable temperatures agreed within 30 K and the mean temperatures agreed well at those locations where more than 90%

of the data were within the detection limit. This applies to most of the central region of the flame. Furthermore, the probability of a strong signal was found to be a reliable determinant of the extent to which the two techniques agreed. Sensitivity of the measurement to probe resolution was also found, highlighting the need for good spatial resolution in temperature measurements. This direct comparison of temperature results demonstrates the capability of the improved NTLAF technique for single-shot temperature measurements in highly sooting flames.

Simultaneous soot volume fraction measurements was performed with LII technique in the same lifted turbulent ethylene jet flame to advance the understanding of soot evolution in turbulent flames. The joint probability of temperature and soot volume fraction was found to depend more strongly on axial than on radial distance, consistent with previous trends found in other flames. The typical most probable values in the joint PDF were measured for the first time in this flame to be $f_v \sim 0.08$ part per million and T $\sim$ 1500 K from three flame heights. The values of the joint probability density function were also found to be consistent with previous measurements by the Sandia group that were obtained with an alternative technique given the differences in flame size and lift-off height, although a direct comparison would be needed to quantify the level of agreement. These measurements have provided reliable experimental data to advance detailed understanding of the soot formation and oxidation processes in turbulent sooty flames.

Line-wise NTLAF has also been developed to enable flame temperature measurements in laminar non-premixed ethylene sooting flames under strong interference from high-flux, broad-band irradiation, which is relevant to the high temperature conditions of solar receiver-combustors. The strong scattering interference to the NTLAF signal from the irradiated soot particles was found to be 3% for Stokes and 17% for anti-Stokes LIF signal. This interference was accounted for by subtracting the background image of the scattered light from the LIF images. A signal-to-interference ratio of 60-70 and 20-40 was found for the Stokes and anti-Stokes process, respectively. The measured averaged temperature probability distribution has a standard deviation of 40 K or 2.2%, while the measurement accuracy due to the presence of spectral interferences was 45 K. The high-flux solar irradiation was also found to increase the temperature of the flame by up to $\sim$ 100 K at heights above burner (HAB) between 26 mm and 41 mm and by $\sim$ 50 K elsewhere on the centreline. The radial profiles of temperature show similar trends. The line-wise TLAF and its demonstrated accuracy enables reliable flame temperature measurements in highly sooting flames

under high-flux, broad-band irradiation.

In summary, this dissertation presents a breakthrough in flame temperature measurements in highly sooting flames with soot volume fractions of several part per million, which is important for the study of the fundamental processes of turbulent non-premixed flames that contain soot.

7.1 Future Work

This dissertation reports significant advancement of a single-shot laser-based temperature imaging technique for sooting flames with a peak soot volume fraction of several parts per million. Future investigations can be undertaken to further improve this technique and to complement the results of this research:

- In addition to using narrow-band filters (FWHM = 1.2 nm) to improve the precision and accuracy of NTLAF measurements in highly sooting flames, it is also worth investigating potential means for further improvement. For example, to use a detector gate width that is shorter than the one used in the current NTLAF system of 30 ns, this has been estimated to offer a less than a factor of two improvement in signal-to-interference ratio. A laser with a line width narrower than $\sim$ 0.35 cm^{-1} can also be used to enhance SIR. However, the application of lasers with such a narrow line width may suffer from reduced spectral overlap between the laser line width and the indium absorption lines. In addition, narrow-band filters with a bandwidth less than 1.2 nm may also be an effective means at the expense of having a reduced angle of view.

- The effects of shot-to-shot variations in laser modes on temperature measurements are worth investigation. This can be done by monitoring the variations using an oscilloscope to estimate their potential influence on temperature measurements.

- At sufficiently high soot volume fractions (e.g., $\sim$ 10 part per million), it has been found that out-of-plane fluorescence from atomic indium generated by secondary, scattered excitation from soot up-beam in the flame that becomes noticeable and may impose uncertainty on the

temperature measurements. Although the soot volume fraction under these operating conditions exceeds most measured values in turbulent flames, which is the main target of the planar NTLAF technique, it may still be worth investigating the effect of this phenomena on NTLAF measurements. Among potential solutions, structured laser illumination may offer the potential to resolve this issue [98, 99].

- The findings from the investigation of the indium nanoparticle seeding method indicates that free indium atoms generated from *in-situ* laser ablation may exist in the air for up to 10^5 ns, making indium nanoparticles a potential candidate for an atomic tagging velocimetry tracer species. In comparison with conventional molecular tagging technique [100], which uses gas species such as NO as the tagging species, the atomic indium tagging technique offers stronger LIF signal and produces less diffusion into the flow, allowing less seeding concentration and more accurate small-scale measurements in turbulent environments. However, it should be noted that the indium atoms are not conservative scalars and may be consumed in the flames. In addition, the proposed atomic tagging velocimetry technique cannot measure out-of-plane velocity vectors.

- In turbulent non-premixed flames, the influence of local defocusing/focusing of the laser sheet from beam steering may result in an inhomogeneous laser profile [101], imposing uncertainties on laser profile correction and, hence, on the temperature results. This, along with signal trapping, is also worth further investigation.

- From this research, it was found that for band-pass filters with a sufficiently high optical density at the excitation wavelength (e.g., $\sim$ 6), the NTLAF technique might be immune to strong scattering. This makes NTLAF not only resistant to scattering from soot particles in highly sooting flames but also to strong scattering from the wall, making NTLAF a good candidate for wall-temperature measurements. However, this is yet to be assessed.

- Finally, a new analysis method should be developed to analyse the simultaneous, planar soot volume fraction and temperature data in turbulent flames. This method should be able to extract information

such as local gradient of gas temperature and to quantify soot sheets.

References

[1] World Energy Outlook 2014, Report, International Energy Agency (November 2014).

[2] T. C. Bond, S. J. Doherty, D. Fahey, P. Forster, T. Berntsen, B. DeAngelo, M. Flanner, S. Ghan, B. Kärcher, D. Koch, et al., Bounding the role of black carbon in the climate system: A scientific assessment, Journal of Geophysical Research: Atmospheres 118 (11) (2013) 5380–5552.

[3] C. de Haar, I. Hassing, M. Bol, R. Bleumink, R. Pieters, Ultrafine carbon black particles cause early airway inflammation and have adjuvant activity in a mouse allergic airway disease model, Toxicological Sciences 87 (2) (2005) 409–418.

[4] M. R. Heal, P. Kumar, R. M. Harrison, Particles, air quality, policy and health, Chemical Society Reviews 41 (19) (2012) 6606–6630.

[5] W. Kim, C. M. Sorensen, D. Fry, A. Chakrabarti, Soot aggregates, superaggregates and gel-like networks in laminar diffusion flames, Journal of Aerosol Science 37 (3) (2006) 386–401.

[6] I. M. Kennedy, Models of soot formation and oxidation, Progress in Energy and Combustion Science 23 (2) (1997) 95–132.

[7] R. L. Vander Wal, Soot precursor carbonization: Visualization using lif and lii and comparison using bright and dark field tem, Combustion and Flame 112 (4) (1998) 607–616.

[8] P. Reilly, R. Gieray, W. Whitten, J. Ramsey, Direct observation of the evolution of the soot carbonization process in an acetylene diffusion flame via real-time aerosol mass spectrometry, Combustion and Flame 122 (1) (2000) 90–104.

[9] C. Tien, S. Lee, Flame radiation, Progress in Energy and Combustion Science 8 (1) (1982) 41–59.

[10] Ü. Ö. Köylü, C. S. McEnally, D. E. Rosner, L. D. Pfefferle, Simultaneous measurements of soot volume fraction and particle size/microstructure in flames using a thermophoretic sampling technique, Combustion and Flame 110 (4) (1997) 494–507.

[11] R. Santoro, H. Semerjian, R. Dobbins, Soot particle measurements in diffusion flames, Combustion and Flame 51 (1983) 203–218.

[12] C. R. Shaddix, J. Zhang, W. Scheffer, J. Doom, J. C. Oefelein, S. Kook, L. M. Pickett, H. Wang, Understanding and predicting soot generation in turbulent non-premixed jet flames, Sand2010-7178, Sandia Report.

[13] A. D'alessio, A. Di Lorenzo, F. Beretta, C. Venitozzi, Optical and chemical investigations on fuel-rich methane-oxygen premixed flames at atmospheric pressure, in: Symposium (International) on Combustion, Vol. 14, Elsevier, 1973, pp. 941–953.

[14] S. J. Harris, A. M. Weiner, Surface growth of soot particles in premixed ethylene/air flames, Combustion Science and Technology 31 (3-4) (1983) 155–167.

[15] H. Bockhorn, F. Fetting, A. Heddrich, G. Wannemacher, Investigation of the surface growth of soot in flat low pressure hydrocarbon oxygen flames, in: Symposium (International) on Combustion, Vol. 20, Elsevier, 1985, pp. 979–988.

[16] N. H. Qamar, G. J. Nathan, Z. T. Alwahabi, Q. N. Chan, Soot sheet dimensions in turbulent nonpremixed flames, Combustion and Flame 158 (12) (2011) 2458–2464.

[17] S. P. Kearney, D. R. Guildenbecher, C. Winters, T. W. Grasser, P. A. Farias, J. C. Hewson, Temperature, oxygen, and soot-volume-fraction measurements in a turbulent C2H4-fueled jet flame, Tech. rep., Sandia National Laboratories (SNL-NM), Albuquerque, NM (United States) (2015).

[18] M. Köhler, K. Geigle, W. Meier, B. Crosland, K. Thomson, G. Smallwood, Sooting turbulent jet flame: characterization and quantitative soot measurements, Applied Physics B 104 (2) (2011) 409–425.

[19] M. Köhler, K.-P. Geigle, T. Blacha, P. Gerlinger, W. Meier, Experimental characterization and numerical simulation of a sooting lifted turbulent jet diffusion flame, Combustion and Flame 159 (8) (2012) 2620–2635.

[20] M. Smooke, M. Long, B. Connelly, M. Colket, R. Hall, Soot formation in laminar diffusion flames, Combustion and Flame 143 (4) (2005) 613 – 628.

[21] A. C. Eckbreth, Laser diagnostics for combustion temperature and species, Vol. 3, CRC Press, 1996.

[22] J. W. Daily, Laser induced fluorescence spectroscopy in flames, Progress in Energy and Combustion Science 23 (2) (1997) 133–199.

[23] K. Kohse-Hóinghaus, J. Jeffries, Applied combustion diagnostics, Taylor & Francis, 2002.

[24] R. S. Barlow, Laser diagnostics and their interplay with computations to understand turbulent combustion, Proceedings of the Combustion Institute 31 (1) (2007) 49–75.

[25] G. Nathan, P. Kalt, Z. Alwahabi, B. Dally, P. Medwell, Q. Chan, Recent advances in the measurement of strongly radiating, turbulent reacting flows, Progress in Energy and Combustion Science 38 (1) (2012) 41–61.

[26] E. Cenker, K. Kondo, G. Bruneaux, T. Dreier, T. Aizawa, C. Schulz, Assessment of soot particle-size imaging with LII at diesel engine conditions, Applied Physics B 119 (4) (2015) 765–776.

[27] E. Cenker, G. Bruneaux, T. Dreier, C. Schulz, Sensitivity analysis for soot particle size imaging with laser-induced incandescence at high pressure, Applied Physics B 119 (4) (2015) 745–763.

[28] E. Cenker, G. Bruneaux, T. Dreier, C. Schulz, Determination of small soot particles in the presence of large ones from time-resolved laser-induced incandescence, Applied Physics B 118 (2) (2015) 169–183.

[29] B. Crosland, K. Thomson, M. Johnson, Instantaneous in-flame measurement of soot volume fraction, primary particle diameter, and aggregate radius of gyration via auto-compensating laser-induced incandescence and two-angle elastic light scattering, Applied Physics B 112 (3) (2013) 381–393.

[30] Z. Sun, D. Gu, G. J. Nathan, Z. T. Alwahabi, B. B. Dally, Single-shot, time-resolved planar laser-induced incandescence (TiRe-LII) for soot primary particle sizing in flames, Proceedings of the Combustion Institute 35 (3) (2015) 3673–3680.

[31] M. E. Mueller, Q. N. Chan, N. H. Qamar, B. B. Dally, H. Pitsch, Z. T. Alwahabi, G. J. Nathan, Experimental and computational study of soot evolution in a turbulent nonpremixed bluff body ethylene flame, Combustion and Flame 160 (7) (2013) 1298–1309.

[32] F. Goulay, P. E. Schrader, X. López-Yglesias, H. A. Michelsen, A data set for validation of models of laser-induced incandescence from soot: temporal profiles of LII signal and particle temperature, Applied Physics B 112 (3) (2013) 287–306.

[33] A. Coppalle, D. Joyeux, Temperature and soot volume fraction in turbulent diffusion flames: measurements of mean and fluctuating values, Combustion and Flame 96 (3) (1994) 275–285.

[34] J. J. Murphy, C. R. Shaddix, Soot property measurements in a two-meter diameter JP-8 pool fire, Combustion Science and Technology 178 (5) (2006) 865–894.

[35] S. M. Mahmoud, G. J. Nathan, P. R. Medwell, B. B. Dally, Z. T. Alwahabi, Simultaneous planar measurements of temperature and soot volume fraction in a turbulent non-premixed jet flame, Proceedings of the Combustion Institute 35 (2) (2015) 1931–1938.

[36] V. Narayanaswamy, N. Clemens, Simultaneous LII and PIV measurements in the soot formation region of turbulent non-premixed jet flames, Proceedings of the Combustion Institute 34 (1) (2013) 1455–1463.

[37] Y. Sivathanu, G. M. Faeth, Temperature/soot volume fraction correlations in the fuel-rich region of buoyant turbulent diffusion flames, Combustion and Flame 81 (2) (1990) 150–165.

[38] L. Gritzo, Y. Sivathanu, W. Gill, Transient measurements of radiative properties, soot volume fraction and soot temperature in a large pool fire, Combustion Science and Technology 139 (1) (1998) 113–136.

[39] J. Engström, J. Nygren, M. Aldén, C. Kaminski, Two-line atomic fluorescence as a temperature probe for highly sooting flames, Optics Letters 25 (19) (2000) 1469–1471.

[40] J. Nygren, J. Engström, J. Walewski, C. Kaminski, M. Aldén, Applications and evaluation of two-line atomic LIF thermometry in sooting combustion environments, Measurement Science and Technology 12 (8) (2001) 1294.

[41] P. R. Medwell, Q. N. Chan, P. A. Kalt, Z. T. Alwahabi, B. B. Dally, G. J. Nathan, Development of temperature imaging using two-line atomic fluorescence, Applied Optics 48 (6) (2009) 1237–1248.

[42] P. R. Medwell, Q. N. Chan, P. A. Kalt, Z. T. Alwahabi, B. B. Dally, G. J. Nathan, Instantaneous temperature imaging of diffusion flames using two-line atomic fluorescence, Applied Spectroscopy 64 (2) (2010) 173–176.

[43] Q. N. Chan, P. R. Medwell, P. A. Kalt, Z. T. Alwahabi, B. B. Dally, G. J. Nathan, Simultaneous imaging of temperature and soot volume fraction, Proceedings of the Combustion Institute 33 (1) (2011) 791–798.

[44] A. Manteghi, Y. Shoshin, N. Dam, L. de Goey, Two-line atomic fluorescence thermometry in the saturation regime, Applied Physics B 118 (2) (2015) 281–293.

[45] Q. N. Chan, P. R. Medwell, Z. T. Alwahabi, B. B. Dally, G. J. Nathan, Assessment of interferences to nonlinear two-line atomic fluorescence (NTLAF) in sooty flames, Applied Physics B 104 (1) (2011) 189–198.

[46] Q. N. Chan, P. R. Medwell, B. B. Dally, Z. T. Alwahabi, G. J. Nathan, New seeding methodology for gas concentration measurements, Applied Spectroscopy 66 (7) (2012) 803–809.

[47] P. Medwell, Q. Chan, B. Dally, Z. Alwahabi, S. Mahmoud, G. Metha, G. Nathan, Flow seeding with elemental metal species via an optical method, Applied Physics B 107 (3) (2012) 665–668.

[48] P. R. Medwell, Q. N. Chan, B. B. Dally, S. Mahmoud, Z. T. Alwahabi, G. J. Nathan, Temperature measurements in turbulent non-premixed flames by two-line atomic fluorescence, Proceedings of the Combustion Institute 34 (2) (2013) 3619–3627.

[49] G. J. Nathan, B. Dally, P. Ashman, A. Steinfeld, Hybrid receiver-combustor, US Patent App. 14/388,867 (Mar. 28 2013).

[50] M. Aldén, J. Bood, Z. Li, M. Richter, Visualization and understanding of combustion processes using spatially and temporally resolved laser diagnostic techniques, Proceedings of the Combustion Institute 33 (1) (2011) 69–97.

[51] A. Steinfeld, R. Bombach, P. Haueter, B. Hemmerling, W. Kreutner, G. Thompson, D. Wuillemin, Experimental setup of a laser diagnostics system for a high-temperature solar receiver/reactor, Journal of Solar Energy Engineering 116 (4) (1994) 206–211.

[52] C. Kaminski, J. Engström, M. Aldén, Quasi-instantaneous two-dimensional temperature measurements in a spark ignition engine using 2-line atomic fluorescence, in: Symposium (International) on Combustion, Vol. 27, Elsevier, 1998, pp. 85–93.

[53] S. R. Turns, An introduction to combustion, Vol. 287, McGraw-hill New York, 1996.

[54] F.-Q. Zhao, H. Hiroyasu, The applications of laser Rayleigh scattering to combustion diagnostics, Progress in Energy and Combustion Science 19 (6) (1993) 447–485.

[55] D. Hofmann, A. Leipert, Temperature field measurements in a sooting flame by filtered Rayleigh scattering (FRS), in: Symposium (International) on Combustion, Vol. 26, Elsevier, 1996, pp. 945–950.

[56] S. P. Kearney, R. W. Schefer, S. J. Beresh, T. W. Grasser, Temperature imaging in nonpremixed flames by joint filtered Rayleigh and Raman scattering, Applied Optics 44 (9) (2005) 1548–1558.

[57] E. Kristensson, A. Ehn, J. Bood, M. Aldén, Advancements in Rayleigh scattering thermometry by means of structured illumination, Proceedings of the Combustion Institute 35 (3) (2015) 3689–3696.

[58] D. Most, A. Leipertz, Simultaneous two-dimensional flow velocity and gas temperature measurements by use of a combined particle image velocimetry and filtered Rayleigh scattering technique, Applied Optics 40 (30) (2001) 5379–5387.

[59] A. Bohlin, C. Kliewer, Diagnostic imaging in flames with instantaneous planar coherent raman spectroscopy, The Journal of Physical Chemistry Letters 5 (7) (2014) 1243–1248.

[60] Z. Yin, I. Adamovich, W. Lempert, OH radical and temperature measurements during ignition of H2-air mixtures excited by a repetitively pulsed nanosecond discharge, Proceedings of the Combustion Institute 34 (2) (2013) 3249 – 3258.

[61] O. M. Feroughi, S. Hardt, I. Wlokas, T. Hülser, H. Wiggers, T. Dreier, C. Schulz, Laser-based in situ measurement and simulation of gas-phase temperature and iron atom concentration in a pilot-plant nanoparticle synthesis reactor, Proceedings of the Combustion Institute 35 (2) (2015) 2299–2306.

[62] H. Kronemayer, P. Ifeacho, C. Hecht, T. Dreier, H. Wiggers, C. Schulz, Gas-temperature imaging in a low-pressure flame reactor for nanoparticle synthesis with multi-line NO-LIF thermometry, Applied Physics B 88 (3) (2007) 373–377.

[63] T. Meyer, S. Roy, R. Lucht, J. Gord, Dual-pump dual-broadband CARS for exhaust-gas temperature and CO2–O2–N2 mole-fraction measurements in model gas-turbine combustors, Combustion and Flame 142 (1) (2005) 52–61.

[64] S. Roy, T. R. Meyer, R. P. Lucht, V. M. Belovich, E. Corporan, J. R. Gord, Temperature and CO2 concentration measurements in the exhaust stream of a liquid-fueled combustor using dual-pump coherent anti-Stokes Raman scattering (CARS) spectroscopy, Combustion and Flame 138 (3) (2004) 273–284.

[65] S. P. Kearney, K. Frederickson, T. W. Grasser, Dual-pump coherent anti-Stokes Raman scattering thermometry in a sooting turbulent pool fire, Proceedings of the Combustion Institute 32 (1) (2009) 871–878.

[66] M. Afzelius, P.-E. Bengtsson, J. Bood, C. Brackmann, A. Kurtz, Development of multipoint vibrational coherent anti-Stokes Raman spectroscopy for flame applications, Applied Optics 45 (6) (2006) 1177–1186.

[67] M. Aldén, P. Bengtsson, H. Edner, S. Kröll, D. Nilsson, Rotational CARS - A comparison of different techniques with emphasis on accuracy in temperature determination, Applied Optics 28 (15) (1989) 3206–3219.

[68] M. Tamura, J. Luque, J. Harrington, P. Berg, G. Smith, J. Jeffries, D. Crosley, Laser-induced fluorescence of seeded nitric oxide as a flame thermometer, Applied Physics B: Lasers and Optics 66 (4) (1998) 503–510.

[69] J. M. Seitzman, R. Hanson, P. DeBarber, C. Hess, Application of quantitative two-line OH planar laser-induced fluorescence for temporally

resolved planar thermometry in reacting flows, Applied Optics 33 (18) (1994) 4000–4012.

[70] M. Haudiquert, A. Cessou, D. Stepowski, A. Coppalle, OH and soot concentration measurements in a high-temperature laminar diffusion flame, Combustion and Flame 111 (4) (1997) 338–349.

[71] R. G. Joklik, J. W. Daily, Two-line atomic fluorescence temperature measurement in flames: an experimental study, Applied Optics 21 (22) (1982) 4158–4162.

[72] N. Omenetto, P. Benetti, G. Rossi, Flame temperature measurements by means of atomic fluorescence spectrometry, Spectrochimica Acta Part B: Atomic Spectroscopy 27 (10) (1972) 453–461.

[73] G. Zizak, F. Cignoli, S. Benecchi, Local flame temperature precision by the two-line atomic fluorescence method and the photon-counting technique, Applied Spectroscopy 33 (2) (1979) 179–182.

[74] J. Hult, I. Burns, C. Kaminski, Two-line atomic fluorescence flame thermometry using diode lasers, Proceedings of the Combustion Institute 30 (1) (2005) 1535–1543.

[75] R. S. Chrystie, I. S. Burns, J. Hult, C. F. Kaminski, High-repetition-rate combustion thermometry with two-line atomic fluorescence excited by diode lasers, Optics Letters 34 (16) (2009) 2492–2494.

[76] Q. N. Chan, P. R. Medwell, P. A. Kalt, Z. T. Alwahabi, B. B. Dally, G. J. Nathan, Solvent effects on two-line atomic fluorescence of indium, Applied Optics 49 (8) (2010) 1257–1266.

[77] D. Gu, Z. Sun, P. R. Medwell, Z. T. Alwahabi, B. B. Dally, G. J. Nathan, Mechanism for laser-induced fluorescence signal generation in a nanoparticle-seeded flow for planar flame thermometry, Applied Physics B 118 (2) (2015) 209–218.

[78] R. Whiddon, B. Zhou, J. Borggren, M. Aldén, Z. Li, Vapor phase tri-methyl-indium seeding system suitable for high temperature spectroscopy and thermometry, Review of Scientific Instruments 86 (9) (2015) 093107.

[79] W. Meier, R. Barlow, Y.-L. Chen, J.-Y. Chen, Raman/Rayleigh/LIF measurements in a turbulent $CH_4/H_2/N_2$ jet diffusion flame: experimental techniques and turbulence–chemistry interaction, Combustion and Flame 123 (3) (2000) 326–343.

[80] C. R. Shaddix, Correcting thermocouple measurements for radiation loss: a critical review, Tech. rep., Sandia National Labs., Livermore, CA (US) (1999).

[81] I. S. Burns, X. Mercier, M. Wartel, R. S. Chrystie, J. Hult, C. F. Kaminski, A method for performing high accuracy temperature measurements in low-pressure sooting flames using two-line atomic fluorescence, Proceedings of the Combustion Institute 33 (1) (2011) 799–806.

[82] B. Chakraborty, R. Long, The formation of soot and polycyclic aromatic hydrocarbons in diffusion flames III-effect of additions of oxygen to ethylene and ethane respectively as fuels, Combustion and Flame 12 (5) (1968) 469–476.

[83] I. Glassman, Sooting laminar diffusion flames: effect of dilution, additives, pressure, and microgravity, in: Symposium (International) on Combustion, Vol. 27, Elsevier, 1998, pp. 1589–1596.

[84] P. R. Medwell, A. R. Masri, P. X. Pham, B. B. Dally, G. J. Nathan, Temperature imaging of turbulent dilute spray flames using two-line atomic fluorescence, Experiments in Fluids 55 (11) (2014) 1–11.

[85] S. Lai, J. Guo, V. Petrova, G. Ramanath, L. Allen, Size-dependent melting properties of small tin particles: nanocalorimetric measurements, Physical Review Letters 77 (1) (1996) 99.

[86] R. A. Yetter, G. A. Risha, S. F. Son, Metal particle combustion and nanotechnology, Proceedings of the Combustion Institute 32 (2) (2009) 1819–1838.

[87] A. Il'in, A. Gromov, V. Vereshchagin, E. Popenko, V. Surgin, H. Lehn, Combustion of ultrafine aluminum in air, Combustion, Explosion and Shock Waves 37 (6) (2001) 664–668.

[88] Y.-S. Kwon, A. A. Gromov, A. P. Ilyin, E. M. Popenko, G.-H. Rim, The mechanism of combustion of superfine aluminum powders, Combustion and Flame 133 (4) (2003) 385–391.

[89] F. E. Kruis, H. Fissan, A. Peled, Synthesis of nanoparticles in the gas phase for electronic, optical and magnetic applicationsa review, Journal of Aerosol Science 29 (5) (1998) 511–535.

[90] A. Lushnikov, Laser induced aerosols, Journal of Aerosol Science 27 (1996) S377–S378.

[91] S.-B. Wen, X. Mao, R. Greif, R. E. Russo, Laser ablation induced vapor plume expansion into a background gas. II. Experimental analysis, Journal of Applied Physics 101 (2) (2007) 023115.

[92] S.-B. Wen, X. Mao, R. Greif, R. E. Russo, Expansion of the laser ablation vapor plume into a background gas. I. Analysis, Journal of Applied Physics 101 (2) (2007) 023114.

[93] C. Liu, A study of particle generation during laser ablation with applications, Lawrence Berkeley National Laboratory.

[94] D. Gu, Z. Sun, G. J. Nathan, P. R. Medwell, Z. T. Alwahabi, B. B. Dally, Improvement of precision and accuracy of temperature imaging in sooting flames using two-line atomic fluorescence (TLAF), Combustion and Flame 167 (2016) 481 – 493.

[95] G. Nathan, D. Battye, P. Ashman, Economic evaluation of a novel fuel-saver hybrid combining a solar receiver with a combustor for a solar power tower, Applied Energy 113 (2014) 1235–1243.

[96] X. Dong, G. J. Nathan, S. M. Mahmoud, P. J. Ashman, D. Gu, B. B. Dally, Global characteristics of non-premixed jet flames of hydrogen–hydrocarbon blended fuels, Combustion and Flame 162 (4) (2015) 1326–1335.

[97] S. R. Turns, F. H. Myhr, Oxides of nitrogen emissions from turbulent jet flames: Part I-Fuel effects and flame radiation, Combustion and Flame 87 (3) (1991) 319–335.

[98] E. Kristensson, A. Ehn, J. Bood, M. Aldn, Advancements in Rayleigh scattering thermometry by means of structured illumination, Proceedings of the Combustion Institute 35 (3) (2015) 3689 – 3696.

[99] N. J. Kempema, M. B. Long, Quantitative Rayleigh thermometry for high background scattering applications with structured laser illumination planar imaging, Applied Optics 53 (29) (2014) 6688–6697.

[100] J. Bominaar, M. Pashtrapanska, T. Elenbaas, N. Dam, H. Ter Meulen, W. van de Water, Writing in turbulent air, Physical Review E 77 (4) (2008) 046312.

[101] Z. Sun, Z. T. Alwahabi, D. Gu, S. M. Mahmoud, G. J. Nathan, B. B. Dally, Planar laser-induced incandescence of turbulent sooting flames: the influence of beam steering and signal trapping, Applied Physics B 119 (4) (2015) 731–743.